

Copyright
by
Nikolaos Bouklas
2014

**The Dissertation Committee for Nikolaos Bouklas Certifies that this is the approved
version of the following dissertation:**

**MODELLING AND SIMULATIONS OF HYDROGELS WITH
COUPLED SOLVENT DIFFUSION AND LARGE DEFORMATION**

Committee:

Rui Huang, Supervisor

Chad Landis, Co-Supervisor

Stelios Kyriakides

Krishnaswamy Ravi-Chandar

Michael Sacks

**MODELLING AND SIMULATIONS OF HYDROGELS WITH
COUPLED SOLVENT DIFFUSION AND LARGE DEFORMATION**

by

Nikolaos Bouklas B. M. E.

Dissertation

Presented to the Faculty of the Graduate School of

The University of Texas at Austin

in Partial Fulfillment

of the Requirements

for the Degree of

Doctor of Philosophy

The University of Texas at Austin

December 2014

Acknowledgements

At the moment of writing this acknowledgement, I am in the final steps of completing my thesis and I cannot help but recollect on the five years I have spent at the Aerospace Engineering and Engineering Mechanics department of the University of Texas at Austin, and all the faculty, friends and family who have supported me during my graduate studies.

First, I would like to sincerely thank my advisors, Professor Rui Huang and Professor Chad Landis for their thoughtful mentoring. They have shared their vision and knowledge, helped me when I had problems, and have inspired me to be a better scientist. I could not be more grateful for their help.

I would like to thank the members of my PhD committee: Professor Stelios Kyriakides, for sharing his knowledge on the foundation of engineering mechanics in his classes that I attended, and always being available to offer his advice; Professor K. Ravi-Chandar, for being such an inspiring teacher, always being able to communicate complicated notions in the most comprehensible fashion; and Professor Michael Sacks, for his insightful suggestions and constructive criticism.

From my time as a student in Greece, I would like to thank Professor Athanasios Mihailidis and Professor Sotirios Natsiavas from Aristotle University of Thessaloniki, and my math teachers, Vasilis Adam from the American College of Thessaloniki and Asterios Pyrros, principal of Rigas Fereos elementary school, for encouraging and motivating me to follow this path. Also, my colleagues in UT, Dr. Stavros Gaitanaros, Dr. Dorinamaria Carka, Dr Aaron Albrecht, Dr. Wei Gao, Professor Michael Borden, Nathan Bechle, Zachary Wilson, Anand Karpatne, Andrew Gross, and my friends in

Austin and Greece, Larry, Tasos, George, Stelios, Alex, Lydia, Danae, Ryan, Bob, for being there and making these five years so interesting.

To my family and especially my parents I would like to express my gratitude, for always supporting me in every possible way, and most of all to my wife Christina, for leaving everything behind in Greece and joining me in pursuing my dreams.

MODELLING AND SIMULATIONS OF HYDROGELS WITH COUPLED SOLVENT DIFFUSION AND LARGE DEFORMATION

Nikolaos Bouklas, Ph.D

The University of Texas at Austin, 2014

Supervisors: Rui Huang and Chad M. Landis

Swelling of a polymer gel is a kinetic process coupling mass transport and mechanical deformation. A comparison between a nonlinear theory for polymer gels and the classical theory of linear poroelasticity is presented. It is shown that the two theories are consistent within the linear regime under the condition of a small perturbation from an isotropically swollen state of the gel. The relationships between the material properties in the linear theory and those in the nonlinear theory are established by a linearization procedure. Both linear and nonlinear solutions are presented for swelling kinetics of substrate-constrained and freestanding hydrogel layers. A new procedure is suggested to fit the experimental data with the nonlinear theory.

A nonlinear, transient finite element formulation is presented for initial boundary value problems associated with swelling and deformation of hydrogels, based on nonlinear continuum theories for hydrogels with compressible and incompressible constituents. The incompressible instantaneous response of the aggregate imposes a constraint to the finite element discretization in order to satisfy the LBB condition for numerical stability of the mixed method. Three problems of practical interests are considered: constrained swelling, flat-punch indentation, and fracture of hydrogels. Constrained swelling may lead to instantaneous surface instability. Indentation relaxation

of hydrogels is simulated beyond the linear regime under plane strain conditions, and is compared with two elastic limits for the instantaneous and equilibrium states. The effects of Poisson's ratio and loading rate are discussed.

On the study of hydrogel fracture, a method for calculating the transient energy release rate for crack growth in hydrogels, based on a modified path-independent J-integral, is presented. The transient energy release rate takes into account the energy dissipation due to diffusion. Numerical simulations are performed for a stationary center crack loaded in mode I, with both immersed and non-immersed chemical boundary conditions. Both sharp crack and blunted notch crack models are analyzed over a wide range of applied remote tensile strains. Comparisons to linear elastic fracture mechanics are presented. A critical condition is proposed for crack growth in hydrogels based on the transient energy release rate. The applicability of this growth condition for simulating concomitant crack propagation and solvent diffusion in hydrogels is discussed.

Table of Contents

List of Tables	xi
List of Figures	xii
Chapter 1. Introduction	1
1.1 Motivation.....	1
1.2. Theories and numerical methods	5
1.3. Scope of study.....	6
Chapter 2. Swelling Kinetics of Polymer Gels: Comparison of Linear and Nonlinear Theories.....	9
2.1. A nonlinear theory	11
2.2. A linear theory	14
2.3. Swelling of hydrogel layers	18
2.3.1. Constrained swelling.....	18
2.3.2. Free swelling.....	24
2.4. Results and Discussions.....	27
2.4.1. Linear poroelastic properties of a gel.....	27
2.4.2. Linear vs nonlinear analysis of swelling.....	30
2.4.3. Comparison with experiments	32
2.4.4. On indentation method.....	37
2.5. Summary	39
Chapter 3. A Nonlinear, Transient Finite Element Method.....	41
3.1. Finite element preliminaries for poroelastic problems	41
3.2. A nonlinear theory-compressible formulation	43
3.3. Finite element method– compressible formulation.....	45
3.3.1. Weak form	47
3.3.2. Time integration.....	47
3.3.3. Spatial discretization.....	48
3.3.4. Newton-Raphson method.....	52

3.4. A nonlinear theory-incompressible formulation.....	54
3.5. Finite element method-incompressible formulation.....	56
3.6. Summary.....	57
Chapter 4. Simulation of Hydrogel Swelling.....	58
4.1 Finite element model.....	58
4.2. Numerical stability.....	60
4.3. Convergence study.....	66
4.4. swelling induced surface instability.....	70
4.5. Summary.....	74
Chapter 5. Indentation of Hydrogel Layers.....	75
5.1. Flat punch indentation model.....	76
5.2. Displacement controlled indentation.....	77
5.2.1. Instantaneous and equilibrium limits.....	77
5.2.2. Application of boundary conditions.....	79
5.2.3. Transient response.....	81
5.2.3. Linear poroelastic indentation.....	85
5.2.4. Effect of loading rate.....	88
5.3. Summary.....	89
Chapter 6. Effect of Diffusion on Fracture of Hydrogels.....	91
6.1 General formulation.....	94
6.1.1. A nonequilibrium thermodynamic approach.....	94
6.1.2. Transient energy release rate.....	97
6.1.3. Domain integral method.....	102
6.2. Numerical results.....	103
6.2.1. Sharp crack model.....	108
6.2.1.1. Small far-field deformations.....	108
6.2.1.2. Moderate far-field deformations.....	127
6.2.2. Notched crack model.....	132
6.2.2.1. Moderate far-field deformations.....	133

6.2.2.2. Large far-field deformations	137
6.3. Summary	138
Chapter 7	140
Conclusions.....	140
Appendices.....	143
Appendix A: Linear elastic properties of gel.....	143
Appendix B: Solution procedures for constrained and free swelling	147
B.1 Constrained swelling by the nonlinear theory.....	147
B.2 Free swelling by the nonlinear theory	149
B.3 Free swelling by the linear poroelasticity theory	152
Appendix C: Analytical solutions for constrained swelling of hydrogels ..	155
C.1 Initial state.....	155
C.2 Equilibrium state	156
C.3 Early stage of swelling: a self-similar solution.....	156
Appendix D: Flat punch indentation of an elastic half space	159
Bibliography	161
Vita	172

List of Tables

Table 5.1: Intrinsic properties of hydrogels for two different Poisson's ratios ($K = 10^3 Nk_b T$ for all cases).	87
---------------------------------------------------------------------------------------------------------------------------	----

List of Figures

Figure 1.1:	Hydrogel used in drug delivery. (Pal et al., 2009).....	1
Figure 1.2:	Flow control in microfluidic applications.(Beebe et al., 2000).	2
Figure 1.3:	Spatially and sequentially programmable 3D patterned shapes. Hydrogels can transform with solvent absorption and desorption. (Palleau et al., 2013)	3
Figure 1.4:	Electrically activated hydrogel robots. (Palleau et al., 2013)	3
Figure 1.5:	Actuation process of walking hydrogel robots. (Morales et al., 2014).	4
Figure 1.6:	Hydrogel fracture (Kwon et al., 2011; http://www.ppm.d.espci.fr/spip.php?article250&lang=fr).....	5
Figure 2.1:	Schematic illustration of a thin hydrogel layer, subject to constrained or free swelling. In the present study, the initial state is assumed to be isotropically swollen from the dry state with $h_0/H = l_0/L = w_0/W =$ λ_0	10
Figure 2.2:	Evolution of (a) stretch and (b) swelling induced compressive stress in a constrained hydrogel layer by the nonlinear theory, with $N\Omega =$ 0.001 , $\chi = 0.4$, and $\lambda_0 = 1.4$. The time is normalized by $\tau_1 = H^2 / D$	20
Figure 2.3:	(a) Thickness swelling ratio as a function of time for constrained hydrogel layers with $N\Omega = 0.001$, $\lambda_0 = 1.4$, and different values for χ . The horizontal dashed lines indicate the equilibrium swelling ratio, $h_\infty / h_0 = \lambda_\infty^c / \lambda_0$. (b) Normalized thickness change as a function of time, in comparison with the self-similar solution (dashed lines). ...	22

Figure 2.4: Numerical results for free swelling of a hydrogel layer by the nonlinear theory ($\chi = 0.4$, $N\Omega = 0.001$, $\lambda_0 = 1.4$): (a) swelling ratio in the thickness direction; (b) in-plane swelling ratio (λ_1) and the average thickness ratio (h/H); (c) nominal stress in the in-plane direction.26

Figure 2.5: (a) Poisson's ratio as a function of the initial swelling ratio; (b) Poisson's ratio at the equilibrium swelling ratio as a function of χ . .29

Figure 2.6: Comparison between the nonlinear theory and the linear poroelasticity for constrained swelling of a hydrogel layer ($\chi = 0.4$ and $N\Omega = 0.001$).....31

Figure 2.7: Comparison of the equilibrium swelling ratio for a constrained hydrogel layer ($N\Omega = 0.001$ and $\chi = 0.4$), as predicted by the nonlinear theory and the linear poroelasticity.....32

Figure 2.8: The ratio between the equilibrium thickness changes for constrained and free swelling, predicted by the nonlinear theory as a function of the initial swelling ratio for $N\Omega = 0.001$ and $\chi = 0.1-0.5$, in comparison with the prediction by the linear poroelasticity theory (dashed lines).33

Figure 2.9: A comparison between the nonlinear theory and experimental results for kinetics of constrained and free swelling. The dashed lines reproduce the predictions of linear poroelasticity using the parameters determined by Yoon et al.¹¹ to fit their experimental data. The solid lines are numerical results based on the nonlinear theory using the parameters determined from (5.3)-(5.6): $\lambda_0 = 2.474$, $\chi = 0.4724$, $N\Omega = 7.821 \times 10^{-5}$, and $D = 1.098 \times 10^{-7} \text{ m}^2 \text{ s}^{-1}$37

Figure 3.1: Two types of quadrilateral elements: an equal-order eight-node element (8u8p) and a Taylor-Hood element (8u4p).	42
Figure 4.1: Schematic of a hydrogel layer attached to a rigid substrate. Three types of boundary conditions (S1, S2, and S3) are indicated for the finite element analysis.....	59
Figure 4.2: Numerical oscillations of the chemical potential in the early stage of constrained swelling for a hydrogel layer with $N\Omega = 10^{-3}$, $\chi = 0.4$, $K = 10^3 Nk_B T$, and $\lambda_0 = 1.4$, using the 8u8p elements with $n_e = 20$.	60
Figure 4.3: The amplitude of numerical oscillation in the chemical potential as a function of time, using different numbers of 8u8p elements. The time is normalized by the diffusion time scale for the layer thickness in (a) and the time scale corresponding to the element size in (b).....	62
Figure 4.4: Numerical oscillations of the chemical potential at $t/\tau = 10^{-4}$ for hydrogels with different bulk moduli, using 8u8p elements. The other parameters are: $N\Omega = 10^{-3}$, $\chi = 0.4$, $\lambda_0 = 1.4$, and $n_e = 20$.	63
Figure 4.5: (a) Evolution of chemical potential for constrained swelling of a hydrogel layer with $N\Omega = 10^{-3}$, $\chi = 0.4$, $K = 10^3 Nk_B T$, and $\lambda_0 = 1.4$, using the 8u4p Taylor-Hood elements with $n_e = 20$. (b) Effect of bulk modulus on the numerical solution, at $t/\tau = 10^{-4}$	65

Figure 4.6: Change of thickness for constrained swelling of a hydrogel layer ($N\Omega = 10^{-3}$, $\chi = 0.4$, $K = 10^3 Nk_B T$, $\lambda_0 = 1.4$): (a) Effect of time step ($n_e = 20$); (b) Effect of mesh density; (c) Effect of time step when the boundary condition for chemical potential is applied by linear ramping in 4 time steps. The dashed line is the self-similar solution in the early stage, and the horizontal line indicates the analytical solution for equilibrium swelling ratio.67

Figure 4.7: Comparison between the transient finite element results for constrained swelling (circles) and previous results obtained by a finite difference method (solid lines). The former is for $K = 10^3 Nk_B T$, while the latter is for a hydrogel with incompressible constituents ($K \rightarrow \infty$); the other material parameters are identical: $N\Omega = 10^{-3}$, $\chi = 0.4$, and $\lambda_0 = 1.4$. (a) Chemical potential; (b) Stretch in the thickness direction; (c) In-plane nominal stress; (d) Evolution of thickness swelling ratio for different values of χ 69

Figure 4.8: Effect of bulk modulus on the equilibrium swelling ratio for constrained hydrogel layers with $\chi = 0.4$ and $N\Omega = 10^{-3}$, in comparison with the incompressible limits (dashed lines).70

Figure 4.9: Thickness swelling ratio as a function of time for hydrogels with $\chi = 0.4$ and 0.6 . The dashed line shows the stabilized finite element simulation (with surface constraint) for $\chi = 0.4$. The symbols mark the points where the calculations without surface constraint are terminated due to swell induced surface instability, depending on the mesh density. The solid line shows that the swelling is stable for $\chi = 0.6$ even without the surface constraint. Other parameters: $N\Omega = 10^{-3}$, $K = 10^3 Nk_B T$, and $\lambda_0 = 1.4$71

Figure 5.1: Schematic of a hydrogel layer subject to rigid flat-punch indentation.76

Figure 5.2: Normalized indentation force versus depth at the two elastic limits, predicted by linear and nonlinear finite element methods, for a hydrogel with $\chi = 0.2$, $N\Omega = 10^{-3}$ and $K = 10^3 Nk_B T$. The indenter half-width is $a/h = 0.1$. The approximate analytical solution in Eq. (B.5) is shown as dashed lines for comparison.....78

Figure 5.3: (a) Indentation force as a function of time for a shallow indentation ($\delta/h = 10^{-3}$), in comparison with the linear elastic limits (dashed lines) for instantaneous and equilibrium responses. (b) Normalized indentation force relaxation for various indentation depths, fitted by a function, $g(t/\tau) = 0.25 \exp(-7t/\tau) + 0.75 \exp(-\sqrt{t/\tau})$. Material parameters of the hydrogel are: $\chi = 0.2$, $N\Omega = 10^{-3}$, and $K = 10^3 Nk_B T$ 80

Figure 5.4: Evolution of the von Misses stress (left) and chemical potential (right) fields in a hydrogel layer ($\chi = 0.2$, $N\Omega = 10^{-3}$, $K = 10^3 Nk_B T$) subject to flat punch indentation with $a/h = 0.1$ and $\delta/h = 0.1$, at normalized time $t/\tau = 1, 10^2, 10^4, 10^7$ (from top to bottom).....82

Figure 5.5: Normal and shear contact tractions under the flat-punch indenter with $a/h = 0.1$ and $\delta/h = 0.1$, comparing the numerical solutions with the analytical predictions at the elastic limits for a hydrogel layer ($\chi = 0.2$, $N\Omega = 10^{-3}$, $K = 10^3 Nk_B T$).....84

Figure 5.6: Normalized indentation force relaxation for plane-strain flat punch indentation, with various combinations of material parameters (Table 5.1) corresponding to two effective Poisson's ratios: (a) $\nu_\infty = 0.25$ and (b) $\nu_\infty = 0.49$. The numerical results are fitted by two functions,
 $g_1(t/\tau_*) = 0.25 \exp(-7910t/\tau_*) + 0.75 \exp(-33.6\sqrt{t/\tau_*})$
 $g_2(t/\tau_*) = 0.2 \exp(-330t/\tau_*) + 0.8 \exp(-28\sqrt{t/\tau_*})$ 87

Figure 5.7: Normalized characteristic relaxation time t_{50}/τ_* as a function of Poisson's ratios for plane-strain flat punch indentation with $a/h = 0.1$88

Figure 5.8: Effect of loading rate on indentation force relaxation. The inset shows the linear ramp of the indentation displacement with $\delta^*/h = 0.1$. The horizontal dashed line corresponds to the equilibrium-state solution. Material parameters of the hydrogel are: $\chi = 0.2$, $N\Omega = 10^{-3}$, and $K = 10^3 Nk_B T$; Half-width of the flat-punch indenter: $a/h = 0.1$90

Figure 6.1: Center crack model in Mode I loading.98

Figure 6.2: Schematic (a) of a body containing a sharp crack, and (b) of a body containing a rounded notch crack, both at the reference/dry configuration.....	98
Figure 6.3: Simply connected region A_2 enclosed by contour $C = C_4 - C_1 + C_2 + C_3$	102
Figure 6.4: Mesh for one quartet of the domain. (a) For the sharp crack model, Taylor-Hood 8u-4p quadrilateral elements used everywhere except for the crack tip, where 50 quartet point Taylor-Hood 6u-3p elements are used. (b) Mesh for notched specimen. Taylor-Hood 8u-4p quadrilateral elements are used. The radius of the notch is taken to be three orders of magnitude smaller the crack length $r_n / \alpha = 10^{-3}$ to study very large deformations with respect to the initial state.....	105
Figure 6.5: Immersed center crack specimen in Mode I loading. Cauchy stress distribution for the instantaneous response and at equilibrium for rings of nodes with an increasing distance from the tip,. Dashed lines are obtained from the linear elastic solution.	107
Figure 6.6: Not-immersed center crack specimen in Mode I loading. Cauchy stress distribution for the instantaneous response and at equilibrium for rings of nodes with an increasing distance from the tip Dashed lines are obtained from the linear elastic solution.	111
Figure 6.7: Evolution of the chemical potential (a,b) and concentration fields (c,d) ahead of the crack tip for the immersed (a,c) and the not-immersed (b,d) cases.....	113

Figure 6.8: Chemical potential contours at the instantaneous response limit, showing the difference in the crack tip chemical potential field for (a) the immersed and (b) the not-immersed cases.115

Figure 6.9: Normalized nominal concentration contours at the equilibrium response limit for the (a) immersed and (b) not immersed cases.. .116

Figure 6.10: Crack opening displacement profile evolution for (a) immersed and (b) the not-immersed case. (c) Maximum crack opening displacement evolution for the two cases and a limiting behavior for the immersed case. (d) Evolution of the total force applied to a $h/\alpha = 10$ model for far field strain $\epsilon^\infty = 10^{-3}$ for both the immersed and the not-immersed cases. Dashed lines are linear elastic solutions for all plots.117

Figure 6.11: (a) transient J integral values for paths at different radial distances from the crack tip and at different times, showing path independence for the integral we have defined here, (b) path dependence for classical definition of the J integral if used in a poroelastic system.122

Figure 6.12: Transient J-integral evolution for immersed and not-immersed cases for increasing loading resulting to far field strains $\epsilon^\infty = 10^{-3}, 10^{-2}, 10^{-1}$124

Figure 6.13: Material parameter dependence of the transient J-integral for a not-immersed hydrogel with a center crack is studied. Variation of the crosslink density $N\Omega$ (a,c) and of χ (b,d) are considered for the same type of displacement controlled Mode I loading up to $\epsilon^\infty = 0.1$ for a domain of size $h/\alpha = 10$, using timescale τ for plots (a,b) and timescale τ^* for plots (c,d).126

Figure 6.14: Normalized transient J-integral evolution comparing to the linear elastic solution for immersed (a) and not-immersed (b) cases for increasing loading specified by the far field strain.128

Figure 6.15: Cauchy stress σ_{22} component for the instantaneous (a) and equilibrium (b) response for an immersed center crack model loaded in Mode I for increasing loading indicated by the averaged quantity of the far field strain.....129

Figure 6.16: Comparison using a sharp crack and a notched model $r_n / \alpha = 10^{-3}$ for an immersed center crack model loaded in Mode I at $\epsilon^\infty = 0.1$ for (a) Cauchy stress σ_{22} component for the instantaneous and equilibrium response and (b) the transient J-integral131

Figure 6.17: Evolution of the crack opening displacement profile with a notched center crack $r_n / \alpha = 10^{-3}$, for an (a) immersed and a (b) not-immersed hydrogel loaded in Mode I at $\epsilon^\infty = 0.1$, and for an (c) immersed and a (d) not-immersed hydrogel loaded in Mode I at $\epsilon^\infty = 0.5$134

Figure 6.18: Evolution of (a) the chemical potential and (b) the concentration field, from the crack tip to the end of the specimen for an immersed hydrogel with a notch $r_n / \alpha = 10^{-3}$ 135

Figure 6.19: Immersed (top) and not immersed (bottom), center crack specimen with notch radius $r_n / \alpha = 10^{-3}$ loaded in Mode I at $\epsilon^\infty = 0.5$, from left to right: before loading, after instantaneous loading and at equilibrium. Note that the notch is not even visible in the initial configuration.136

Figure 6.20: Evolution of the transient J-integral obtained from an immersed and a not immersed notched model, with notch radius $r_n / \alpha = 10^{-3}$ loaded in Mode I at $\mathcal{E}^\infty = 0.5$. Stage I refers to loading, and stage II to the transient relaxation.....138

Chapter 1

Introduction

Hydrogels consist of crosslinked polymer chains and solvent molecules (e.g., water). The crosslinked polymer chains form a three-dimensional network structure through which the smaller solvent molecules can migrate. The response of hydrogels to external forces or chemical stimuli is generally a transient process, involving solvent diffusion and deformation coupled via the chemo-mechanical interactions between the polymer network and the solvent. In addition, hydrogels are also responsive to diverse stimuli, such as electric and magnetic fields, temperature, and light.

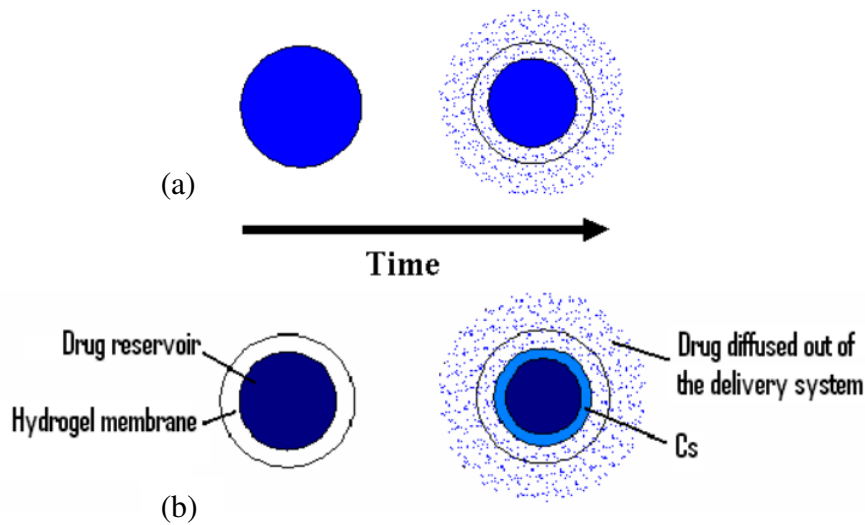


Figure 1.1: Hydrogel used in drug delivery. (Pal et al., 2009)

1.1 MOTIVATION

Hydrogels have been used in many bioengineering applications, due to their biointegrability, physical similarity to natural tissue and other physical characteristics, and their transient response is often a key feature in these applications. Some of these bioengineering applications include drug delivery, tissue engineering, microfluidics, and

artificial muscles (Abidian et al., 2009; Drury et al., 2003; Beebe et al., 2000; Lee et al., 2010; Tokarev et al., 2009; Galaev et al., 1999; Jeong et al., 1997; Peppas et al., 2006; Qiu et al., 2001; Ulijn et al., 2007; Suciu et al., 2004; Jagur-Grodzinski 2006). There is also a great deal of interest and development in hydrogel applications in other areas. Hydrogels have been used for sensors and actuators (Holtz et al., 1997; Harmon et al., 2003), energy storage devices (Nohara et al., 2003; Sun et al., 2004), swellable packers in the oil industry (Al-Khelaiwi et al., 2010), spatially programmable 3D structures (Palleau et al., 2013), and soft machines/robots (Morales et al., 2014).

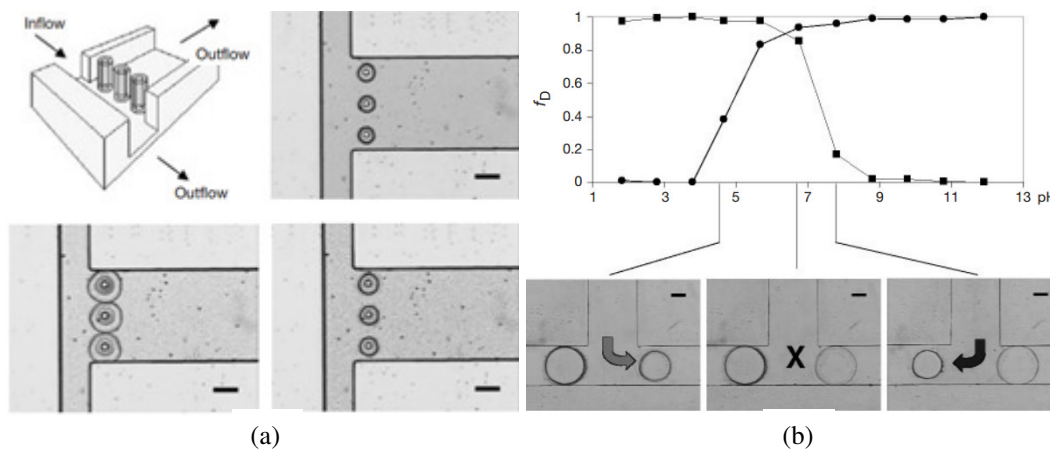


Figure 1.2: Flow control in microfluidic applications. (Beebe et al., 2000)

In their application as vessels for drug delivery (Figure 1.1), hydrogels can be used in two ways; (Figure 1.1a) encapsulating drug particles in an unswollen state of the hydrogel between the polymer chains and releasing the particles directly at the target when the hydrogel starts swelling, and also (Figure 1.1b) using the hydrogel as a permeable membrane that encapsulates a biodegradable carrier for the drug particles and again controlling the release rate of the drug particles (Pal et al., 2009). In a similar way, by swelling/de-swelling of hydrogel pillars, a microfluidics channel (Figure 1.2) is controlled by (a) stopping the flow and (b) changing the direction of the flow based on

the pH of the solvent that flows in the channel. The use of multiple hydrogel pillars can accelerate the response time of the array (Beebe et al., 2000).

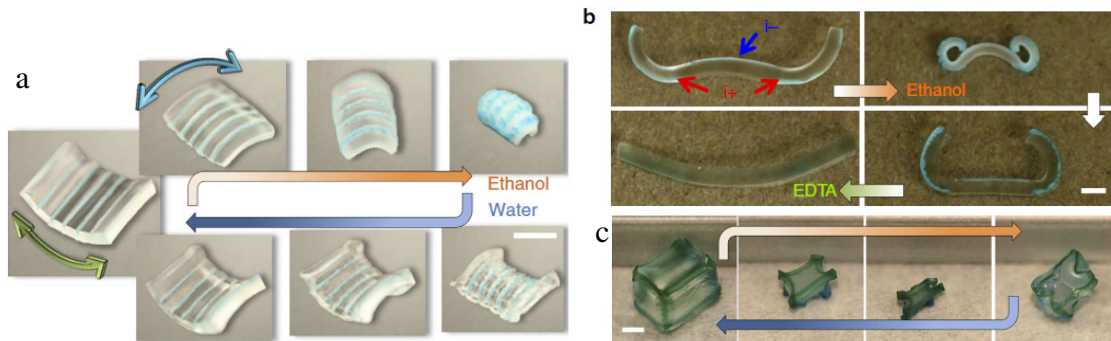


Figure 1.3: Spatially and sequentially programmable 3D patterned shapes. Hydrogels can transform with solvent absorption and desorption. (Palleau et al., 2013)

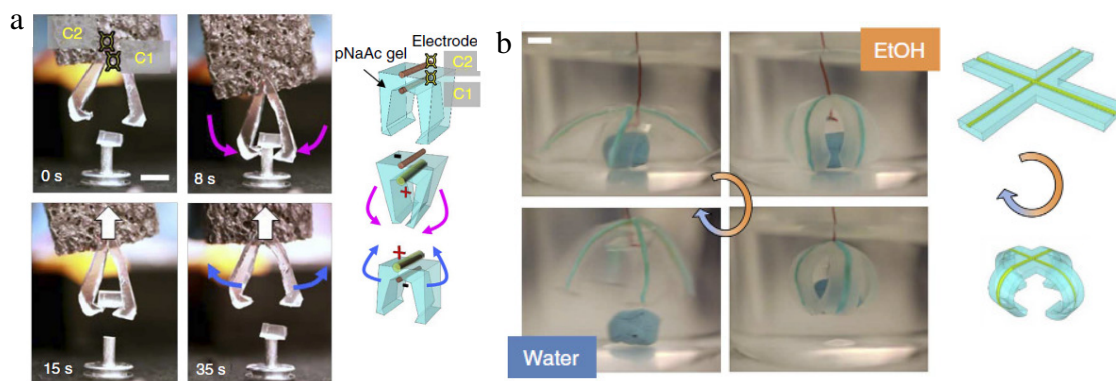


Figure 1.4: Electrically activated hydrogel robots. (Palleau et al., 2013)

On-demand, three dimensional hydrogel structures, with sequentially and spatially programmable features (Figure 1.3) can be created with the use of ionoprinting. Regions that undergo ionoprinting become stiffer and control the response to solvent migration, leading to a time-dependent shape transformation following the immersion of the hydrogel in solvent (Palleau et al., 2013). Soft machines made of hydrogels are often designed utilizing the response of hydrogels to electric field. In Figure 1.4 the application of a potential to the electrodes leads to a stress distribution that opens and closes the arms

capturing and releasing the target objects (Palleau et al., 2013). Also, in Figure 1.5 a polyelectrolyte hydrogel structure made of an anionic and a cationic leg, actuated by the application of an electric field in an ionic aqueous solution, moves without the use of an external mechanical input. The direction of motion is dictated by the sign of the fixed charges in the polyelectrolyte network and the applied field (Morales et al., 2014).

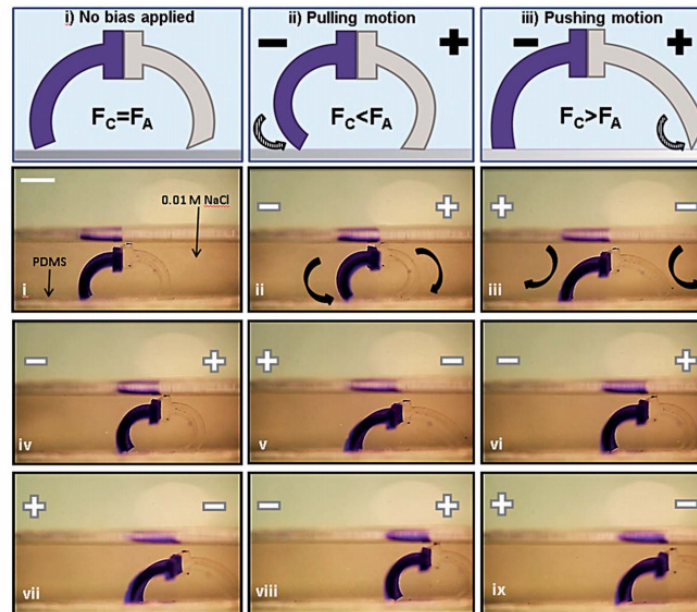


Figure 1.5: Actuation process of walking hydrogel robots. (Morales et al., 2014)

Cartilage in joints can also be replaced by hydrogels (Suciu et al., 2004), and in such cases where the hydrogel acts a structural component, it is important to maintain the structural integrity of the system. One macroscopic failure mode of hydrogels is fracture, which is influenced by the type of loading and the low toughness of the hydrogels (Figure 1.6). In order to prevent fracture of hydrogels, double network hydrogels have been devised to enhance the toughening (Gong et al., 2003). Mechanisms to restore the

integrity of the gels once they have been damaged have also been employed (Zhao et al., 2014).

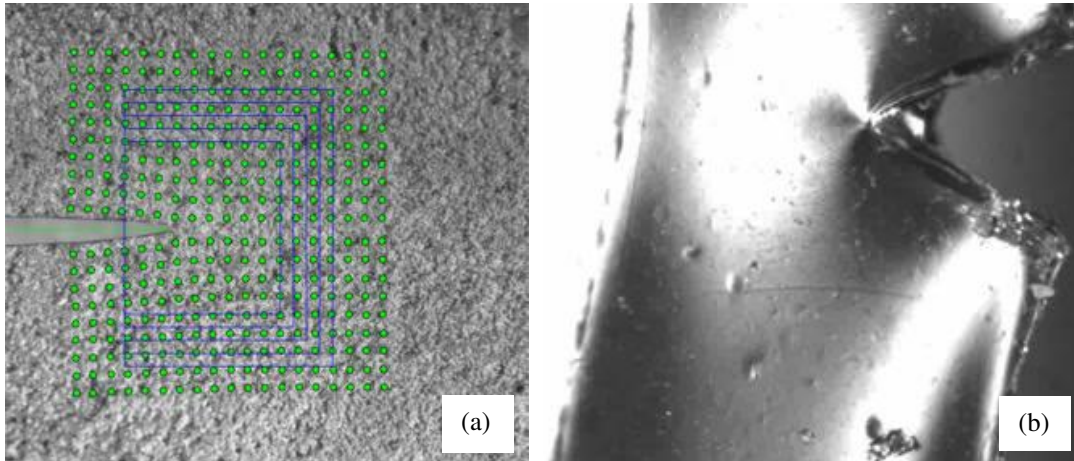


Figure 1.6: Hydrogel fracture (Kwon et al., 2011; <http://www.ppm.d.espci.fr/spip.php?article250&lang=fr>)

1.2. THEORIES AND NUMERICAL METHODS

Both linear and nonlinear theories have been proposed to model the transient responses of hydrogels subject to various mechanical and chemical conditions. Tanaka et al. [1973] derived a linear diffusion equation by treating the gel as a mixture of solid and liquid with a coefficient of friction for the interaction. Another linear approach was proposed by Scherer [1989], who extended the linear poroelasticity theory to model the gel as a continuum phase with solvent concentration and pore pressure. Recently, the theory of linear poroelasticity has been used extensively in combination with experimental measurements for characterizing the mechanical and transport properties of polymer gels (Hui et al., 2006; Galli et al., 2009; Hu et al., 2010; Yoon et al., 2010; Chan et al., 2012; Kalcioğlu et al., 2012). In spite of its remarkable success, it is well known that the linear theory is limited to relatively small deformation, while large deformation is

common for hydrogels. On the other hand, a variety of nonlinear approaches have been proposed for coupling large deformation and transport processes in gels (Dolbow et al., 2004; Hong et al., 2008; Birgersson et al., 2008; Doi, 2009; Chester and Anand, 2010; Duda et al., 2010; Wang and Hong, 2012) .

To capture the full response of hydrogels to environmental stimuli, the finite element method is mainly used to numerically solve the boundary value problems that arise. Previously, finite element methods for equilibrium analyses of hydrogels were developed (Hong et al., 2009a; Kang and Huang, 2010a) without considering the diffusion kinetics. More recently, several implementations of transient finite element methods for hydrogels have been reported (Zhang et al., 2009; Wang and Hong, 2012; Lucantonio et al., 2013; Toh et al., 2013).

Transient finite element methods, applied using the theory of poroelasticity, have also been developed in the past, even though it was primarily in the field of geomechanics. These methods can provide intuition for the study and development of transient mixed-finite element methods necessary for the study of hydrogels using the nonlinear theories that have been proposed. Vermeer and Verruijt [1981], Zienkiewicz et al. [1990], Borja [1986], Murad and Loula [1992 and 1994], Wan [2002], and Phillips [2005] have all studied consolidation problems with finite element methods using the theory of poroelasticity. The study of finite element methods for incompressible elasticity (Phillips et al., 2009; Hughes, 1987) is also relevant to the implementation of finite element methods for the transient response of hydrogels.

1.3. SCOPE OF STUDY

The present study focuses on the transient behavior of hydrogels, and on the consistent modeling and numerical analysis of boundary value problems that arise in the

study of the response of hydrogel materials. This dissertation will be organized as follows.

Chapter 1 presents a short introduction to the study of hydrogels, summarizes the applications that have motivated this study, and presents theories and numerical approaches that have been used to study hydrogels.

Chapter 2 includes a comparison of the nonlinear theory for hydrogels by Hong et al. [2009a] to the theory of linear poroelasticity specified for gels with incompressible constituents. The theories are proven to be consistent through a perturbation analysis in the small deformation regime. Examples for substrate-constrained and free hydrogel swelling are numerically solved using both theories, and fitting to experimental results with each theory is discussed.

Chapter 3 presents the finite element formulation and implementation of a mixed finite element method using the backward Euler scheme for time integration and the Newton-Raphson method for solving the nonlinear problem iteratively for both a compressible and an incompressible constitutive behavior based on the nonlinear theories that are presented in the chapter. Issues regarding the numerical stability of the method are also discussed.

Chapter 4 validates the proposed finite element method by examining the problem of constrained swelling and comparing numerical results to the solutions obtained in Chapter 2. Swell induced instability is also discussed, focusing on the response of a hydrogel bilayer.

Chapter 5 discusses the problem of indentation of hydrogel layers under a flat rigid punch. Examples are solved using the proposed finite element method, and the characterization of hydrogel properties based on indentation experiments is studied.

Chapter 6 considers the effect of diffusion in hydrogel fracture. First, a consistent method using nonequilibrium thermodynamics is proposed to obtain the energy release rate for crack propagation using a modified path independent transient J-integral that takes into account the dissipation due to diffusion. Numerical examples are considered for sharp crack and blunted crack models, and the possibility of delayed fracture is discussed.

Finally, in Chapter 7 the conclusions of this study are presented along with future directions for research in this field.

Chapter 2

Swelling Kinetics of Polymer Gels: Comparison of Linear and Nonlinear Theories¹

A polymer gel swells significantly when imbibing a large amount of solvent (e.g., water). Swelling is a kinetic process coupling mass transport and mechanical deformation, which depends on the interaction between the polymer network and the solvent. Both linear and nonlinear theories have been used to describe or predict the swelling kinetics of polymer gels under various conditions. Tanaka (1973 & 1979) derived a linear diffusion equation by treating the gel as a mixture of solid and liquid with a coefficient of friction for the interaction. Alternatively, Scherer (1989 & 1992) proposed a linear theory treating the gel as a continuum phase with the pore pressure (or solvent concentration) as a state variable. The linear theory by Scherer is equivalent to the linear poroelasticity theory originally proposed by Biot (1941) for soil consolidation. The two linear approaches have been compared (Johnson, 1982; Hui et al., 2005), and considerable differences were noted. Hui et al. (2005) proposed an extension to the approach by Tanaka (1973 & 1979), with which the two linear theories become identical. Recently, the theory of linear poroelasticity has been used extensively in combination with experimental measurements for characterizing the mechanical and transport properties of polymer gels (Hui et al., 2006; Galli et al., 2009; Hu et al., 2010, 2011 & 2012; Yoon et al., 2010; Chan et al., 2012; Kalcioglu et al., 2012). In spite of remarkable success, it is well known that the linear theory is limited to relatively small deformation, while large deformation is common for polymer gels. On the other hand, a variety of nonlinear approaches have been proposed for coupling large deformation and transport

¹ Bouklas, N., & Huang, R. (2012). Swelling kinetics of polymer gels: comparison of linear and nonlinear theories. *Soft Matter*, 8(31), 8194-8203. Professor Rui Huang was the supervisor of this work

processes in polymer gels (Durning et al., 1993; Barriere et al., 2003; Rajagopal, 2003; Baek et al., 2004; Dolbow et al., 2004; Ji et al., 2006; Birgersson et al., 2008; Hong et al., 2009a; Duda et al., 2010; Chester et al., 2010). A comparison between the linear and nonlinear approaches would define the range of applicability for the linear theory. Moreover, a consistent nonlinear theory would extend the properties determined in the linear regime to the nonlinear regime, provided that the physical parameters in the nonlinear theory can be properly related to those in the linear theory.

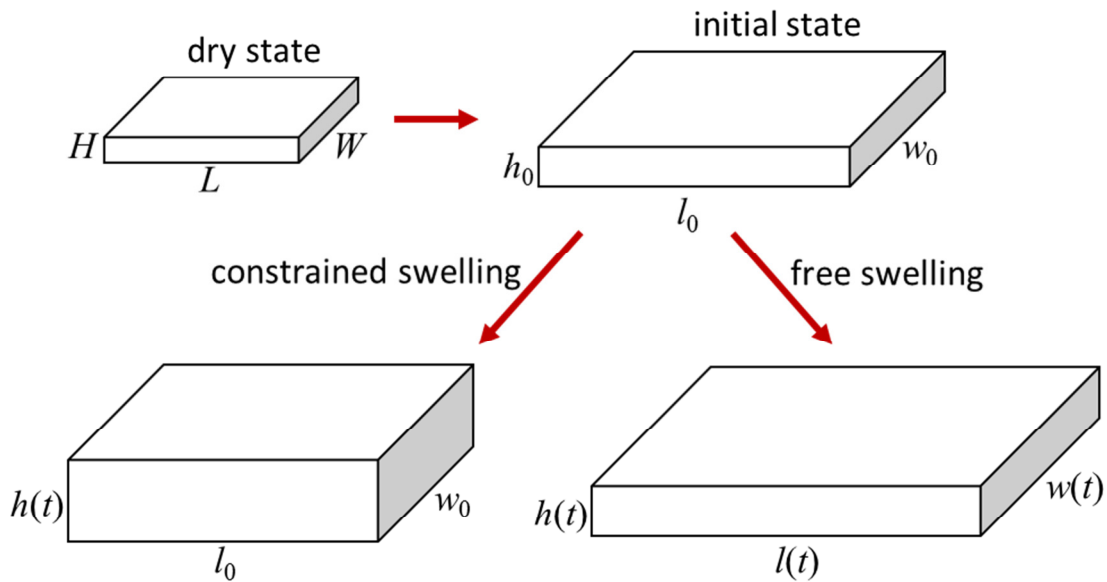


Figure 2.1: Schematic illustration of a thin hydrogel layer, subject to constrained or free swelling. In the present study, the initial state is assumed to be isotropically swollen from the dry state with $h_0/H = l_0/L = w_0/W = \lambda_0$.

In this chapter, we present a comparison between the nonlinear theory by Hong et al. (2009a) and the linear poroelasticity theory. We show that the two theories are consistent within the linear regime under the condition of small perturbation from an isotropically swollen state of the gel. As specific examples, we consider swelling kinetics of both substrate-constrained and freestanding hydrogel layers immersed in a solvent (Fig. 2.1). Although the linear poroelasticity theory can be used to fit the experimental data for both the constrained and free swelling kinetics (Yoon et al., 2010), it is cautioned that the applicability of the linear theory should be limited to relatively small swelling ratios. For large swelling ratios, we suggest a new procedure to fit the experimental data with the nonlinear theory. Finally, we discuss the indentation relaxation experiment as an effective method for characterizing the mechanical and transport properties of polymer gels within the linear regime but with possible extensions to the nonlinear regime.

2.1. A NONLINEAR THEORY

Here we briefly summarize the nonlinear theory of polymer gels by Hong et al. [2009a]. First, the constitutive behavior of a gel is described by using a free energy function. For a specific material model, the free energy density function based on the Flory-Rehner theory (Flory and Rehner, 1943; Flory 1953), takes the form

$$U(\mathbf{F}, C) = U_e(\mathbf{F}) + U_m(C) \quad (2.1)$$

$$U_e(\mathbf{F}) = \frac{1}{2} N k_B T \left[F_{iK} F_{iK} - 3 - 2 \ln(\det(\mathbf{F})) \right] \quad (2.2)$$

$$U_m(C) = \frac{k_B T}{\Omega} \left(\Omega C \ln \frac{\Omega C}{1 + \Omega C} + \frac{\chi \Omega C}{1 + \Omega C} \right) \quad (2.3)$$

where $F_{iJ} = \partial x_i / \partial X_J$ is the deformation gradient mapping the reference frame X_J to the current frame x_i , and C is the nominal solvent concentration (i.e., number of solvent molecules per unit volume of polymer). Here, N is the effective number of polymer chains per unit volume of the polymer, χ is the Flory parameter for interaction between the solvent and the polymer, Ω is the volume per solvent molecule, T is the absolute temperature, and k_B is the Boltzmann constant.

Next assume that the volume of the gel changes only by solvent absorption/desorption so that

$$1 + \Omega C = \det(\mathbf{F}) \quad (2.4)$$

which imposes a constraint coupling deformation (\mathbf{F}) with the solvent concentration (C) in the gel. Eq. (2.4) implies that both the polymer network and solvent are incompressible. Using a Lagrange multiplier (Π), the free energy density function is rewritten as

$$U(\mathbf{F}, C) = U_e(\mathbf{F}) + U_m(C) + \Pi[1 + \Omega C - \det(\mathbf{F})] \quad (2.4)$$

The chemical potential and nominal stress in the gel are obtained as the thermodynamic work conjugates, namely

$$\mu = \frac{\partial U}{\partial C} = k_B T \left[\ln \frac{\Omega C}{1 + \Omega C} + \frac{1}{1 + \Omega C} + \frac{\chi}{(1 + \Omega C)^2} \right] + \Omega \Pi \quad (2.6)$$

$$s_{iJ} = \frac{\partial U}{\partial F_{iJ}} = N k_B T \left(F_{iJ} - \frac{1}{2} \left(\frac{1}{\det(\mathbf{F})} + \frac{\Pi}{N k_B T} \right) e_{ijk} e_{JKL} F_{jK} F_{kL} \right) \quad (2.7)$$

where e_{ijk} is the alternating unit tensor.

In the absence of body forces, mechanical equilibrium of the gel requires that

$$\frac{\partial s_{ij}}{\partial X_j} = 0 \quad (2.8)$$

When the gel reaches a state of chemical equilibrium, the chemical potential is a constant everywhere. In the transient state, however, the gradient of the chemical potential drives solvent migration. By a diffusion model, the true flux of solvent at the current state is given as (Hong et al., 2009a):

$$j_k = -\frac{cD}{k_B T} \frac{\partial \mu}{\partial x_k} \quad (2.9)$$

where D is a constant for solvent diffusivity, c is the true solvent concentration which is related to the nominal concentration as $c = C / \det(\mathbf{F})$.

The nominal flux by definition is related to the true flux as: $J_K N_K dS_0 = j_k n_k dS$, where N_K and n_k are the unit normal in the reference and current frames, respectively. The differential areas, dS_0 and dS , are related as $F_{iK} n_i dS = \det(\mathbf{F}) N_K dS_0$. Thus, by (2.9) the nominal flux is obtained as

$$J_K = \det(\mathbf{F}) \frac{\partial X_K}{\partial x_k} j_k = -M_{KL} \frac{\partial \mu}{\partial X_L} \quad (2.10)$$

through which a nominal mobility tensor is defined as

$$M_{KL} = \frac{D}{\Omega k_B T} \left(\frac{\partial X_K}{\partial x_k} \frac{\partial X_L}{\partial x_k} \right) [\det(\mathbf{F}) - 1] \quad (2.11)$$

By conservation of solvent molecules, the evolution equation for the nominal solvent concentration is

$$\frac{\partial C}{\partial t} = -\frac{\partial J_K}{\partial X_K} = \frac{\partial}{\partial X_K} \left(M_{KL} \frac{\partial \mu}{\partial X_L} \right) \quad (2.12)$$

Therefore, a complete set of governing equations by the nonlinear theory includes the field equations in (2.8) and (2.12) along with the constitutive relations in (2.6), (2.7),

and (2.10). In such a theory, the intrinsic material properties of the gel are specified by four independent quantities: N , χ , Ω , and D .

2.2. A LINEAR THEORY

The theory of linear poroelasticity, originally developed by Biot (1941) for soil consolidation, has been extended to gels (Scherer, 1989 & 1992; Johnson, 1982; Hui et al., 2005 & 2006; Galli et al., 2009; Hu et al., 2010, 2011 & 2012; Yoon et al., 2010; Chan et al., 2012; Kalcioglu et al., 2012). In this section, by linearizing the equations of the nonlinear theory at the vicinity of an isotropically swollen state, we derive a set of linear equations for comparison with the theory of linear poroelasticity. With such, the relationship between the nonlinear and linear theories is established, and the material properties used in the linear theory are defined consistently based on the nonlinear theory.

The gel is assumed to be stress free and isotropically swollen at the initial state, with a swelling ratio λ_0 relative to the dry state in all directions. By setting $s_{iJ} = 0$ in (2.7), the Lagrange multiplier Π is obtained, and by (2.6) the corresponding chemical potential for the initial state is

$$\frac{\mu_0}{k_B T} = \ln \frac{\lambda_0^3 - 1}{\lambda_0^3} + \frac{1}{\lambda_0^3} + \frac{\chi}{\lambda_0^6} + N\Omega \left(\frac{1}{\lambda_0} - \frac{1}{\lambda_0^3} \right) \quad (2.14)$$

Now consider a small perturbation to the initial state with a displacement field u_i . Relative to the initial state, a linear strain field is defined as

$$\varepsilon_{ij} = \frac{1}{2} \left(\frac{\partial u_i}{\partial x_j} + \frac{\partial u_j}{\partial x_i} \right) \quad (2.15)$$

By (2.4), the volumetric part of the strain is related to the change of solvent concentration, namely

$$\varepsilon_{kk} = \Omega(c - c_0) \quad (2.16)$$

where the concentration c is the number of solvent molecules per unit volume of the gel at the initial state, and c_0 is the initial concentration that is related to the initial swelling ratio as $\Omega c_0 = 1 - \lambda_0^{-3}$.

Next we linearize the constitutive equations (2.6) and (2.7) at the vicinity of the initial state. For the chemical potential, we obtain that

$$\mu \approx \mu_0 + k_B T \left[\frac{1}{\lambda_0^3 (\lambda_0^3 - 1)} - \frac{2\chi}{\lambda_0^6} \right] \varepsilon_{kk} + \Omega \delta \Pi \quad (2.17)$$

where $\delta \Pi$ is the perturbation to the Lagrange multiplier associated with the displacement field.

The Cauchy stress in the gel is related to the nominal stress as $\sigma_{ij} = s_{iK} F_{jK} / \det(\mathbf{F})$. After linearization, we obtain that

$$\sigma_{ij} \approx \frac{2Nk_B T}{\lambda_0} \varepsilon_{ij} - (\Pi_0 \varepsilon_{kk} + \delta \Pi) \delta_{ij} \quad (2.18)$$

where

$$\Pi_0 = Nk_B T \left(\frac{1}{\lambda_0} - \frac{1}{\lambda_0^3} \right) \quad (2.19)$$

Combining (2.27) and (2.28) to eliminate $\delta \Pi$, we obtain the Cauchy stress in the form

$$\sigma_{ij} = 2G \left[\varepsilon_{ij} + \frac{\nu}{1-2\nu} \varepsilon_{kk} \delta_{ij} \right] - \frac{\mu - \mu_0}{\Omega} \delta_{ij} \quad (2.20)$$

where

$$G = \frac{1}{\lambda_0} Nk_B T \quad (2.21)$$

$$\nu = \frac{1}{2} - \frac{N\Omega}{2} \left[\frac{1}{\lambda_0^2 (\lambda_0^3 - 1)} + \frac{N\Omega}{\lambda_0^2} - \frac{2\chi}{\lambda_0^5} \right]^{-1} \quad (2.22)$$

As shown in Appendix A, G and ν are the shear modulus and Poisson's ratio of the swollen gel in the linear elastic regime; Similar relations were obtained by Hu et al. (2011).

Furthermore, linearizing the mechanical equilibrium equation in (2.8) leads to

$$\frac{\partial \sigma_{ij}}{\partial x_j} = 0 \quad (2.23)$$

By (2.9), the solvent flux at the vicinity of the initial state is approximately

$$j_k = -\frac{c_0 D}{k_B T} \frac{\partial \mu}{\partial x_k} = -M_0 \frac{\partial \mu}{\partial x_k} \quad (2.24)$$

where

$$M_0 = \frac{D}{\Omega k_B T} \frac{\lambda_0^3 - 1}{\lambda_0^3} \quad (2.25)$$

By mass conservation, a linear evolution equation for the solvent concentration is obtained as

$$\frac{\partial c}{\partial t} = -\frac{\partial j_k}{\partial x_k} = M_0 \frac{\partial^2 \mu}{\partial x_k \partial x_k} \quad (2.26)$$

Therefore, based on the nonlinear theory, a complete set of linear equations can be developed, consisting of Eqs. (2.23) and (2.26) for the field equations along with Eqs. (2.20) and (2.24) as the constitutive relations. The linear kinematics is described by Eqs. (2.15) and (2.16). Moreover, three material parameters for the linear equations are defined in Eqs. (2.21), (2.22), and (2.25), which depend on the swelling ratio (λ_0) at the initial state.

In comparison with Biot's theory of linear poroelasticity, we note that the linear relation in Eq. (2.20) is identical to its counterpart in linear poroelasticity with the pore

pressure, $p = (\mu - \mu_0) / \Omega$. Furthermore, Darcy's law in linear poroelasticity is equivalent to Eq. (2.24) by setting

$$M_0 = \frac{k}{\eta \Omega^2} \quad (2.26)$$

where k is the permeability of the polymer network and η is the viscosity of the solvent. All the other equations then become identical to Biot's theory. Therefore, the linear poroelasticity theory may be considered as a specialization of the nonlinear theory in the linear regime. In addition to the linear elastic shear modulus and Poisson's ratio in (2.21) and (2.22), the linear poroelastic property, k / η , is related to the intrinsic diffusivity D and the swelling ratio λ_0 by Eq. (2.26) and (2.24).

The linear equations can be further reduced by inserting (2.20) into (2.23):

$$G \left[\frac{\partial^2 u_i}{\partial x_j \partial x_j} + \frac{1}{1-2\nu} \frac{\partial^2 u_j}{\partial x_j \partial x_i} \right] = \frac{1}{\Omega} \frac{\partial \mu}{\partial x_i} \quad (2.27)$$

Next inserting (2.27) into (2.25), we obtain that

$$\frac{\partial c}{\partial t} = D^* \frac{\partial^2 c}{\partial x_j \partial x_j} \quad (2.28)$$

which takes the form of a linear diffusion equation in terms of the solvent concentration, with an effective diffusivity

$$D^* = \frac{2(1-\nu)\Omega^2 G M_0}{1-2\nu} \quad (2.30)$$

Note that the effective diffusivity defined in (2.30) differs from the intrinsic diffusivity introduced in (2.9) for the nonlinear theory. The effective diffusivity, also called the cooperative diffusion coefficient (Hui et al., (2006)), is a combined quantity that depends on the initial state for the development of the linear theory.

2.3. SWELLING OF HYDROGEL LAYERS

In this section we consider swelling kinetics for two cases (Fig. 2.1), one for a hydrogel layer laterally constrained by a rigid substrate and the other for a freestanding hydrogel layer immersed in a solvent. In both cases, we assume that the lateral dimensions of the hydrogel layer are much larger than the thickness ($L, W \gg H$) and hence ignore the edge effects. In each of the two cases we solve the transient problem based on the nonlinear theory and compare with the corresponding solution based on the linear theory. The detailed solution procedure is presented in Appendix B, and the main results are discussed here.

2.3.1. Constrained swelling

Consider a layer of hydrogel with one face ($X=0$) attached to a rigid substrate and the other face ($X=H$) exposed to a solvent, where H is the layer thickness at the dry state. Initially the gel is swollen isotropically with a swelling ratio λ_0 (Figure 2.1). As more solvent molecules migrate into the gel, the gel swells in the thickness direction while the lateral dimensions are fixed by the substrate. Therefore, the stretch in the thickness direction is a function of time and position, $\lambda_2 = \lambda_2(X_2, t)$, whereas $\lambda_1 = \lambda_3 = \lambda_0$. By the nonlinear theory, the thickness swelling ratio can be obtained by solving a nonlinear diffusion equation

$$\lambda_0^2 \frac{\partial \lambda_2}{\partial t} = D \frac{\partial}{\partial X_2} \left(\xi \frac{\partial \lambda_2}{\partial X_2} \right) \quad (2.31)$$

where

$$\xi(\lambda_2) = \frac{1}{\lambda_0^2 \lambda_2^4} - \frac{2\chi(\lambda_0^2 \lambda_2 - 1)}{\lambda_0^4 \lambda_2^5} + N\Omega \frac{(\lambda_0^2 \lambda_2 - 1)(\lambda_2^2 + 1)}{\lambda_0^2 \lambda_2^4} \quad (2.32)$$

Equation (2.31) is to be solved with the initial condition, $\lambda_2(t=0) = \lambda_0$, and the boundary conditions including: (i) $s_{22}(X_2=H) = 0$; (ii) $\mu(X_2=H) = 0$; and (iii)

$J_2(X_2 = 0) = 0$, where H is the layer thickness at the dry state. The first two boundary conditions together require an instantaneously equilibrium swelling ratio at the upper surface, $\lambda_2(X_2 = H) = \lambda_\infty^c$, which can be obtained by solving a nonlinear algebra equation

$$\ln\left(\frac{\lambda_0^2 \lambda_\infty^c - 1}{\lambda_0^2 \lambda_\infty^c}\right) + \frac{1}{\lambda_0^2 \lambda_\infty^c} + \frac{\chi}{\lambda_0^4 (\lambda_\infty^c)^2} + \frac{N\Omega}{\lambda_0^2} \left(\lambda_\infty^c - \frac{1}{\lambda_\infty^c}\right) = 0 \quad (2.33)$$

The zero flux condition at the lower surface requires that

$$\left(\frac{\partial \lambda_2}{\partial X_2}\right)_{X_2=0} = 0 \quad (2.34)$$

With the boundary conditions (2.33) and (2.34), a finite difference method is used to numerically integrate the nonlinear diffusion equation (2.31) (Appendix B). Figure 2.2a shows the numerical results, with λ_2 as a function of X_2 for increasing time, where the time is normalized by the characteristic time scale of diffusion, $\tau_1 = H^2 / D$. Apparently, a sharp gradient of the swelling ratio develops near the upper surface at the early stage of swelling. Correspondingly, the solvent concentration, $C = (\lambda_0^2 \lambda_2 - 1) / \Omega$, and the swell-induced compressive stress are both inhomogeneous at the transient state. In particular, the compressive stress as shown in Fig. 2.2b may cause surface instability to form wrinkles and creases as observed experimentally (Tanaka et al., 1987, Trujill et al., 2008). For the present study we assume the surface to remain flat during swelling. After a long time ($t \rightarrow \infty$), the hydrogel approaches the homogeneous equilibrium state with $\lambda_2 = \lambda_\infty^c$ everywhere. By (2.33), the equilibrium swelling ratio depends on the initial swelling ratio (λ_0) as well as two dimensionless parameters, $N\Omega$ and χ .

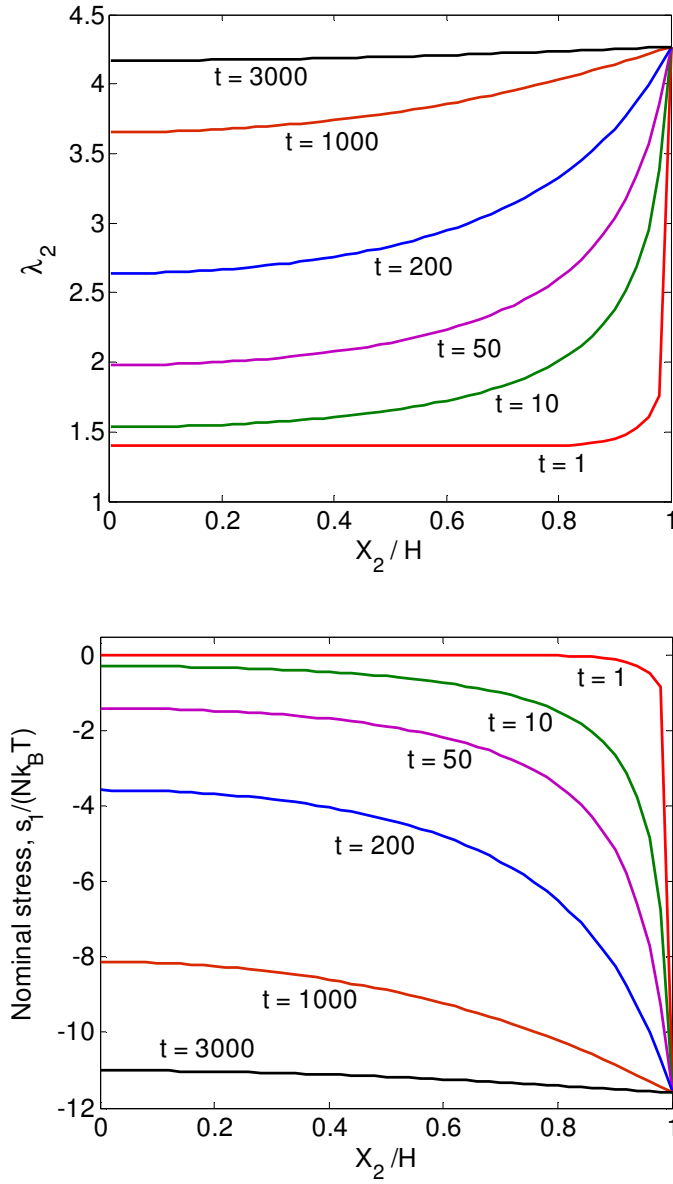


Figure 2.2: Evolution of (a) stretch and (b) swelling induced compressive stress in a constrained hydrogel layer by the nonlinear theory, with $N\Omega = 0.001$, $\chi = 0.4$, and $\lambda_0 = 1.4$. The time is normalized by $\tau_1 = H^2 / D$.

With the transient swelling ratio $\lambda_2(X_2, t)$, the thickness of the hydrogel layer can be calculated as

$$h(t) = \int_0^H \lambda_2(X_2, t) dX_2 \quad (2.35)$$

Figure 2.3a plots the relative thickness swelling ratio, $h(t)/h_0$, as a function of time for different values of χ , with the initial thickness $h_0 = \lambda_0 H$. In all cases, the thickness increases rapidly at the early stage and eventually approaches the equilibrium state with $h_\infty/h_0 = \lambda_\infty^c/\lambda_0$. As the equilibrium swelling ratio increases with decreasing χ , the time to reach the equilibrium state increases.

At the limit of short time ($t \rightarrow 0$), the diffusion equation (2.31) can be linearized, yielding a self-similar solution, namely

$$\frac{\lambda_2 - \lambda_0}{\lambda_\infty^c - \lambda_0} = \text{erfc} \left(\frac{\lambda_0 (H - X_2)}{2\sqrt{\xi(\lambda_0)Dt}} \right) \quad (2.36)$$

The thickness change of the hydrogel layer is then obtained as

$$\Delta h(t) = \int_{-\infty}^H (\lambda_2 - \lambda_0) dX_2 = 2 \left(\frac{\lambda_\infty^c}{\lambda_0} - 1 \right) \sqrt{\frac{\xi(\lambda_0)Dt}{\pi}} \quad (2.37)$$

As shown in Fig. 2.3b, the thickness change obtained numerically by the finite difference method scales with \sqrt{t} in a window, roughly $0.1 < t/\tau_1 < 10$. The accuracy of the numerical method is limited by the spatial step ΔX . To reduce the numerical error in the early stage ($t/\tau_1 < 0.1$), we may reduce ΔX , which however would require a smaller time step Δt and thus higher computational cost for the numerical method to be stable. Alternatively, an unconditionally stable implicit method may be used to improve the numerical solution.

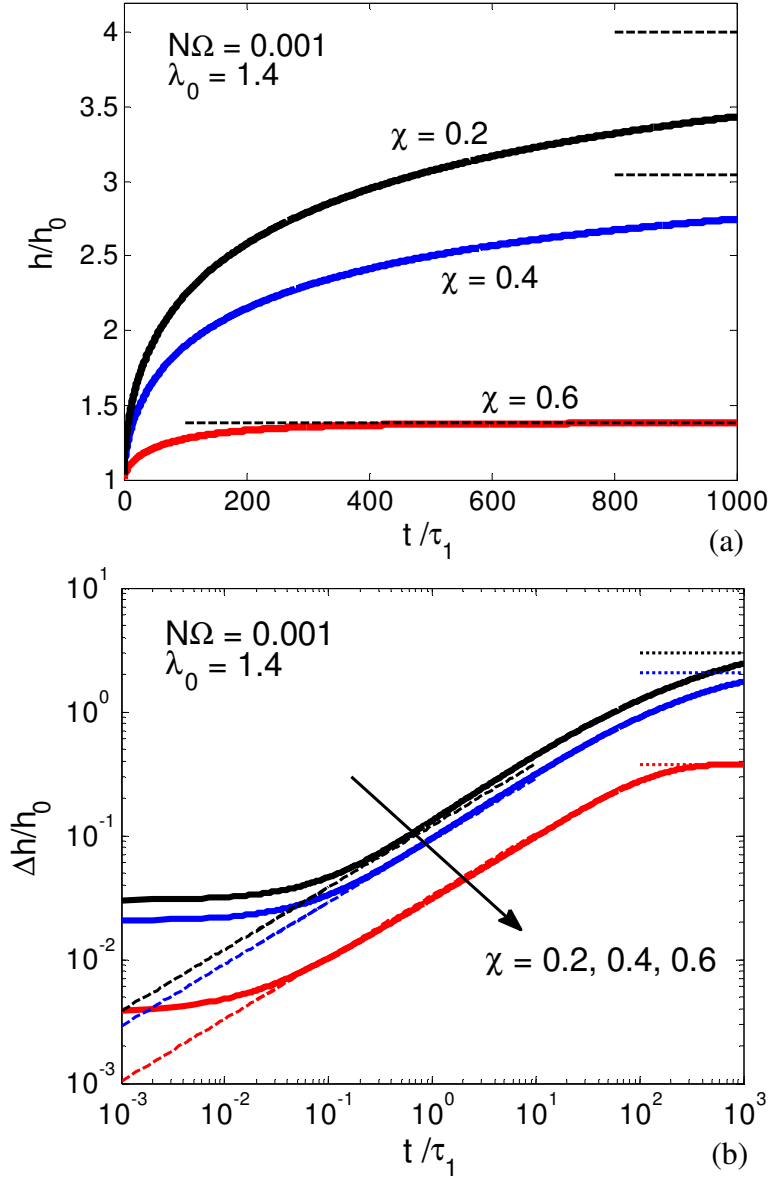


Figure 2.3: (a) Thickness swelling ratio as a function of time for constrained hydrogel layers with $N\Omega = 0.001$, $\lambda_0 = 1.4$, and different values for χ . The horizontal dashed lines indicate the equilibrium swelling ratio, $h_\infty/h_0 = \lambda_\infty^c/\lambda_0$. (b) Normalized thickness change as a function of time, in comparison with the self-similar solution (dashed lines).

It is found that the self-similar solution (2.37) tends to overestimate the swelling rate in the window $0.1 < t/\tau_1 < 10$ due to the use of $\xi(\lambda_0)$. As shown in Fig. 2.2a, the swelling ratio λ_2 is sharply graded between λ_0 and λ_∞^c near the surface during the early stage of swelling. By taking $\xi = \xi(\lambda_0 + \lambda_\infty^c)/2$ in (4.7), the self-similar solution agrees closely with the numerical solution for $0.1 < t/\tau_1 < 10$ as shown in Fig. 2.3b.

The same problem of constrained swelling was solved by using the linear poroelasticity theory (Yoon et al., 2010; Peters et al., 1986; Doi, 2009), which predicted the thickness change of the hydrogel layer as

$$\Delta h(t) = \frac{(1-2\nu)(\hat{\mu} - \mu_0)h_0}{2(1-\nu)G\Omega} \left\{ 1 - \frac{8}{\pi^2} \sum_{n=0}^{\infty} \frac{1}{(2n+1)^2} \exp\left[-(2n+1)^2 \frac{\pi^2 t}{4\tau_2}\right] \right\} \quad (2.38)$$

where $\tau_2 = h_0^2 / D^*$ defines a time scale for the linear theory and $\hat{\mu}$ is the chemical potential of the solvent in the environment. After a long time ($t \rightarrow \infty$), the gel reaches the equilibrium with $\mu = \hat{\mu}$, and the equilibrium thickness change is

$$\Delta_\infty^c = \frac{(1-2\nu)(\hat{\mu} - \mu_0)h_0}{2(1-\nu)G\Omega} \quad (2.39)$$

At the limit of short time ($t/\tau_2 \ll 1$), a self-similar solution predicts that

$$\Delta h(t) = \frac{(1-2\nu)(\hat{\mu} - \mu_0)}{(1-\nu)G\Omega} \sqrt{\frac{D^* t}{\pi}} = \frac{2\Delta_\infty^c}{h_0} \sqrt{\frac{D^* t}{\pi}} \quad (2.40)$$

The results by the nonlinear and linear theories will be compared in Section 2.4.

2.3.2. Free swelling

Without the substrate constraint, solvent molecules enter the gel layer from both upper and lower surfaces, and the gel swells in both the thickness and in-plane directions. Again, we neglect the edge effects so that the solvent molecules migrate in the thickness direction only. By symmetry, the layer remains flat (no bending), with $\lambda_2 = \lambda_2(X_2, t)$ and $\lambda_1 = \lambda_3 = \lambda_1(t)$; the stretch in the in-plane direction is a function of time only. Based on the nonlinear theory, we obtain that

$$\lambda_1^2 \frac{\partial \lambda_2}{\partial t} + 2\lambda_1 \lambda_2 \frac{d\lambda_1}{dt} = D \frac{\partial}{\partial X_2} \left(\bar{\xi} \frac{\partial \lambda_2}{\partial X_2} \right) \quad (2.41)$$

where

$$\bar{\xi}(\lambda_1, \lambda_2) = \frac{1}{\lambda_1^2 \lambda_2^4} - \frac{2\chi(\lambda_1^2 \lambda_2 - 1)}{\lambda_1^4 \lambda_2^5} + N\Omega \frac{(\lambda_1^2 \lambda_2 - 1)(\lambda_2^2 + 1)}{\lambda_1^2 \lambda_2^4} \quad (2.42)$$

Furthermore, with no constraint, the in-plane stress must be self-balanced, namely

$$\int_0^H s_{11} dX_2 = 0 \quad (2.43)$$

which leads to

$$\lambda_1^2 = \frac{1}{H} \int_0^H \lambda_2^2 dX_2 \quad (2.44)$$

Thus, the in-plane swelling ratio equals the root-mean-square (RMS) average of the out-of-plane swelling ratio.

The two nonlinear equations (2.41) and (2.44) can be solved simultaneously using a numerical method (Appendix B), with the initial and boundary conditions: (i) $\lambda_2(t=0) = \lambda_1(t=0) = \lambda_0$; (ii) $s_{22}(X_2=0, H) = 0$; and (iii) $\mu(X_2=0, H) = 0$. The boundary conditions require that the swelling ratios at the surfaces ($X_2=0$ and H) satisfy

$$\ln\left(\frac{\lambda_1^2 \lambda_2 - 1}{\lambda_1^2 \lambda_2}\right) + \frac{1}{\lambda_1^2 \lambda_2} + \frac{\chi}{\lambda_1^4 \lambda_2^2} + \frac{N\Omega}{\lambda_1^2} \left(\lambda_2 - \frac{1}{\lambda_2}\right) = 0 \quad (2.45)$$

Unlike constrained swelling, however, the swelling ratio λ_2 at the surface is not a constant value for free swelling. Instead, it depends on λ_1 and is a function of time. Figure 2.4 shows the numerical results, with λ_2 as a function of X_2 for increasing time in (a) and λ_1 as a function of time in (b). By Eq.(2.35), the thickness of the hydrogel layer is calculated as a function of time, which is also plotted in Fig. 2.4b. Apparently, the thickness swelling ratio, $h(t)/H$, follows closely with $\lambda_1(t)$, but not exactly, as expected from Eq. (2.44). Experimentally, the difference was found to be small, indistinguishable within the experimental uncertainty (Yoon et al., 2010; Li et al., 1990). In Fig. 2.4c, the nominal in-plane stress (s_{11}) is plotted as a function of X_2 for increasing time. Due to the inhomogeneous swelling ratio at the transient state, the stress is compressive near the surfaces but tensile near the center, with zero resultant force. After a long time ($t \rightarrow \infty$), the gel approaches the homogeneous equilibrium state, with an isotropic swelling ratio and zero in-plane stress. The equilibrium swelling ratio can be obtained by solving Eq. (2.45) with $\lambda_2 = \lambda_1 = \lambda_\infty^f$.

By the linear poroelasticity theory, the kinetics equation for free swelling of a hydrogel layer becomes (Yoon et al., 2010)

$$\frac{\partial \mu}{\partial t} + 4G\Omega \frac{d\varepsilon_{11}}{dt} = D^* \frac{\partial^2 \mu}{\partial x_2^2} \quad (2.46)$$

In addition, by setting $\sigma_{22} = 0$, we obtain

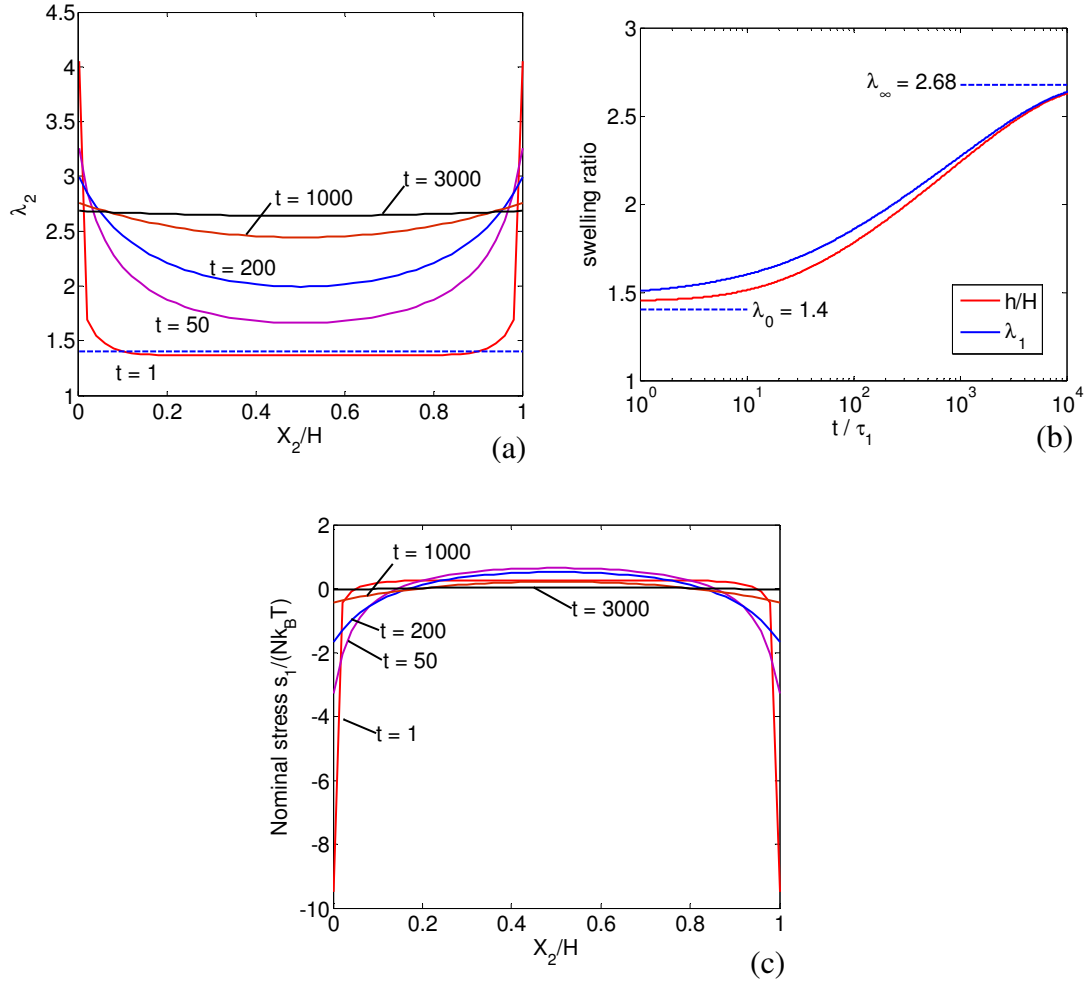


Figure 2.4: Numerical results for free swelling of a hydrogel layer by the nonlinear theory ($\chi = 0.4$, $N\Omega = 0.001$, $\lambda_0 = 1.4$): (a) swelling ratio in the thickness direction; (b) in-plane swelling ratio (λ_1) and the average thickness ratio (h/H); (c) nominal stress in the in-plane direction.

$$2G\left(\frac{1-\nu}{1-2\nu}\right)\frac{\partial u_2}{\partial x_2} + 4G\left(\frac{\nu}{1-2\nu}\right)\varepsilon_{11} = \frac{\mu - \mu_0}{\Omega} \quad (2.47)$$

By requiring a vanishing resultant force in the in-plane direction, the in-plane strain is

$$\varepsilon_{11}(t) = \frac{u_2(h_0, t) - u_2(0, t)}{h_0} \quad (2.48)$$

A numerical method is used to solve (2.46)-(2.48) for the transient kinetics of free swelling (Appendix B). In particular, no self-similar solution is found at the early stage, and the thickness change at equilibrium ($t \rightarrow \infty$) can be obtained from (2.47) and (2.48) by setting $\mu = \hat{\mu}$:

$$\Delta_\infty^f = \frac{(1-2\nu)(\hat{\mu} - \mu_0)h_0}{2(1+\nu)G\Omega} \quad (2.49)$$

2.4. RESULTS AND DISCUSSIONS

2.4.1. Linear poroelastic properties of a gel

Under the condition of small deformation, the swelling behavior of a gel can be described by the theory of linear poroelasticity (Biot et al., 1941; Scherer et al., 1989; Yoon et al., 2010). The physical parameters used in the linear theory, including the shear modulus (G), Poisson's ratio (ν), and permeability (k), are generally not intrinsic properties of the gel. Instead, they depend on the current state of the gel. On the other hand, the physical parameters in the nonlinear theory (N , χ , Ω , and) are based on a microscopic model (Flory and Rehner, 1943; Flory, 1953) and thus may be considered as intrinsic properties. For example, the shear modulus of a gel as defined in (2.21) depends on the initial swelling ratio λ_0 in addition to the polymer network, which has an initial shear modulus $Nk_p T$ at the dry state. Since the swelling ratio depends on the chemical potential, as predicted in (2.14) by the nonlinear theory, the shear modulus of the gel,

which may be measured by shear rheology, depends on the chemical potential of the environment. At the equilibrium chemical potential ($\mu=0$), the shear modulus depends on the equilibrium swelling ratio, which in turn depends on the intrinsic parameters (χ and $N\Omega$). Similarly, Poisson's ratio as defined in (2.22) also depends on the initial swelling ratio (λ_0) as well as the intrinsic properties, as shown in Figure 2.5a. Since the polymer network is assumed to be incompressible, the Poisson's ratio is 0.5 at the dry state ($\lambda_0=1$). As the swelling ratio increases, the Poisson's ratio decreases; the gel becomes compressible due to solvent absorption/desorption. For each gel with specific intrinsic properties (χ and $N\Omega$), the Poisson's ratio at the equilibrium swelling ratio corresponding to $\mu=0$ is plotted in Fig. 2.5b as a function of χ for different values of $N\Omega$. Interestingly, a sharp transition of the equilibrium Poisson's ratio is observed at $\chi \sim 0.5$, especially for gels with relatively small $N\Omega$. Thus, the Poisson's ratio of a gel is closely related to the intrinsic interaction between the polymer and the solvent. With a good solvent ($\chi \leq 0.5$), the swelling ratio is high, and the gel is highly compressible ($\nu = 0.2 \sim 0.25$) at the equilibrium swollen state.

By linear poroelasticity, the swelling kinetics depends on the ratio between permeability (k) and viscosity (η). By Eq. (2.25) and (2.27), we obtain that

$$\frac{k}{\eta} = \frac{\Omega D}{k_B T} \frac{\lambda_0^3 - 1}{\lambda_0^3} \quad (2.50)$$

Assuming a constant viscosity for the solvent, the permeability of the gel depends on the intrinsic diffusivity D as well as the swelling ratio λ_0 . The permeability is zero at the dry state ($\lambda_0=1$) and increases with increasing swelling ratio. Intuitively, it may be understood that the permeability increases as a result of an increasingly open polymer network due to swelling.

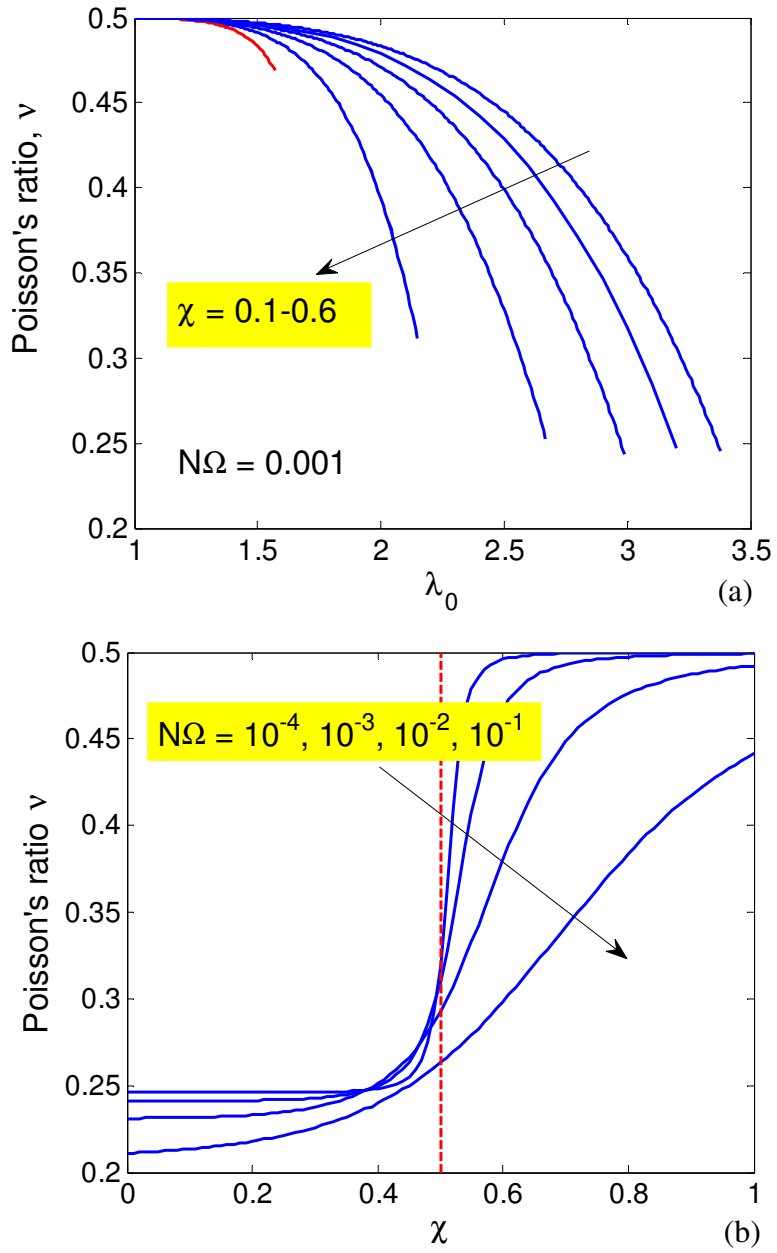


Figure 2.5: (a) Poisson's ratio as a function of the initial swelling ratio; (b) Poisson's ratio at the equilibrium swelling ratio as a function of χ .

It is noted here that the classical theory of linear poroelasticity assumes an isotropic behavior (Biot, 1941). Taking an isotropically swollen state as the initial state, we recover the classical theory by linearizing the nonlinear theory. In general, however, the initial state is not necessarily isotropic. When swelling is constrained in one or two directions, the gel swells anisotropically (Kang and Huang, 2010a). The constrained swelling of a hydrogel layer on a rigid substrate is a common example. With an anisotropic initial state, linearization of the nonlinear theory would lead to a set of linear equations for anisotropic poroelasticity. Theories of anisotropic poroelasticity have been developed for geomaterials (Biot, 1955 ; Carroll, 1979; Thomson et al., 1991; Cheng, 1997) and biomaterials, e.g., bones, in Crowin (1997) and Kohles et al. (1997) while few studies have considered poroelastic anisotropy in gels.

2.4.2. Linear vs nonlinear analysis of swelling

In Section 2.3, we present the analysis for constrained and free swelling of a hydrogel layer based on the nonlinear theory and the linear poroelasticity theory. For comparison, we plot in Fig. 2.6 the thickness ratio as a function of time for the constrained swelling, where the thickness is normalized by the initial thickness h_0 and the time is normalized by the time scale τ_1 . By Eqs. (2.21), (2.25), and (2.30), the time scale for linear poroelasticity, τ_2 , is converted to τ_1 as

$$\tau_2 = \tau_1 \frac{(1-2\nu)\lambda_0^6}{2(1-\nu)(\lambda_0^3-1)N\Omega} \quad (2.51)$$

For a specific gel with the intrinsic properties (χ and $N\Omega$), the swelling kinetics depends on the initial swelling ratio λ_0 , governed by Eq. (2.31) according to the nonlinear theory. On the other hand, the solution based on linear poroelasticity, as given in Eq. (2.38), depends on the initial chemical potential (μ_0), which can be determined by

(2.14). In addition, all the linear poroelastic properties, including G , ν , and the time scale τ_2 , depend on the initial swelling ratio. As seen in Fig. 2.6, the linear theory agrees with the nonlinear theory at the early stage of swelling, both predicting a self-similar swelling with $\Delta h \sim \sqrt{t}$, which is expected following the linearization procedure in Section 2.2. However, the equilibrium thickness change ($\Delta_\infty^c = h_\infty - h_0$) predicted by the linear theory, as given in Eq. (2.39), underestimates the equilibrium swelling in comparison with the nonlinear theory, as shown in Fig. 2.7. The discrepancy is significant when the relative swelling ratio, h_∞ / h_0 , is much greater than 1. As a result, the swelling kinetics by the linear theory deviates from the nonlinear theory beyond the early stage. Apparently, the linear theory is applicable only for relatively small swelling ratios from the initial state. The same conclusion can be drawn for the kinetics of free swelling.

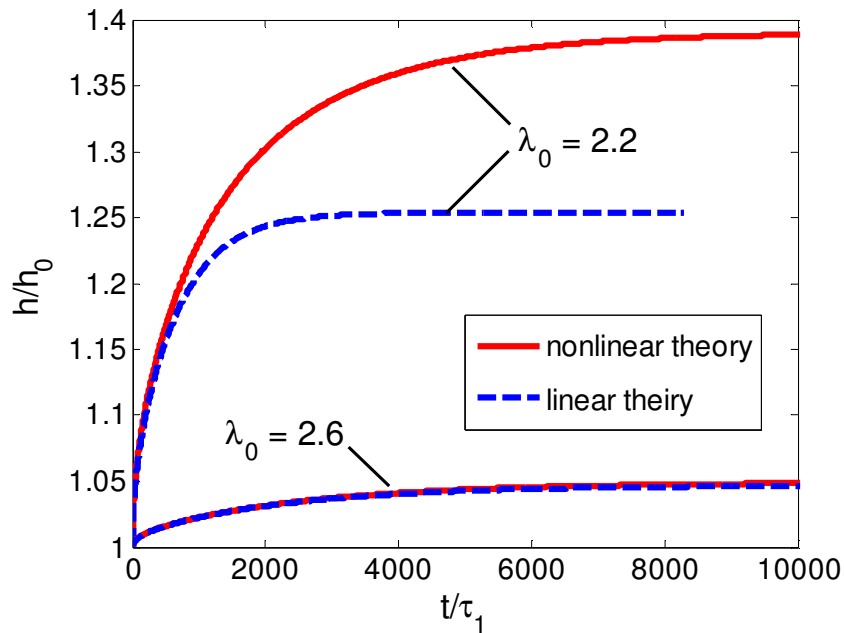


Figure 2.6: Comparison between the nonlinear theory and the linear poroelasticity for constrained swelling of a hydrogel layer ($\chi = 0.4$ and $N\Omega = 0.001$).

2.4.3. Comparison with experiments

Recently, Yoon et al. (2010) reported measurements of swelling kinetics of thin poly(N-isopropylacrylamide) (PNIPAM) hydrogel layers under both constrained and freestanding conditions. Remarkably, they found that the measured swelling kinetics compared closely with the predictions based on the theory of linear poroelasticity, despite that the relative swelling ratio (h_∞/h_0) was up to 1.8, which is apparently beyond the linear regime by the assumption of small deformation. The excellent agreement could be a fortuitous result of the fitting procedure. First, the Poisson's ratio was determined by comparing the measured thickness change at equilibrium for constrained swelling with that for free swelling. By linear poroelasticity, the ratio between the two equilibrium thickness changes, as given in Eqs. (2.39) and (2.49), depends only on Poisson's ratio.

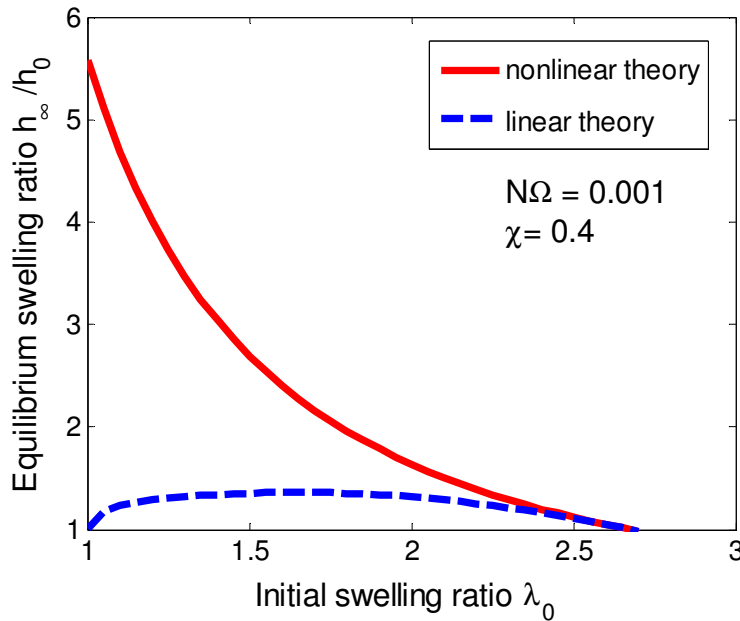


Figure 2.7: Comparison of the equilibrium swelling ratio for a constrained hydrogel layer ($N\Omega = 0.001$ and $\chi = 0.4$), as predicted by the nonlinear theory and the linear poroelasticity.

However, as shown in Fig. 2.7, the linear poroelasticity theory underestimates the equilibrium swelling ratio in comparison with the nonlinear theory, especially for the cases with relatively large swelling ratios ($h_\infty/h_0 > 1.05$). By the nonlinear theory, the equilibrium swelling ratios, which can be determined from (2.33) and (2.45) respectively for the constrained and free swelling, depend on the intrinsic properties of the gel (χ and $N\Omega$) as well as the initial swelling ratio (λ_0). The ratio between the two equilibrium thickness changes, $\Delta_\infty^c / \Delta_\infty^f$, is plotted in Fig. 2.8 as a function of λ_0 for $N\Omega = 0.001$ and different values of χ . The predictions by the linear and the nonlinear theory agree only when the initial swelling ratio is close to the equilibrium free swelling ratio ($\lambda_0 \sim \lambda_\infty^f$). With the measured ratio $\Delta_\infty^c / \Delta_\infty^f = 2$, we cannot determine the three parameters (λ_0, χ and $N\Omega$) in the nonlinear theory.

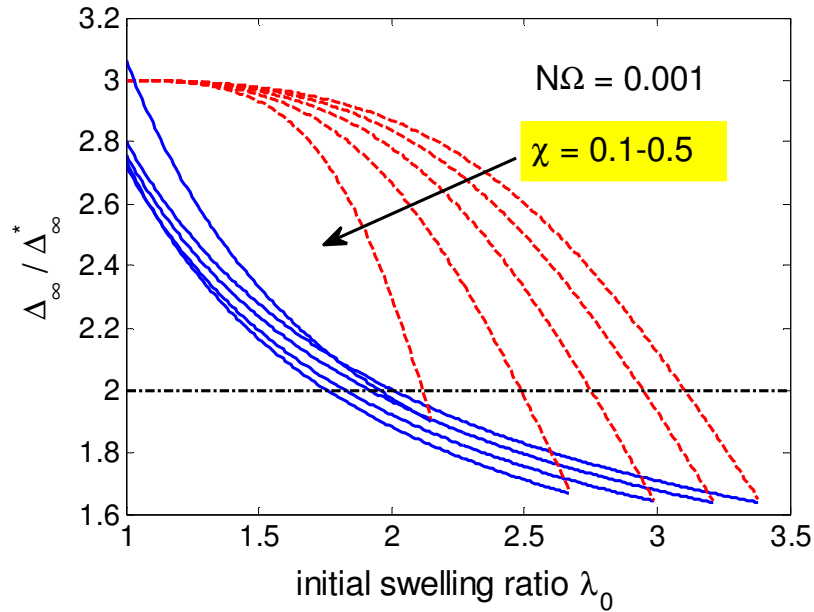


Figure 2.8: The ratio between the equilibrium thickness changes for constrained and free swelling, predicted by the nonlinear theory as a function of the initial swelling ratio for $N\Omega = 0.001$ and $\chi = 0.1-0.5$, in comparison with the prediction by the linear poroelasticity theory (dashed lines).

Next, the effective diffusivity (D^*) in the linear poroelasticity theory was determined by fitting the self-similar solution in (4.10) to the data for constrained swelling at the early stage (Yoon et al., 2010). This is plausible since the linear theory is expected to be applicable at the early stage of swelling. With the self-similar kinetics at the early stage and the measured equilibrium thickness ratio ($\Delta_\infty^c / h_0 = 0.80$), the kinetics of constrained swelling was well described by the linear theory, despite the relatively large degree of swelling. With the same set of linear poroelastic parameters (ν , D^* , and Δ_∞^c / h_0), the kinetics of free swelling as predicted by the linear theory was also found to be in good agreement with the experiment. However, it is cautioned that the results should be interpreted within the fundamental limit of linear poroelasticity.

Here we suggest an alternative procedure to fit the experimental data using the nonlinear theory. To fully describe the swelling kinetics for both constrained and freestanding hydrogel layers, four parameters are to be determined: λ_0 , χ , $N\Omega$, and D . In addition to the measurement of swelling kinetics, Yoon et al., (2010) performed independent measurements of the shear modulus of the same gel by shear rheology. In principle, by measuring the shear modulus of the gel in the unswelled state (just after polymerization) and in the equilibrium state after free swelling, we obtain by (3.8): $G_0 = Nk_B T / \lambda_0$ and $G_\infty = Nk_B T / \lambda_\infty^f$. The measured values for the PNIPAM gel were: $G_0 = 1.3$ kPa and $G_\infty = 0.5$ kPa.¹¹ However, the ratio between the two moduli, $G_0 / G_\infty = 2.6$, does not agree with the ratio, $\lambda_\infty^f / \lambda_0 = 1.4$, as measured from the free swelling experiment (Yoon et al., 2010). The discrepancy raises questions regarding the nonlinear theory as well as experimental uncertainties. Nevertheless, to illustrate the procedure of data fitting, we take one of the measured shear modulus (e.g., $G_0 = 1.3$ kPa) and disregard the other. The three parameters, λ_0 , χ and $N\Omega$, can then be

determined from the three measurable quantities, G_0 , $R_c = h_\infty^c / h_0$, and $R_f = h_\infty^f / h_0$, by solving the following three equations simultaneously:

$$\frac{N\Omega}{\lambda_0} = \frac{\Omega G_0}{k_B T} \quad (2.52)$$

$$\ln\left(1 - \frac{1}{R_c \lambda_0^3}\right) + \frac{1}{R_c \lambda_0^3} + \frac{\chi}{R_c^2 \lambda_0^6} + N\Omega\left(\frac{R_c}{\lambda_0} - \frac{1}{R_c \lambda_0^3}\right) = 0 \quad (2.53)$$

$$\ln\left(1 - \frac{1}{R_f \lambda_0^3}\right) + \frac{1}{R_f \lambda_0^3} + \frac{\chi}{R_f^6 \lambda_0^6} + N\Omega\left(\frac{1}{R_f \lambda_0} - \frac{1}{R_f \lambda_0^3}\right) = 0 \quad (2.54)$$

Using the measured values from Yoon et al., (2010), $G_0 = 1.3$ kPa, $R_c = 1.8$ and $R_f = 1.4$, along with $\Omega = 10^{-28}$ m³ and $T = 298$ K, we obtain $\lambda_0 = 2.474$, $\chi = 0.4724$, and $N\Omega = 7.821 \times 10^{-5}$. The corresponding Poisson's ratio at the initial state is $\nu = 0.47$ by definition in (2.22). Using the same parameters, the Poisson's ratio at the fully swollen state is $\nu = 0.27$, which compares closely with reported values for PNIPAM gels from various measurements (Hiros, 1991; Li et al., 1993). As noted in Fig. 2.5a, Poisson's ratio may change considerably from the initial state to the equilibrium state.

To determine the diffusivity (D), we compare the self-similar solution in (2.37) with the data for constrained swelling at the early stage. Using the effective diffusivity $D^* = 1.5 \times 10^{-11}$ m²s⁻¹ obtained by Yoon et al. (2010), we obtain that

$$D = \frac{D^*}{\xi(\lambda_0^*)} = 1.098 \times 10^{-7} \text{ m}^2 \text{ s}^{-1} \quad (2.55)$$

Here $\lambda_0^* = 1/2(\lambda_0 + \lambda_\infty^c) = 3.464$ has been used to account for instantaneous swelling near the surface as discussed in Section 2.3. On the other hand, by (2.30) and (2.25), the diffusivity can also be obtained as

$$D = D^* \frac{(1-2\nu)k_B T}{2(1-\nu)\Omega G_0} \frac{\lambda_0^3}{\lambda_0^3 - 1} = 2.74 \times 10^{-8} \text{ m}^2 \text{ s}^{-1} \quad (2.56)$$

which however underestimates the swelling rate. Since the surface of the hydrogel layer swells instantaneously to a large degree ($\lambda_\infty^c / \lambda_0 = 1.8$), the linear theory with all properties defined at the initial state cannot correctly predict the swelling kinetics near the surface even at the early stage.

With all the parameters determined from (2.52)-(2.56), Fig. 2.9 compares the swelling kinetics by the nonlinear theory with the linear theory. Using the parameters determined by Yoon et al. (2010) the linear theory agrees closely with the experimental data. Thus, Fig. 2.9 can be considered as a comparison between the nonlinear theory and the experiment. As expected from the data fitting procedure, the nonlinear theory reproduces the two equilibrium swelling ratios and the kinetics of constrained swelling at the early stage. The kinetics of free swelling at the early stage, not used for data fitting, is correctly predicted by the nonlinear theory. In Fig. 2.9, two curves are plotted for free swelling according to the nonlinear theory, one for the average thickness ratio ($\Delta h / h_0$) and the other for in-plane swelling ratio ($\lambda_1 / \lambda_0 - 1$). The two curves are slightly different at the early stage of swelling as shown more clearly in Fig. 2.4b. The curve for in-plane swelling ratio agrees more closely with the experimental data, which was actually obtained by measuring the in-plane swelling instead of the thickness ratio (Yoon et al., 2010). However, relatively large discrepancy is notable beyond the early stage, although it is comparable to the scattering of the experimental data.

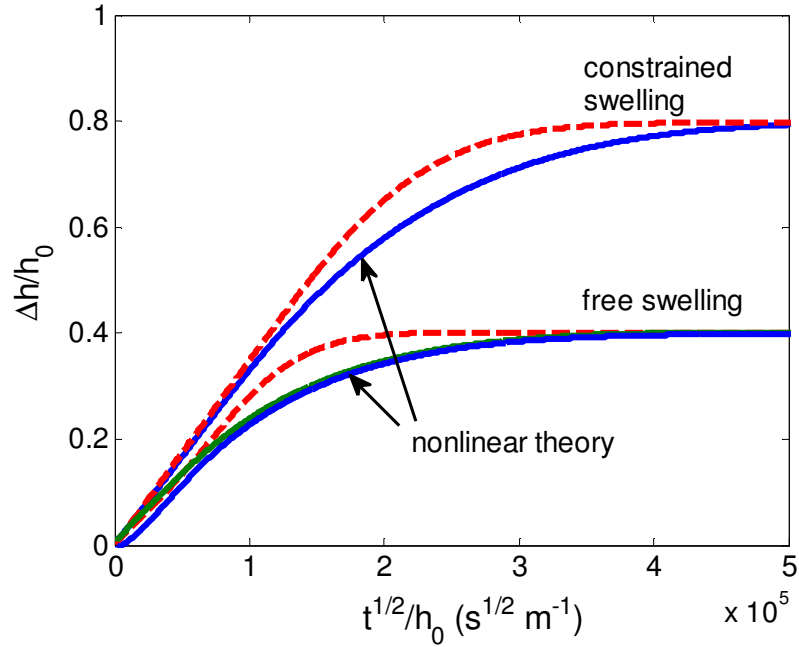


Figure 2.9: A comparison between the nonlinear theory and experimental results for kinetics of constrained and free swelling. The dashed lines reproduce the predictions of linear poroelasticity using the parameters determined by Yoon et al.⁽²⁰¹⁰⁾ to fit their experimental data. The solid lines are numerical results based on the nonlinear theory using the parameters determined from (5.3)-(5.6): $\lambda_0 = 2.474$, $\chi = 0.4724$, $N\Omega = 7.821 \times 10^{-5}$, and $D = 1.098 \times 10^{-7} \text{ m}^2 \text{ s}^{-1}$.

2.4.4. On indentation method

Indentation experiments have been demonstrated recently as an effective method for characterizing poroelastic properties of gels (Hui et al., 2006; Yoon et al., 2010; Hu et al., 2010, 2011 & 2012). By imposing relatively shallow indentation displacements into a saturated gel and measuring force relaxation as a function of time, the linear poroelastic properties can be fully determined without ambiguity. Such a method is efficient from both experimental and theoretical points of view. The procedure of the indentation

experiment is relatively simple, and the analysis of the data is fairly straightforward within the theoretical framework of linear poroelasticity due to relatively small deformation. As shown by Hu et al. [2011] the measured elastic constants (G and ν) can be interpreted within the Flory-Huggins theory for nonlinear analysis. Since the gel is fully saturated with the solvent, the swelling ratio λ_0 is determined by the intrinsic properties (χ and $N\Omega$) of the gel as given in Eq. (2.14) with $\mu_0 = 0$. Thus the measured elastic constants by the indentation method are the linear properties at the vicinity of the fully swollen state of the gel. Furthermore, the effective diffusivity (D^*) measured by the indentation method can be converted to the intrinsic diffusivity D in the nonlinear theory, as given in (2.56). Therefore, all the intrinsic properties in the nonlinear theory can be determined from the indentation method, which would then enable prediction of the nonlinear behavior of the gel with large deformation. In particular, a comparison between a full nonlinear analysis of the force relaxation during indentation and the linear poroelasticity solution would be useful to quantitatively define the shallow indentation requirement for the linear analysis.

As noted by Hui et al. (2006), it is possible to extend the analysis of the indentation experiment to include the effect of adhesion. Polymer gels are often sensitive to adhesive interactions with other materials coming into contact. Contact mechanics with the effect of adhesion has been developed and widely used to characterize adhesive interactions between surfaces (Johnson et al., 1971; Chaudhury et al., 1991). However, most studies have assumed elastic behavior of the interacting solids, and extension to poroelastic solids would be desirable for the study of adhesion between polymer gels. In addition, many applications use gels in the form of thin layers (Hu et al., 2011). Constrained swelling of thin layers results in an anisotropic swollen state (Kang and Huang, 2010a). Indentation upon such a gel layer should be analyzed using an anisotropic

poroelasticity theory. The linearization procedure in Section 2.2 of the present work can be easily extended to develop a set of linear equations for anisotropic poroelasticity consistent with the nonlinear theory. Then the anisotropic poroelastic contact problem may be solved by extending the solution to the corresponding elastic contact problem for anisotropic materials (Willis, 1966; Vlassak et al., 2005). Further extension of the indentation method may be developed to characterize polymer gels in the form of patterned lines and particles (Tirumala et al., 2005; DuPont et al., 2010; Kang and Huang, 2011; Caldorera et al., 2011). The analysis would be necessarily complicated due to the geometry and likely inhomogeneous swelling. Numerical analysis based on the nonlinear theory would be required along with experimental measurements, which may be used to probe the effects of size and shape on the mechanical and transport properties of polymer gels.

2.5. SUMMARY

In summary, we present a comparison between a nonlinear theory for polymer gels and the classical theory of linear poroelasticity. We show that the two theories are consistent within the linear regime under the condition of small perturbation from an isotropically swollen state of the gel. The relationship between the material properties in the linear theory and those in the nonlinear theory is established by a linearization procedure. Both linear and nonlinear solutions are presented for swelling kinetics of substrate-constrained and freestanding hydrogel layers. Although the linear poroelasticity theory can be used to fit the experimental data, it is cautioned that the applicability of the linear theory should be limited to relatively small swelling ratios. For large swelling ratios, a new procedure is suggested to fit the experimental data with the nonlinear

theory. Finally, we discussed the indentation experiment as an effective method for characterizing the mechanical and transport properties of polymer gels along with possible extensions of the method.

Chapter 3

A Nonlinear Transient Finite Element Method

The aim of this chapter is to develop a transient finite element method for large deformation of hydrogels based on a nonlinear continuum theory. A constitutive theory with material laws specified for the cases of hydrogels with compressible constituents and incompressible constituents will be defined, and the discretization and solution procedures of the finite element method will be modified accordingly for each case.

3.1. FINITE ELEMENT PRELIMINARIES FOR POROELASTIC PROBLEMS

Starting from a critical point for the formulation of a transient mixed finite element method for hydrogels, as noted by Wang and Hong (2012a), when implementing the finite element method for the transient response of hydrogels, a mixed formulation must be used with different shape functions for discretization of the displacement and chemical potential in a hydrogel. In fact, such a requirement has been known for finite element methods in linear poroelasticity, which have been studied primarily in the context of geomechanics. The most common method used in the studies of linear poroelasticity is the mixed continuous Galerkin formulation for displacement and pore pressure (Borja, 1986; Wan, 2002; White and Borja, 2008). For either poroelasticity or hydrogels, the transient response can often be decomposed into three stages: the instantaneous response at $t \rightarrow 0$, the transient evolution, and the equilibrium or steady state as $t \rightarrow \infty$. At the instantaneous limit, the poroelastic response is similar to the linear elastic response of an incompressible or nearly incompressible solid, which requires the mixed finite element method to satisfy the Ladyzhenskaya-Babuska-Brezzi (LBB) condition (Murad and Loula, 1994; Wan, 2002). First noted by Babuška (1971) and Brezzi (1974), the LBB condition requires that the finite element discretization for

incompressible linear elasticity and Stokes flow satisfy the incompressibility constraints in order to produce stable results. An example is provided by the elements in the Taylor-Hood family (Taylor and Hood, 1973) where the spatial discretization for pressure is one order lower than for displacement (Figure 3.1). If the LBB condition is not satisfied, numerical oscillations in the form of spurious pressure modes would be obtained for the instantaneous response of a nearly incompressible poroelastic medium. As discussed in Murad and Loula (1992), Wan (2002), and Phillips (2005), the numerical oscillations are prevalent in the early stage of transient responses, which would decay in time and eventually converge towards the equilibrium or steady state. In the present study, we show that the implementation of a transient finite element method for hydrogels with coupled diffusion and large deformation should also satisfy the LBB condition to avoid numerical instabilities.

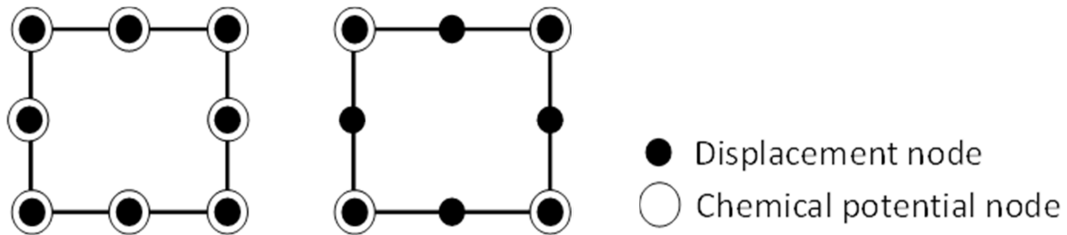


Figure 3.1: Two types of quadrilateral elements: an equal-order eight-node element (8u8p) and a Taylor-Hood element (8u4p).

Most of the previous works on transient finite element methods for hydrogels (Zhang et al., 2009; Wang and Hong, 2012a; Lucantonio et al., 2013; Toh et al., 2013) have assumed incompressibility for both the polymer network and the solvent, which imposes a volume constraint on the hydrogel with a relationship between solvent concentration and deformation. In Section 3.2, we summarize the nonlinear continuum theory proposed by Hong et al. (2008) and relax the volume constraint by introducing a bulk modulus as an additional material property. Section 3.3 presents the finite element formulation and implementation of a mixed finite element method using the backward Euler scheme for time integration and the Newton-Raphson method for solving the nonlinear problem iteratively. Section 3.4 summarizes the exactly incompressible nonlinear continuum theory, and in Section 3.5 the mixed finite element method is modified to adopt the changes in the constitutive model. Section 3.6 summarizes critical features of the proposed numerical methods.

3.2. A NONLINEAR THEORY-COMPRESSIBLE FORMULATION

Following Hong et al. (2008a), the constitutive behavior of a polymer gel is described through a free energy density function based on the Flory-Rehner theory, following equations (2.1-3).

In previous works (e.g., Hong et al., 2008; Zhang et al., 2009), both the polymer and the solvent were assumed to be incompressible. As a result, the volumetric strain of the hydrogel is solely related to the solvent concentration, which imposes a constraint on the deformation gradient. Such a constraint is lifted in the present study to allow compressibility by adding a quadratic term into the elastic free energy from Eq. (2.2), namely

$$U_e(\mathbf{F}, C) = \frac{1}{2} Nk_B T \left[F_{iK} F_{iK} - 3 - 2 \ln(\det(\mathbf{F})) \right] + \frac{K}{2} (\det(\mathbf{F}) - 1 - \Omega C)^2 \quad (3.1)$$

where K is a bulk modulus with the same unit as $Nk_B T$ (shear modulus). It is expected that the behavior of the hydrogel predicted by the modified free energy function approaches that by the original theory when the bulk modulus is sufficiently large (i.e., $K \gg Nk_B T$). Note that the elastic free energy in (3.1) introduces a coupling between deformation gradient and solvent concentration at the constitutive level.

The nominal stress and chemical potential of the solvent in the hydrogel are obtained from the free energy density function as

$$s_{ij} = \frac{\partial U}{\partial F_{ij}} = Nk_B T (F_{ij} + \alpha H_{ij}). \quad (3.2)$$

$$\mu = \frac{\partial U}{\partial C} = k_B T \left(\ln \frac{\Omega C}{1 + \Omega C} + \frac{(1 + \Omega C) + \chi}{(1 + \Omega C)^2} \right) - \Omega K (\det(\mathbf{F}) - 1 - \Omega C). \quad (3.3)$$

where

$$\alpha = -\frac{1}{\det(\mathbf{F})} + \frac{K}{Nk_B T} (\det(\mathbf{F}) - 1 - \Omega C) \quad (3.4)$$

$$H_{ij} = \frac{1}{2} e_{ijk} e_{JKL} F_{jK} F_{kL}. \quad (3.5)$$

Mechanical equilibrium is assumed to be maintained at all time during the transient process, which requires that

$$\frac{\partial s_{ij}}{\partial X_j} + b_i = 0 \text{ in } V_0 \quad (3.6)$$

$$s_{ij} N_j = T_i \text{ on } S_0 \quad (3.7)$$

where b_i is the nominal body force (per unit volume), V_0 is the volume in the reference configuration, N_j is unit normal on the surface of the reference configuration, and T_i is the nominal traction on the surface. In addition, prescribed displacements can be specified as essential boundary conditions.

On the other hand, the gel has not reached chemical equilibrium in the transient stage. The gradient of chemical potential drives solvent migration inside the gel. By a diffusion model (Hong et al., 2008), the true flux of the solvent was presented in Chapter 2 in Eq. (2.9). and also the nominal flux and the nominal mobility tensor were defined in Eqs. (2.10-11).

By mass conservation, a rate equation for change of the local solvent concentration is obtained as

$$\frac{\partial C}{\partial t} + \frac{\partial J_{\kappa}}{\partial X_{\kappa}} = r \text{ in } V_0 \quad (3.8)$$

where r is a source term for the number of solvent molecules injected into unit reference volume per unit time. The chemical boundary condition for the gel in general can be a mixture of two kinds, i.e., $S_0 = S_i + S_{\mu}$, where the solvent flux is specified on S_i and the chemical potential is specified on S_{μ} .

3.3. FINITE ELEMENT METHOD– COMPRESSIBLE FORMULATION

This section presents a finite element formulation based on the nonlinear theory in Section 3.2, starting from the strong form of the governing equations and initial/boundary conditions, to the weak form of the problem, and then to the discretization and solution procedures.

As the strong form of the initial/boundary-value problem, the governing field equations in (3.6) and (3.8) are complemented by a set of initial and boundary conditions. The initial conditions are typically described by a displacement field ($\mathbf{u} = \mathbf{x} - \mathbf{X}$) and chemical potential:

$$\mathbf{u}|_{t=0} = \mathbf{u}_0 \quad (3.9)$$

$$\mu|_{t=0} = \mu_0 \quad (3.10)$$

Relative to the dry state ($\mu \rightarrow -\infty$), the initial displacement field can be prescribed for a homogeneous deformation corresponding to a constant chemical potential (e.g., $\mu_0 = 0$).

At $t = 0^+$, boundary conditions are applied. The mechanical boundary condition can be prescribed with a mixture of traction and displacement:

$$s_{ij}N_j = T_i \text{ or } u_i = \bar{u}_i \text{ on } S_0 \quad (3.11)$$

Similarly, the chemical boundary condition is prescribed as

$$J_k N_k = -i \text{ or } \mu = \bar{\mu} \text{ on } S_0 \quad (3.12)$$

where i is the surface flux rate (number of solvent molecules per unit reference area per unit time, positive inward) and $\bar{\mu}$ is the surface chemical potential depending on the surrounding environment.

Since the chemical boundary conditions for gels are often specified in terms of chemical potential or diffusion flux (proportional to the gradient of chemical potential), it is convenient to use the chemical potential (instead of solvent concentration) as an independent variable in the finite element formulation. For this purpose, we re-write the free energy density as a function of the deformation gradient and chemical potential by Legendre transform:

$$\hat{U}(\mathbf{F}, \mu) = U(\mathbf{F}, C) - \mu C \quad (3.13)$$

Similar to Eqs. (3.2) and (3.3), we have

$$s_{ij}(\mathbf{F}, \mu) = \frac{\partial \hat{U}}{\partial F_{ij}} \quad (3.14)$$

$$C(\mathbf{F}, \mu) = -\frac{\partial \hat{U}}{\partial \mu} \quad (3.15)$$

which yield the same constitutive relationships but the solvent concentration is now given implicitly by solving a nonlinear algebraic equation in (3.3). We also note that the continuity requirement for the nonlinear finite element formulation remains C_0 by using the chemical potential instead of the concentration as a nodal degree of freedom

3.3.1. Weak form

The solution to the initial/boundary-value problem consists of a vector field of displacement and a scalar field of chemical potential, $\mathbf{u}(\mathbf{X}, t)$ and $\mu(\mathbf{X}, t)$, which are coupled and evolve concurrently with time. The weak form of the problem is obtained by using a pair of test functions, $\delta \mathbf{u}(\mathbf{X})$ and $\delta \mu(\mathbf{X})$, which satisfy necessary integrability conditions. Multiplying Eq. (3.6) by δu_i , integrating over V_0 , and applying the divergence theorem, we obtain that

$$\int_{V_0} s_{ij} \delta u_{i,j} dV = \int_{V_0} b_i \delta u_i dV + \int_{S_0} T_i \delta u_i dS \quad (3.16)$$

Similarly, multiplying Eq. (3.8) by $\delta \mu$ and applying the divergence theorem for the volume integral, we obtain that

$$\int_{V_0} \frac{\partial C}{\partial t} \delta \mu dV - \int_{V_0} J_{\kappa} \delta \mu_{,\kappa} dV = \int_{V_0} r \delta \mu dV + \int_{S_0} i \delta \mu dS \quad (3.17)$$

Hence, the weak form of the problem statement is to find $\mathbf{u}(\mathbf{X}, t)$ and $\mu(\mathbf{X}, t)$ such that the integral equations (3.16) and (3.17) are satisfied for any permissible test functions, $\{\delta \mathbf{u}, \delta \mu\}$.

3.3.2. Time integration

A backward Euler scheme is used to integrate Eq. (3.17) over time:

$$\int_{V_0} \frac{C^{t+\Delta t} - C^t}{\Delta t} \delta\mu dV - \int_{V_0} J_K^{t+\Delta t} \delta\mu_{,K} dV = \int_{V_0} r^{t+\Delta t} \delta\mu dV + \int_{S_0} i^{t+\Delta t} \delta\mu dS \quad (3.18)$$

where the superscripts indicate quantities at the current time step ($t + \Delta t$) or the previous step (t). The implicit backward Euler integration scheme is first order accurate and allows for improved numerical stability compared to the explicit forward Euler integration.

Combine Eq. (3.18) with Eq. (3.16) and rearrange to obtain

$$\begin{aligned} & \int_{V_0} (s_{iJ} \delta u_{i,J} - C \delta\mu + \Delta t J_K \delta\mu_{,K}) dV = \\ & \int_{V_0} (b_i \delta u_i - r \Delta t \delta\mu - C^t \delta\mu) dV + \int_{S_0} T_i \delta u_i dS - \int_{S_0} i \Delta t \delta\mu dS \end{aligned} \quad (3.19)$$

where the superscript ($t + \Delta t$) is omitted for all the terms at the current time step and C^t is the solvent concentration at the previous time step.

3.3.3. Spatial discretization

Next the displacement and chemical potential are discretized through interpolation in the domain of interest:

$$\mathbf{u} = \mathbf{N}^u \mathbf{u}^n \quad \text{and} \quad \mu = \mathbf{N}^\mu \boldsymbol{\mu}^n \quad (3.20)$$

where \mathbf{N}^u and \mathbf{N}^μ are shape functions, \mathbf{u}^n and $\boldsymbol{\mu}^n$ are the nodal values of the displacement and chemical potential, respectively. The test functions are discretized in the same way

$$\delta\mathbf{u} = \mathbf{N}^u \delta\mathbf{u}^n \quad \text{and} \quad \delta\mu = \mathbf{N}^\mu \delta\boldsymbol{\mu}^n \quad (3.21)$$

The stress, solvent concentration, and flux are evaluated at integration points, depending on the gradients of the displacement and chemical potential via the constitutive relations. Taking the gradient of Eq. (3.20), we obtain that

$$\nabla \mathbf{u} = \mathbf{F} - \mathbf{I} = \nabla \mathbf{N}^u \mathbf{u}^n = \mathbf{B}^u \mathbf{u}^n \quad (3.22a)$$

$$\nabla \mu = \nabla \mathbf{N}^\mu \boldsymbol{\mu}^n = \mathbf{B}^\mu \boldsymbol{\mu}^n \quad (3.22b)$$

where \mathbf{B}^u and \mathbf{B}^μ are gradients of the shape functions. In this formulation we have allowed the use of different shape functions to interpolate displacement and chemical potential.

Before proceeding to choose a type of interpolation for displacement and chemical potential, it is important to consider the nearly incompressible behavior of a hydrogel at the instantaneous limit ($t \rightarrow 0$). In linear elasticity, at the incompressible limit, a finite element method with displacement as the only unknown would fail to converge to the true solution. Thus a mixed finite element method with both displacement and pressure as the unknown fields must be employed (Hughes, 1987). In order for the mixed method to produce numerically stable results, the LBB condition must be satisfied (Babuška, 1971; Brezzi, 1974). This is ensured by the appropriate choice of shape functions for interpolation of the displacement and pressure. Elements with shape functions of equal order do not satisfy the LBB condition and hence produce numerical oscillations. A family of elements that satisfy the LBB condition are the Taylor-Hood elements (Taylor and Hood, 1987), where interpolation for pressure is one order lower than for displacement. However, the combination of zero-order constant pressure and first-order linear displacement results in spurious pressure modes (Sussman and Bathe, 1987). Thus, the lowest order Taylor-Hood element that produces stable results combines

first-order linear interpolation for pressure and second-order quadratic interpolation for displacement.

Similar numerical issues have been noted in linear poroelasticity when the instantaneous response is nearly incompressible. Vermeer and Verruijt [1981] first proposed a stability condition for the poroelastic consolidation problem, where the time step had to be larger than a proposed value. It was established later that this numerical instability was due to the use of unstable elements in the LBB sense (Zienkiewicz et al., 1990). Extensive discussions about the numerical issues for solving Biot's consolidation problem with mixed finite element methods have been presented by Murad and Loula (1992 and 1994), Wan (2002), and Phillips (2005). In the case of a poroelastic medium with incompressible or nearly incompressible constituents, numerically oscillating solutions for the pore pressure field are obtained at the initial stages of the evolution process when the shape functions for the displacement and pore pressure do not satisfy the LBB condition. As the equations turn from elliptic to parabolic in the transient stage, the diffusion process is known to regularize the oscillating solution and the oscillations would eventually vanish after a sufficiently long time.

In Chapter 2, it has been shown that the nonlinear continuum theory proposed by Hong et al. (2008) reduces to Biot's linear poroelasticity theory for small deformation of an isotropically swollen gel (Bouklas and Huang, 2012). Thus, similar numerical issues are to be expected for the finite element method in the present formulation when $K \gg Nk_B T$. In the continuum theory for hydrogels, chemical potential plays the role of pore pressure in linear poroelasticity. To satisfy the LBB condition, the shape function for chemical potential must be one order lower than for the displacement in the mixed finite element method. Otherwise, numerical oscillations would be significant and instantaneous response of the hydrogel may not be correctly predicted, (as shown in

Chapter 4). The necessity to employ a stable combination of the shape functions was first noted by Wang and Hong (2012a) in their study on visco-poroelastic behaviors of polymer gels.

In the present study, we have implemented the Taylor-Hood elements with quadratic shape functions for the displacement and linear shape functions for the chemical potential. For comparison, equal-order elements with quadratic shape functions for both displacement and chemical potential are also implemented. Regardless of the choice of shape functions, the same steps are followed to calculate the nominal stress (\mathbf{s}), nominal concentration (C) and flux (\mathbf{J}) at the integration points, to numerically integrate the weak form over each element, and then to assemble globally to form a system of nonlinear equations. In particular, the nominal concentration C is first calculated at each integration point by solving Eq. (3.3) with the interpolated chemical potential and the displacement gradient. A one-dimensional Newton-Raphson method is implemented to solve the nonlinear algebraic equation. Subsequently, the nominal stress is calculated by Eq. (3.2) and the flux is calculated using Eq. (2.10-11).

After the spatial discretization, invoking the arbitrariness of the test functions, the weak form in Eq. (3.19) can be expressed as a system of nonlinear equations,

$$\mathbf{n}(\mathbf{d}) = \mathbf{f} \quad (3.23)$$

where $\mathbf{d} = \begin{bmatrix} \mathbf{u}^n \\ \boldsymbol{\mu}^n \end{bmatrix}$. More specifically, the individual contributions to Eq. (3.23) are

$$\begin{aligned} n_i^{u,M} &= \int_{V_0} s_{ij} B_j^{u,M} dV \\ n^{\mu,M} &= \int_{V_0} (-CN^{\mu,M} + \Delta t J_K B_K^{\mu,M}) dV \end{aligned} \quad (3.24a)$$

$$\begin{aligned} f_i^{u,M} &= \int_{V_0} b_i N^{u,M} dV + \int_{S_0} T_i N^{u,M} dS \\ f^{\mu,M} &= \int_{V_0} (r\Delta t - C^t) N^{\mu,M} dV - \int_{S_0} i\Delta t N^{\mu,M} dS \end{aligned} \quad (3.24b)$$

where the superscript M refers to the node and the subscript in B_J^u refers to the direction in which the derivative is taken.

3.3.4. Newton-Raphson method

The system of nonlinear equations in (3.23) are solved iteratively using the Newton-Raphson method at each time step. Noting that the right hand side of the equations only consists of known quantities, the residual in each iteration can be calculated as

$$\mathbf{R}_i = \mathbf{f} - \mathbf{n}(\mathbf{d}_i) \quad (3.25)$$

where \mathbf{d}_i represents the solution at the i th iteration. The correction to the solution is then calculated as

$$\Delta \mathbf{d}_i = \left[\frac{\partial \mathbf{n}}{\partial \mathbf{d}} \Big|_{\mathbf{d}_i} \right]^{-1} \mathbf{R}_i \quad (3.26)$$

with which the nodal unknowns are updated for the next iteration as $\mathbf{d}_{i+1} = \mathbf{d}_i + \Delta \mathbf{d}_i$. The iteration repeats until a suitable level of convergence is reached, both in terms of the nodal corrections, $\|\Delta \mathbf{d}\| = \sqrt{\sum (\Delta d_j)^2}$, and the residual, $\|\mathbf{R}\| = \sqrt{\sum (R_j)^2}$.

In particular, Eq. (3.26) requires calculation of the tangent Jacobian matrix at each iteration, namely

$$\frac{\partial \mathbf{n}}{\partial \mathbf{d}} \Big|_{\mathbf{d}_i} = \begin{bmatrix} \mathbf{K}^{uu} & \mathbf{K}^{um} \\ \mathbf{K}^{mu} & \mathbf{K}^{mm} \end{bmatrix} \quad (3.27)$$

where for each pair of nodes (N, M) and degrees of freedom (i, k) :

$$K_{ik}^{uu, NM} = \int_{V_0} B_J^{u, N} \frac{\partial^2 \hat{U}}{\partial F_{ij} \partial F_{kl}} B_L^{u, M} dV \quad (3.28a)$$

$$K_i^{\mu\mu, NM} = \int_{V_0} B_J^{\mu, N} \frac{\partial^2 \hat{U}}{\partial F_{iJ} \partial \mu} N^{\mu, M} dV \quad (3.28b)$$

$$K_i^{\mu\mu, NM} = \int_{V_0} \left[N^{\mu, N} \frac{\partial^2 \hat{U}}{\partial \mu \partial F_{iJ}} B_J^{\mu, M} + \Delta t \frac{D}{k_B T} B_K^{\mu, N} \left(\frac{\partial^2 \hat{U}}{\partial \mu \partial F_{iJ}} F_{Kk}^{-1} F_{Ll}^{-1} + \frac{\partial \hat{U}}{\partial \mu} \frac{\partial F_{Kk}^{-1}}{\partial F_{iJ}} F_{Ll}^{-1} + \frac{\partial \hat{U}}{\partial \mu} F_{Kk}^{-1} \frac{\partial F_{Ll}^{-1}}{\partial F_{iJ}} \right) \mu^N B_L^{\mu, N} B_J^{\mu, M} \right] dV \quad (3.28c)$$

$$K_i^{\mu\mu, NM} = \int_{V_0} \left[N^{\mu, N} \frac{\partial^2 \hat{U}}{\partial \mu^2} N^{\mu, M} + \Delta t \frac{D}{k_B T} B_K^{\mu, N} \left(\frac{\partial^2 \hat{U}}{\partial \mu^2} F_{Kk}^{-1} F_{Ll}^{-1} \mu^N B_L^{\mu, N} N^{\mu, M} + \frac{\partial \hat{U}}{\partial \mu} F_{Kk}^{-1} F_{Ll}^{-1} B_L^{\mu, M} \right) \right] dV \quad (3.28d)$$

We notice that the derivatives of the mobility tensor in Eqs. (3.28 c and d) break the symmetry of the tangent matrix. For a consistent Newton-Raphson method, a non-symmetric solver has to be implemented to achieve quadratic convergence of the iterative procedure. Alternatively, a symmetric tangent Jacobian matrix may be used as an approximation with

$$K_i^{\mu\mu, NM} = \int_{V_0} \left(N^{\mu, N} \frac{\partial^2 \hat{U}}{\partial \mu \partial F_{iJ}} B_J^{\mu, M} \right) dV \quad (3.29a)$$

$$K_i^{\mu\mu, NM} = \int_{V_0} \left[N^{\mu, N} \frac{\partial^2 \hat{U}}{\partial \mu^2} N^{\mu, M} + \Delta t \frac{D}{k_B T} B_K^{\mu, N} \frac{\partial \hat{U}}{\partial \mu} F_{Kk}^{-1} F_{Ll}^{-1} B_L^{\mu, M} \right] dV \quad (3.29b)$$

so that the standard symmetric solver can be employed for the ease of computation. However, if the mobility tensor is updated throughout the iterative process, the use of the

inconsistent symmetric tangent matrix would lead to loss of the quadratic convergence, although the scheme remains fully implicit and unconditionally stable. On the other hand, if the mobility tensor is fixed at the previous time step, the tangent matrix would be consistently symmetric and hence the quadratic convergence would be maintained. In this case, however, the time integration is partly explicit with the forward Euler scheme for the mobility tensor. As a result, the time step has to be chosen appropriately to ensure stability. In the present study, both methods with the symmetric tangent matrix have been implemented, and both yield convergent results for the specific problems considered.

3.4.A NONLINEAR THEORY-INCOMPRESSIBLE FORMULATION

In this section, a material model with incompressible constituents, following Chapter 2, will be presented. Incompressibility will be enforced without the use of Lagrange multipliers this time, to allow for a convenient form of the free energy density to be used in the finite element method that will follow.

Following Hong et al. (2008), a free energy density function based on the Flory-Rehner theory is adopted, which can be split into an elastic deformation and a polymer-solvent mixing part defined in Eq. (1-3). Similar to previous works (Hong et al., 2008; Zhang et al., 2009), all the constituents of the hydrogel are considered totally incompressible. This can be ensured by Eq. (2.4) connecting the determinant of the deformation gradient to the volume of the solvent in the hydrogel, where any change to the volume of the hydrogel is due to the concentration of the solvent molecules. Therefore the nominal concentration can be obtained explicitly as a function solely of the deformation gradient through Eq. (2.4). Enforcing the incompressibility constraint of Eq. (2.4) into Eq. (2.1-3), the Legendre transform of the free energy through Eq. (3.13) leads to

$$\begin{aligned} \hat{U}(\mathbf{F}, \mu) = & \frac{1}{2} N k_B T [F_{iK} F_{iK} - 3 - 2 \ln(\det(\mathbf{F}))] + \\ & + \frac{k_B T}{\Omega} \left[(\det(\mathbf{F}) - 1) \ln \frac{(\det(\mathbf{F}) - 1)}{\det(\mathbf{F})} + \frac{\chi(\det(\mathbf{F}) - 1)}{\det(\mathbf{F})} \right] - \frac{\mu(\det(\mathbf{F}) - 1)}{\Omega} \end{aligned} \quad (3.30)$$

The field equations necessary for this formulation are

$$s_{ij} = \frac{\partial \hat{U}}{\partial F_{ij}} = N k_B T (F_{ij} + \alpha H_{ij}) \quad (3.6/3.31)$$

$$C = - \frac{\partial \hat{U}}{\partial \mu} \quad (3.7/3.32)$$

where

$$\alpha = - \frac{1}{\det(\mathbf{F})} - \frac{1}{N \Omega} \left[\ln \left(\frac{\det(\mathbf{F}) - 1}{\det(\mathbf{F})} \right) + \frac{1}{\det(\mathbf{F})} + \frac{\chi}{(\det(\mathbf{F}))^2} \right] + \frac{\mu}{N \Omega k_B T} \quad (3.8/3.33)$$

$$H_{ij} = \frac{1}{2} e_{ijk} e_{JKL} F_{jK} F_{kL} \cdot \quad (3.9/3.34)$$

and Eq. (3.32) just repeats the relationship of the constraint in Eq. (2.4). A relationship for nominal stress is also obtained through Eq. (3.31) and Eq. (3.33-34). The last term of the free energy density is the one that couples the chemical potential with the deformation gradient through the incompressibility constraint.

Along with mechanical equilibrium from Eq. (3.6) and the mass conservation equation from Eq. (3.8) a kinetic law has to be assumed for the hydrogel as chemical equilibrium is not maintained during the transient state. The same diffusion model adopted for hydrogels by Hong et al. (2008) is used again from Eqs. (2.9-11).

3.5.FINITE ELEMENT METHOD-INCOMPRESSIBLE FORMULATION

The strong form of the problem including remains consistent with the formulation in section 3.3. The governing equations (3.6), (3.8) have initial conditions defined in equation (3.9-10) and boundary conditions in (3.11-12). In section 3.4 the Legendre transform of the free energy density was explicitly obtained in Eq. (3.30) for the material model with incompressible constituents. Thus it can be used directly into the formulation of the finite element method presented in Section 3.3 avoiding the complication of not having an explicit expression for the energy form.

The unknowns in the strong form are again a vector field of displacement and a scalar field of chemical potential, $\mathbf{u}(\mathbf{X}, t)$. A pair of test functions, $\delta\mathbf{u}(\mathbf{X})$ and $\delta\mu(\mathbf{X})$, which satisfy necessary integrability conditions are used, and the weak form of the problem following Section 3.3.1 is obtained and expressed in Eqs. (3.16-17). With time integration procedure discussed in Section 3.3.2 using the backward Euler integration scheme, Eq. (3.17) is discretized in time and combined with Eq. (3.16) into Eq. (3.19).

Following, displacement and chemical potential, and their corresponding test functions are discretized in Eqs. (3.20-21). The calculation of stress and flux at the integration points involves, gradients of displacements and chemical potential which are calculated using Eqs. (3.22). The use of different shape functions to interpolate displacement and chemical potential is also allowed in this formulation. As discussed previously, using the incompressible formulation, is expected to pose an issue to the numerical stability of the solution, following the LBB condition. Thus Taylor-Hood will be used in this case as well.

To summarize, for known nodal values of the displacement and the chemical potential, their values are interpolated at the integration points and their gradients are

calculated at the same locations. Following, the nominal stress (\mathbf{s}), nominal concentration (C) and flux (\mathbf{J}) are calculated at the integration points using equations (3.31-34) and (2.10-11), to numerically integrate the weak form over each element, and then to assemble globally to form a system of nonlinear equations.

After the spatial discretization, invoking the arbitrariness of the test functions, the weak form in Eq. (3.23) can be expressed as a system of nonlinear equations assembled following Section 3.3.4 and solved using the Newton-Raphson iterative procedure outlined in Section 3.3.5. The only difference in Eq. (3.28-29) is that in this case, the derivatives of the Legendre transform of the free energy density with respect to the deformation gradient and chemical potential can be directly calculated from Eq. (3.30). Again, a symmetric form of the tangent matrix is implemented in this case.

3.6. SUMMARY

A nonlinear, transient finite element formulation is presented for initial boundary value problems associated with swelling and deformation of hydrogels, based on a nonlinear continuum theory. The cases, and corresponding theories for a hydrogel with incompressible and compressible constituents are considered. Unlike the previous studies, a finite bulk modulus is introduced in the constitutive model for the compressible case. A mixed finite element method is implemented, with specific attention to the numerical stability issues associated with the LBB condition for spatial discretization. Numerical results that demonstrate the capability of the proposed finite element methods for simulating the transient behavior of hydrogels under various initial/boundary conditions are presented in Chapters 4-6, and an in-depth discussion of the numerical issues associated with the proposed finite element method takes place in Chapter 4.

Chapter 4

Simulation of Hydrogel Swelling

Hydrogel swelling is a transient phenomenon that depending on the material parameters, initial state of the hydrogel, and boundary conditions can involve inhomogeneous behavior. The finite element method proposed in Chapter 3 can simulate such behaviors and the scope of this chapter is to first confirm that the method works accurately comparing to some benchmark problems. In Section 4.1 the finite element model for the problem of constrained hydrogel swelling will be described. The numerical stability issues, associated with the mixed finite element method will be discussed with respect to these benchmark problems in Section 4.2 and following, a convergence study will be presented in Section 4.3. Swelling problems involving instability of single layers and bilayers will be examined in Section 4.4. The constitutive model and finite element method for a hydrogel with compressible constituents, presented in Sections 3.2-3 will be used in this chapter. Section 4.5 will summarize the results of this chapter.

4.1 FINITE ELEMENT MODEL

As the first example, we consider constrained swelling of a hydrogel layer attached to a rigid substrate (Fig. 4.1). The same problem has been studied previously by both linear and nonlinear theories in Chapter 2 (Bouklas and Huang, 2012), which provides a benchmark for the finite element method developed in this study. A two-dimensional finite element (2D-FE) model is used to simulate swelling of the hydrogel layer. As shown in Fig. 4.1, three types of boundary conditions are imposed onto the simulation box: the surface (S1) is traction free and in contact with an external solvent so

that $\mu|_{x_2=H} = 0$; the bottom (S2) is attached to the substrate so that $\Delta u|_{x_2=0} = 0$ (fixed displacement, $\Delta u = u - u_0$) and $J_2|_{x_2=0} = 0$ (zero flux); the two sides (S3) are subject to

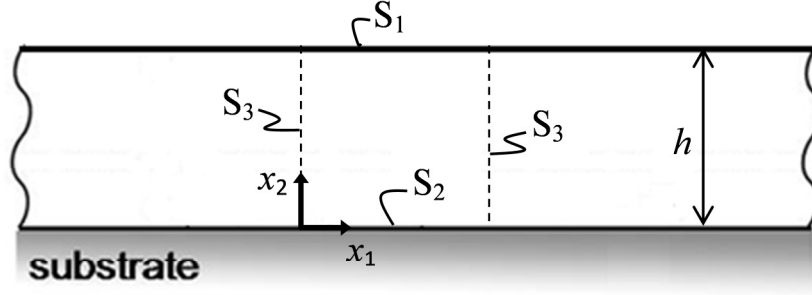


Figure 4.1: Schematic of a hydrogel layer attached to a rigid substrate. Three types of boundary conditions (S1, S2, and S3) are indicated for the finite element analysis.

the symmetry conditions with $\Delta u_1|_{x_1=0,a} = 0$, $s_{21}|_{x_1=0,a} = 0$ and $J_1|_{x_1=0,a} = 0$, where a is the length of the simulation box. The initial condition is set by a homogeneous swelling ratio λ_0 corresponding to an initial chemical potential, μ_0 , which can be determined analytically (Appendix C). Relative to the dry state, the initial displacement is: $\mathbf{u}_0 = \lambda_0 \mathbf{X} - \mathbf{X}$. For convenience, dimensionless quantities are used as follows: all lengths are normalized by the dry-state thickness of the hydrogel (H), time is normalized by the characteristic diffusion time, $\tau = H^2 / D$, stresses are normalized by $Nk_B T$, chemical potential by $k_B T$, and solvent concentration by $\Omega - 1$.

4.2. NUMERICAL STABILITY

To illustrate the issue of numerical stability, we compare the results from two types of spatial interpolation (Fig. 4.2). First, using eight-node quadrilateral elements with equal-order biquadratic interpolation for both the displacement and chemical potential (8u8p), the numerical results show significant oscillations at the early stage (Fig. 4.2), which decay over time and eventually vanish. This is expected because the 8u8p elements with equal order interpolation violate the LBB condition. Here, a

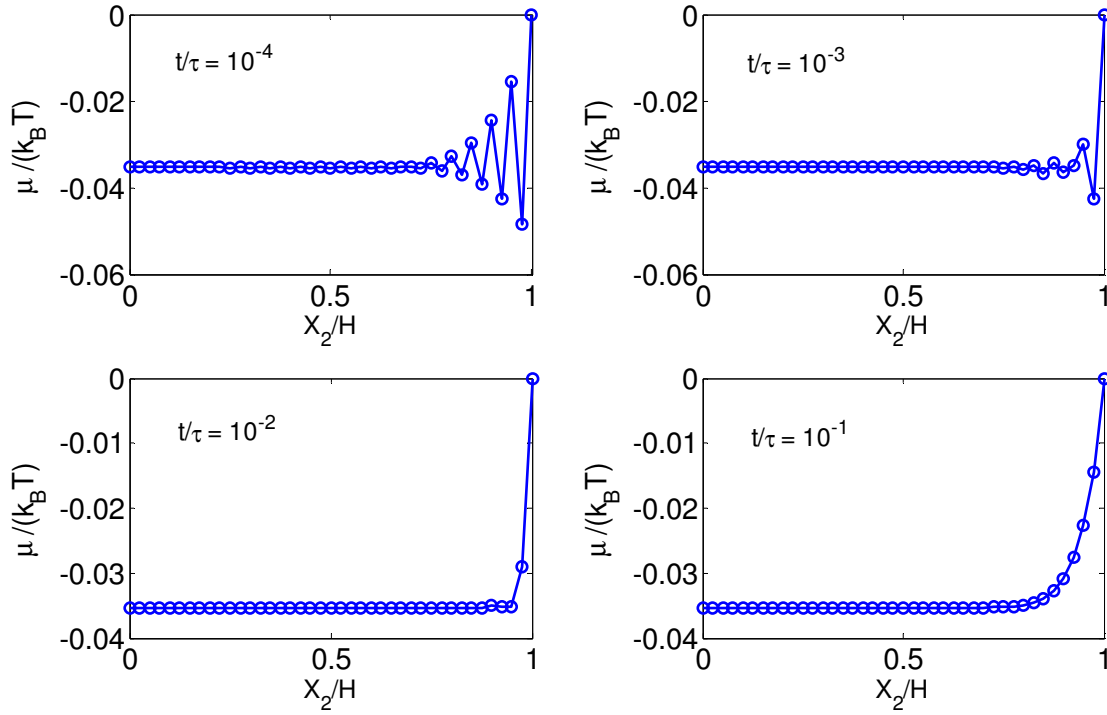


Figure 4.2: Numerical oscillations of the chemical potential in the early stage of constrained swelling for a hydrogel layer with $N\Omega = 10^{-3}$, $\chi = 0.4$, $K = 10^3 Nk_B T$, and $\lambda_0 = 1.4$, using the 8u8p elements with $n_e = 20$.

relatively large bulk modulus is used, $K = 10^3 Nk_B T$, to simulate a hydrogel with nearly incompressible constituents. The simulation domain is a square in the reference and initial states ($a/H = 1$) and is discretized by a uniform mesh with the number of elements along each side $n_e = 20$. A 3×3 Gauss integration scheme is employed for full integration. The time step is small at the early stage with $\Delta t/\tau = 10^{-5}$ and it is gradually increased until the hydrogel reaches equilibrium.

It is found that the decay of the numerical oscillation depends on the element size. The maximum oscillation occurs in the first layer of the elements below the surface, with an averaged amplitude, $A_{\max} = (\mu'' - 2\mu')/4$, where μ' and μ'' are the chemical potentials at the second and third layers of nodes, respectively; the chemical potential is zero for the surface nodes (first layer) by the boundary condition. In Figure 4.3, the oscillation amplitude A_{\max} is plotted versus time normalized by two different time scales, $\tau = H^2/D$ and $\tau_e = h_e^2/D$, where h_e is the element size ($h_e = H/n_e$). The oscillation decays faster with respect to t/τ when using smaller elements. With respect to t/τ_e , however, the oscillation amplitude evolution curves collapse, suggesting that the numerical solution becomes stable when $t/\tau_e > 10^4$. Therefore, by reducing the element size, the numerical oscillation can be suppressed after a shorter physical time. Furthermore, the numerical oscillations depend on the compressibility of the hydrogel. As shown in Fig. 4.4, by decreasing the value of the bulk modulus, the numerical oscillation can be considerably reduced, even in the very early stage ($t/\tau = 10^{-4}$). On the other hand, the oscillations become more severe and wide spread if the hydrogel is less compressible with a larger bulk modulus ($K = 10^4 Nk_B T$).

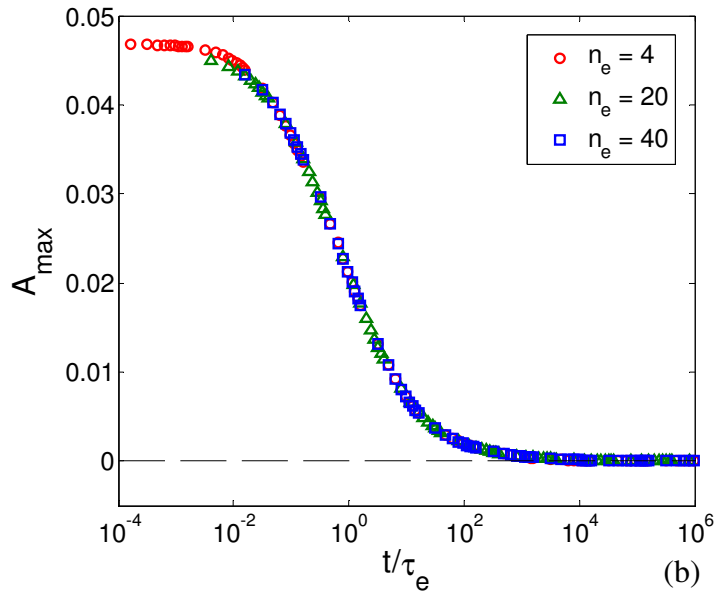
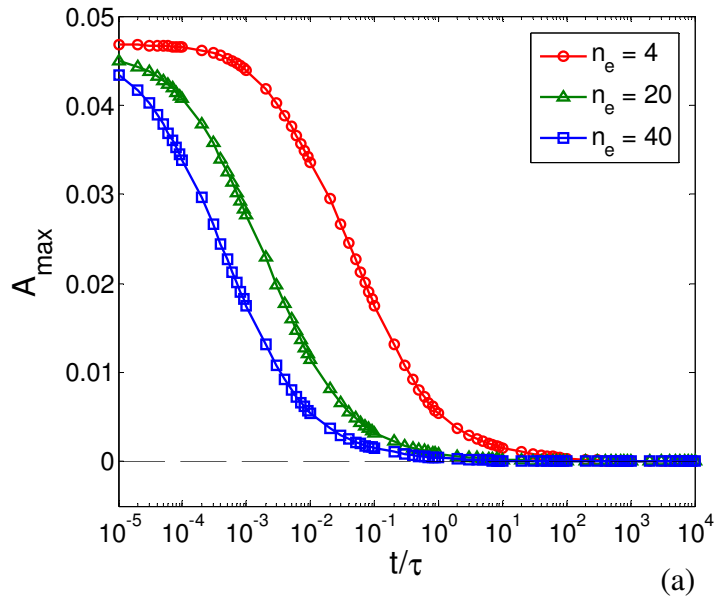


Figure 4.3: The amplitude of numerical oscillation in the chemical potential as a function of time, using different numbers of 8u8p elements. The time is normalized by the diffusion time scale for the layer thickness in (a) and the time scale corresponding to the element size in (b).

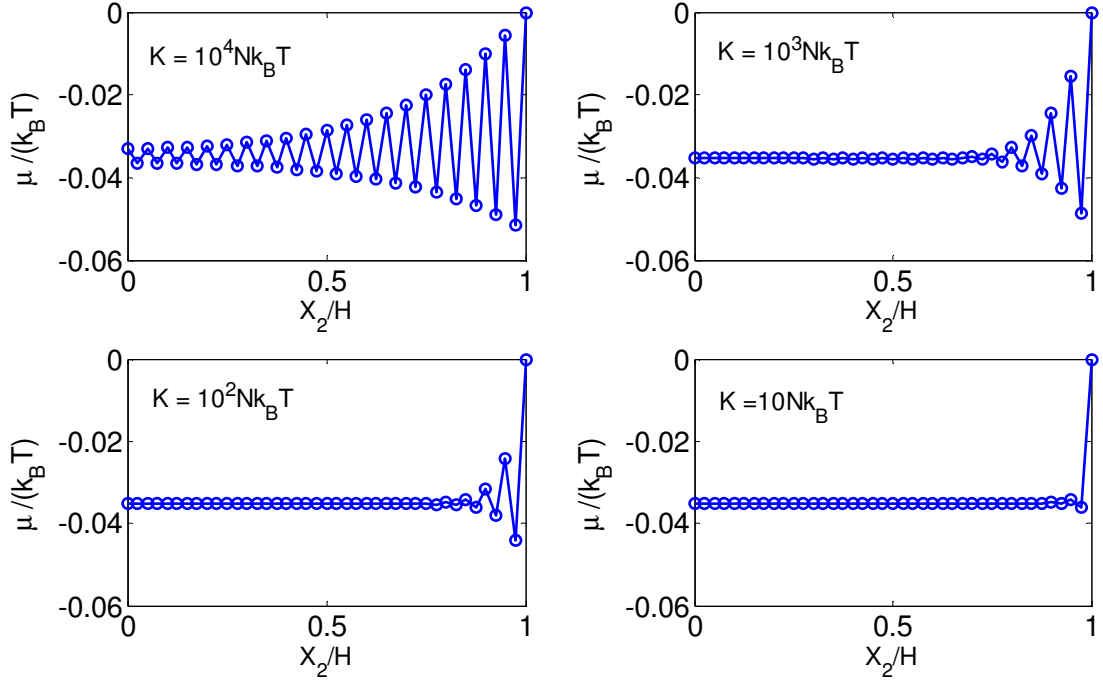


Figure 4.4: Numerical oscillations of the chemical potential at $t/\tau=10^{-4}$ for hydrogels with different bulk moduli, using 8u8p elements. The other parameters are: $N\Omega = 10^{-3}$, $\chi = 0.4$, $\lambda_0 = 1.4$, and $n_e = 20$.

The numerical oscillations are largely alleviated by using the 8u4p Taylor-Hood elements (Figure 3.1), with the biquadratic serendipity interpolation for displacement and bilinear interpolation for chemical potential, as shown in Fig. 4.5. The remaining oscillations in the early stage of the numerical results are due to sudden change of the chemical potential on the surface. These oscillations are confined within a thin surface layer, depending on the element size, and they vanish after a short time. Moreover, they do not increase significantly with increasing bulk modulus for nearly incompressible hydrogels (Fig. 4.5b). The application of the boundary conditions at $t=0^+$ with a sudden change of chemical potential on the surface causes a discontinuity with respect to time

(i.e., a step function). As a result, there is a lack of regularity in the exact solution, which inherently affects the convergence characteristics for the numerical solution at $t \rightarrow 0$ as discussed by Murad and Loula (1994) for similar problems in linear poroelasticity. This issue may be resolved by pressure stabilization schemes or use of discontinuous approximations (for chemical potential) as proposed by others for similar problems in poroelasticity (Hughes et al., 1986; Wan, 2002; Phillips, 2005; Phillips and Wheeler, 2009). Alternatively, the numerical issue may be mitigated by imposing the boundary condition with a continuous function for the chemical potential.

The same behavior, with oscillations appearing at the early stage evolution, is observed when equal order interpolation 8u8p is used, using the totally incompressible material model and finite element method presented in Sections 3.3.4-5. There, the hydrogel aggregate shows an exactly incompressible behavior at the instantaneous limit, and that makes the use of Taylor-Hood 8u4p elements necessary. That material model and finite element method will be used more extensively in Chapter 6, where it will be confirmed that 8u8p Taylor-Hood elements are sufficient to obtain a stable numerical solution.

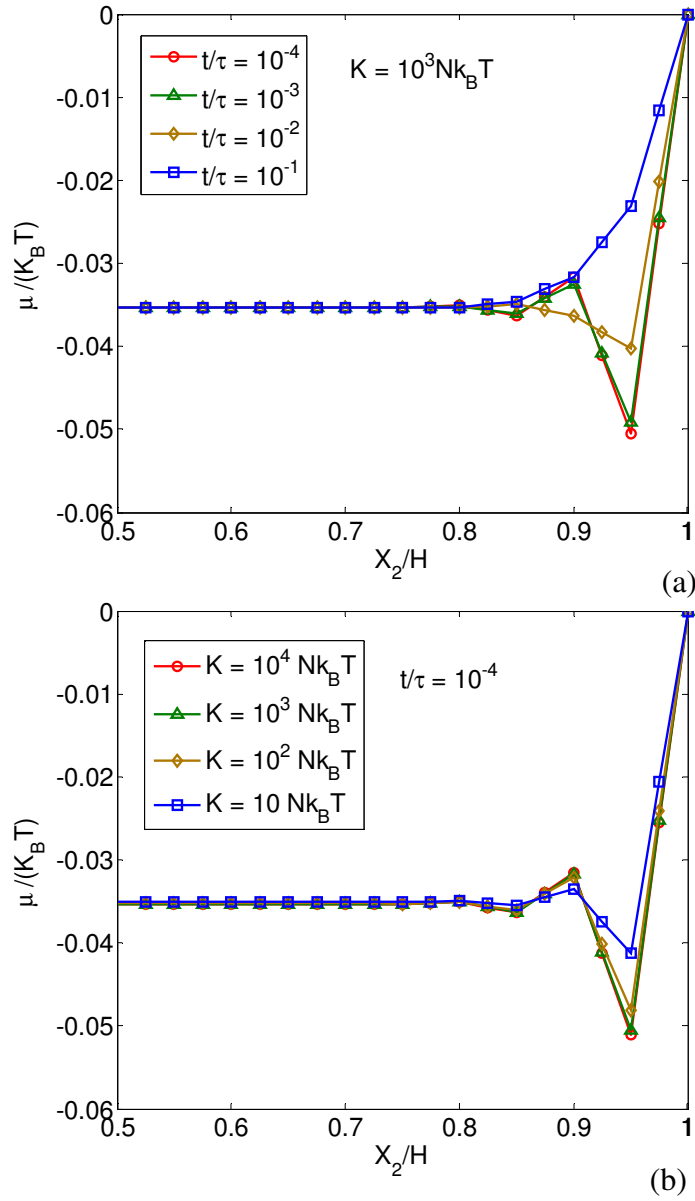


Figure 4.5: (a) Evolution of chemical potential for constrained swelling of a hydrogel layer with $N\Omega = 10^{-3}$, $\chi = 0.4$, $K = 10^3 Nk_B T$, and $\lambda_0 = 1.4$, using the 8u4p Taylor-Hood elements with $n_e = 20$. (b) Effect of bulk modulus on the numerical solution, at $t/\tau = 10^{-4}$.

4.3. CONVERGENCE STUDY

The convergence of the numerical solution is examined in three stages. First, in the early stage ($t \rightarrow 0$), we compare the numerical solution to a self-similar analytical solution. As given in Appendix C, the self-similar solution in Eq. (C.17) predicts the thickness change of the hydrogel. For a hydrogel layer with an initial thickness $h_0 = \lambda_0 H$, the thickness swelling ratio is a function of the normalized time:

$$\frac{\Delta h}{h_0} = 2 \left(\frac{\lambda_\infty}{\lambda_0} - 1 \right) \sqrt{\frac{\xi(\lambda_0) \left(\frac{t}{\tau} \right)}{\pi \lambda(\lambda_0) \left(\frac{t}{\tau} \right)}} \quad (4.1)$$

In the numerical solution, the thickness change can be obtained directly from the surface displacement. As shown in Fig. 4.6a, the numerical solution overestimates the thickness swelling ratio ($\Delta h / h_0$) in the early stage, but subsequently converges toward the self-similar solution. Similar numerical results were obtained by a one-dimensional finite difference (1D-FD) method in Chapter 2. With the implicit time integration, the numerical results using different time steps collapse onto a single curve. On the other hand, the numerical solution in the early stage depends sensitively on the element size, as shown in Fig. 4.6b. As a result, the accuracy of the numerical result in the early stage can be improved by reducing the element size, while the result in the later stage is less sensitive to the element size. Alternatively, the chemical potential on the surface can be imposed by a linear ramping from the initial value (μ_0) to the final value. In this way, as

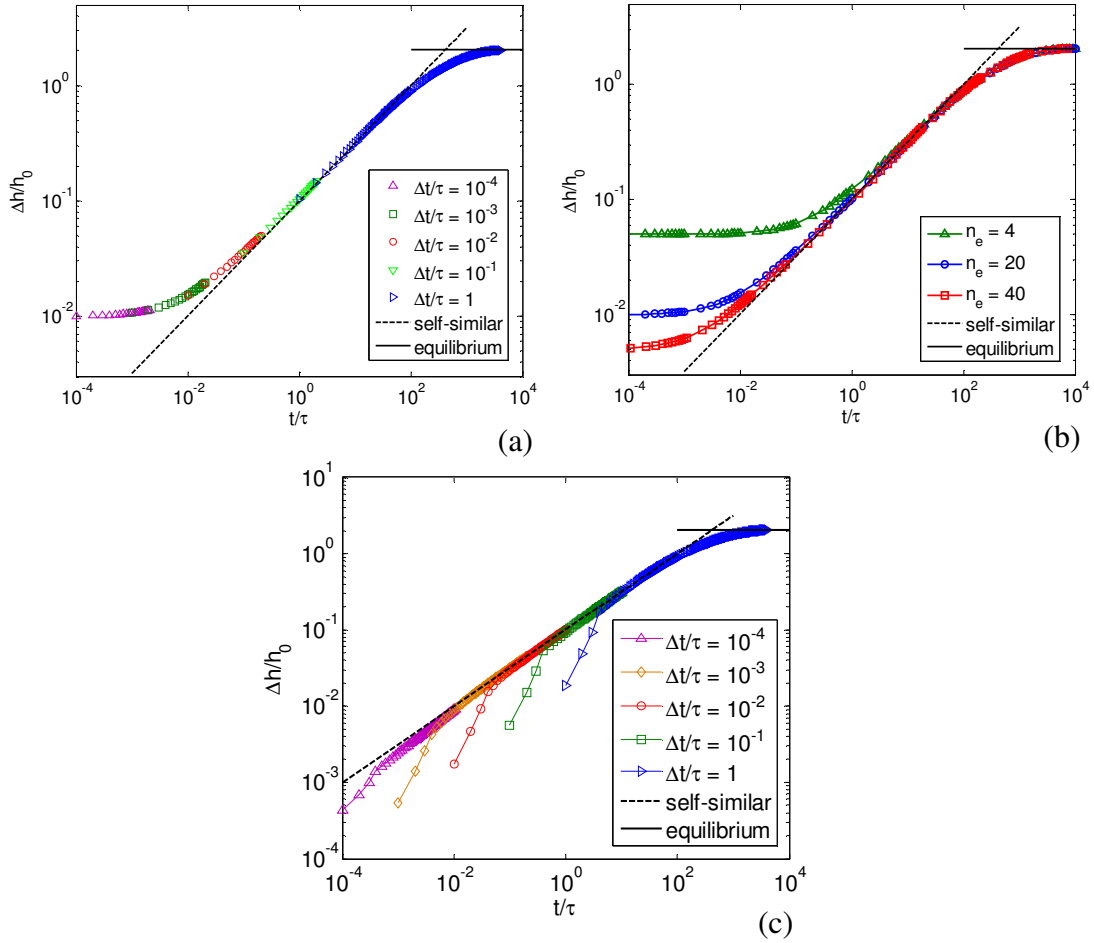


Figure 4.6: Change of thickness for constrained swelling of a hydrogel layer ($N\Omega = 10^{-3}$, $\chi = 0.4$, $K = 10^3 Nk_B T$, $\lambda_0 = 1.4$): (a) Effect of time step ($n_e = 20$); (b) Effect of mesh density; (c) Effect of time step when the boundary condition for chemical potential is applied by linear ramping in 4 time steps. The dashed line is the self-similar solution in the early stage, and the horizontal line indicates the analytical solution for equilibrium swelling ratio.

shown in Fig. 4.6c, the numerical result converges onto the self-similar solution quickly after the linear ramping, even for a very fast ramping rate ($\Delta t/\tau = 10^{-4}$ in 4 time steps). The numerical solution in this case is insensitive to the element size for $4 \leq n_e \leq 50$.

Beyond the early stage, we compare the numerical results by the 2D-FE model with those obtained by the 1D-FD method in Chapter 2, showing excellent agreement in Figure 4.7a-c for the evolution of chemical potential, the stretch in the thickness direction ($\lambda_2 = 1 + u_{2,2}$), and the nominal stress in the lateral direction (s_{11}). Note that the stretch and nominal stress are evaluated at the integration points of the 2D-FE model. Figure 4.8d shows the comparison for the thickness swelling ratio as a function of time for hydrogels with $\chi = 0.2, 0.4$ and 0.6 . Again, the agreement between the two numerical methods is excellent. While the finite difference method is limited to 1D problems, the finite element method can be used to study laterally inhomogeneous swelling and other 2D problems as demonstrated in Chapters 5 and 6.

The transient evolution of constrained swelling eventually reaches an equilibrium state, with a uniform chemical potential ($\mu = 0$), a constant thickness swelling ratio ($h/H = \lambda_\infty$), and a constant in-plane stress. The analytical solution for the equilibrium swelling ratio (λ_∞) is given in Appendix C. We note that the equilibrium swelling ratio depends on the compressibility of the gel. As shown in Fig. 4.8, the equilibrium swelling ratio for the constrained hydrogel layer decreases with increasing compressibility (decreasing bulk modulus). On the other hand, the incompressible limit is reached closely for $K > 10^2 Nk_B T$. Moreover, the effect of compressibility depends on the initial swelling ratio (λ_0). In all cases, the convergence of the numerical solution in the equilibrium state is confirmed by comparing to the analytical solution, as shown in Fig. 4.6.

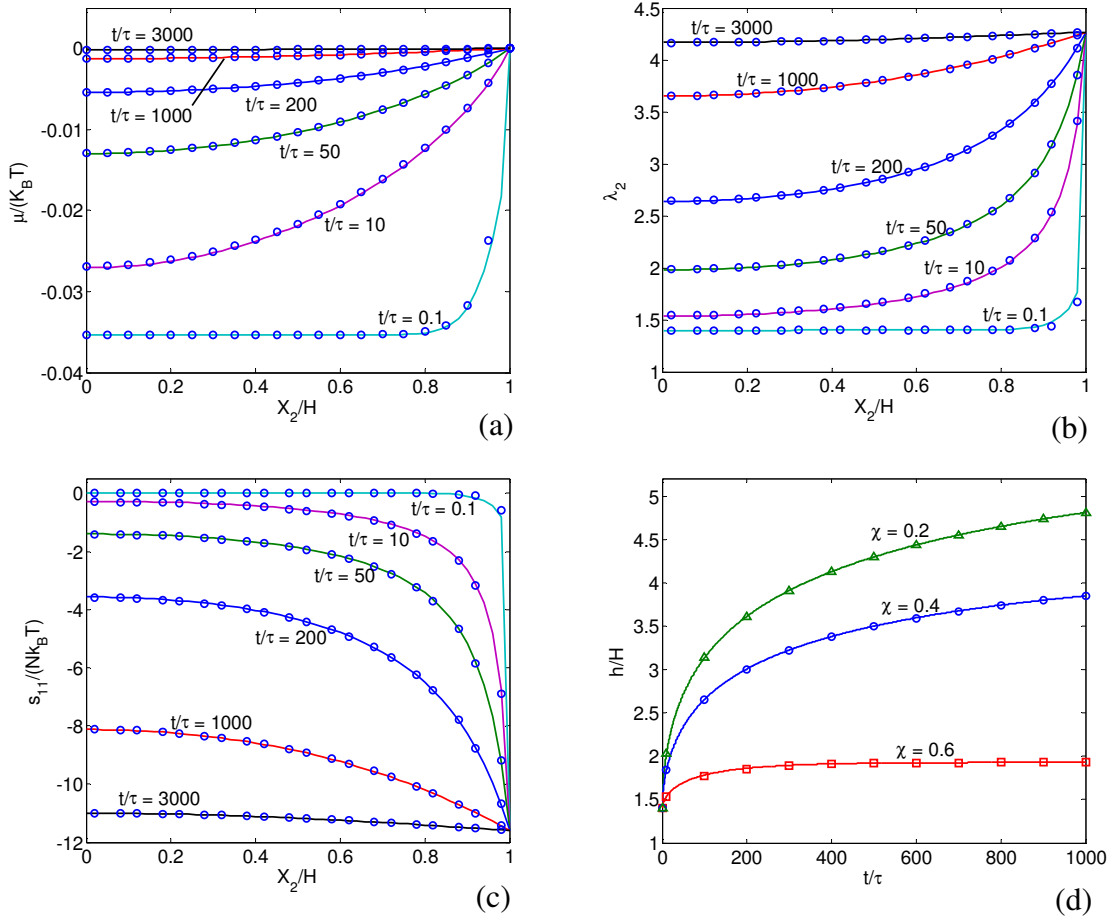


Figure 4.7: Comparison between the transient finite element results for constrained swelling (circles) and previous results obtained by a finite difference method (solid lines). The former is for $K = 10^3 Nk_B T$, while the latter is for a hydrogel with incompressible constituents ($K \rightarrow \infty$); the other material parameters are identical: $N\Omega = 10^{-3}$, $\chi = 0.4$, and $\lambda_0 = 1.4$. (a) Chemical potential; (b) Stretch in the thickness direction; (c) In-plane nominal stress; (d) Evolution of thickness swelling ratio for different values of χ .

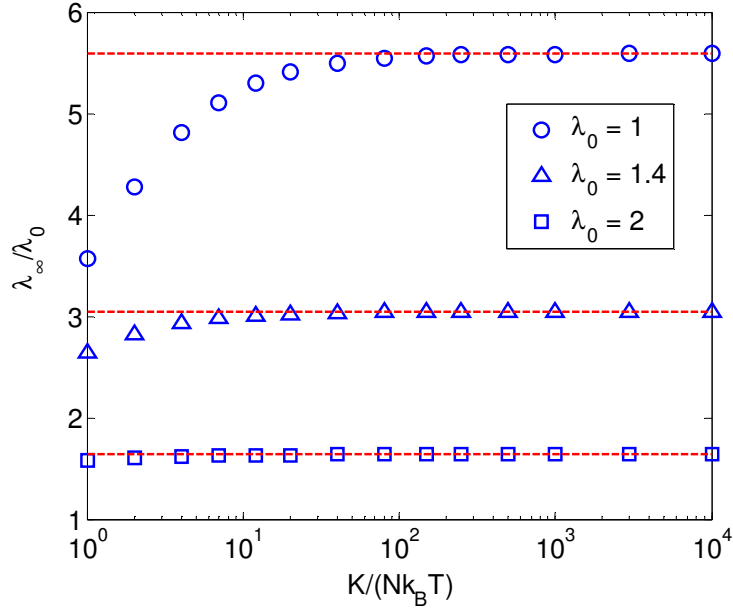


Figure 4.8: Effect of bulk modulus on the equilibrium swelling ratio for constrained hydrogel layers with $\chi = 0.4$ and $N\Omega = 10^{-3}$, in comparison with the incompressible limits (dashed lines).

4.4. SWELLING INDUCED SURFACE INSTABILITY

The constrained swelling induces a compressive in-plane stress in the hydrogel (Fig. 4.7c), which may cause surface instability (creasing or wrinkling) as observed in experiments (Tanaka et al., 1987; Trujillo et al., 2008; Guvendiren, et al., 2010). Several previous studies have predicted swell induced surface instability based on energy or equilibrium analyses (Hong et al., 2009; Kang and Huang, 2010b; Wu et al., 2013; Weiss et al., 2013). In most experiments, however, surface instability develops during the transient stage of swelling. In the present study, using the 2D-FE model, we have intentionally suppressed the surface instability by not allowing the nodes on the top surface of the hydrogel to move in the direction parallel to the surface for the results in Sections 4.2 and 4.3; this is equivalent to attaching a rigid, permeable cap layer onto the

surface of the hydrogel. If such constraint is relaxed, the surface may become unstable before the hydrogel reaches the equilibrium swelling state, depending on the material properties ($N\Omega$, χ , and K). The physical instability in turn would cause numerical instability due to severe distortion and possible interpenetration of the elements near the surface, at which point the numerical calculation has to be terminated.

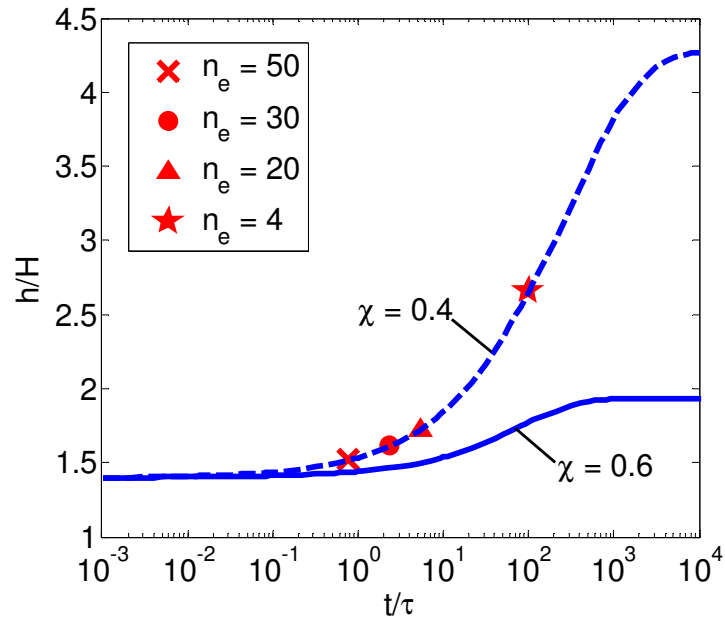


Figure 4.9: Thickness swelling ratio as a function of time for hydrogels with $\chi = 0.4$ and 0.6 . The dashed line shows the stabilized finite element simulation (with surface constraint) for $\chi = 0.4$. The symbols mark the points where the calculations without surface constraint are terminated due to swell induced surface instability, depending on the mesh density. The solid line shows that the swelling is stable for $\chi = 0.6$ even without the surface constraint. Other parameters: $N\Omega = 10^{-3}$, $K = 10^3 Nk_B T$, and $\lambda_0 = 1.4$.

As shown in Fig. 4.9, for a hydrogel with $\chi = 0.6$ (poor solvent), the constrained swelling is stable all the way until equilibrium. However, with $\chi = 0.4$ (good solvent), the predicted equilibrium swelling ratio is much larger and the numerical solution (without surface constraint) becomes unstable during the transient stage (marked by the termination of the calculation). Theoretically, as the surface reaches the equilibrium swelling ratio instantaneously by the condition of local equilibrium, it becomes unstable instantaneously in this case. Numerically, the instability occurs after a delay depending on the element size. As shown in Fig. 4.9, with decreasing element size (increasing n_e), the time to instability shortens, approaching the theoretical prediction of instantaneous instability.

To simulate swelling induced surface instability, a self-contact surface condition must be implemented to prevent interpenetration, which is left for future works. The instantaneous instability could be mitigated by including viscous damping in the constitutive model (Wang and Hong, 2012a), which may represent the physical process of viscoelastic deformation of the polymer. Alternatively, we may assume a thin surface layer with different material properties, which is fairly common in experiments due to the crosslinking or surface treatment processes (Guvendiren, et al., 2010). When the surface layer is stiffer or less hydrophilic (higher crosslink density N or larger χ), swelling induced surface instability is regulated to form wrinkles (rather than self-contacting creases), as shown in Figure 4.10a. For this simulation, a 2D-FE model with 50×50 elements ($n_e = 50$) are used. The surface layer is modeled by the topmost two layers of elements with $N\Omega = 10^{-2}$, while the remaining part of the gel is more compliant with $N\Omega = 10^{-3}$; the other material properties are identical ($\chi = 0.4$ and $K = 10^3 Nk_B T$). With a small perturbation to a surface node, the surface evolves into periodic wrinkles with a particular wavelength, while the wrinkle amplitude grows with time (Fig. 4.10b). The

kinetics of swell-induced wrinkling appears to be similar to wrinkling of an elastic film on a viscoelastic substrate (Huang, 2005; Huang and Im, 2006), but the underlying mechanism is quite different in the present case (i.e., poroelastic vs viscoelastic) and a systematic study will be presented elsewhere.

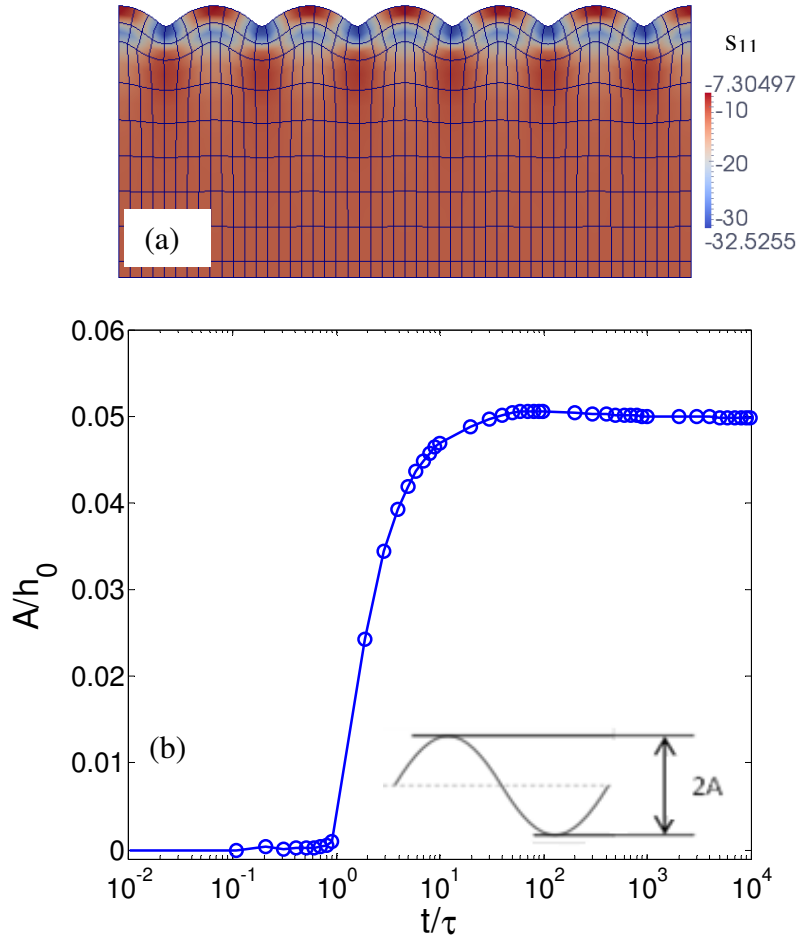


Figure 4.10: (a) Swelling induced surface wrinkles for a hydrogel with a stiff surface layer, showing only the top part of the swollen gel in the equilibrium state, with color contour for the compressive in-plane stress. (b) Evolution of the

4.5. SUMMARY

Numerical results are presented for constrained swelling, using the theory and the finite element method for hydrogels with compressible constituents. The numerical stability issues associated with the LBB condition and the instantaneous response are studied, and the use of 8u4p Taylor-Hood elements helps resolve them. The transient behavior of constrained swelling is compared to the self-similar solution in the early stage, the previous results by a finite difference method, and the analytical solution for equilibrium state. It is found that convergence of the numerical solution in the early stage can be improved by linear ramping of the chemical potential boundary condition. For a hydrogel in a good solvent, constrained swelling leads to instantaneous surface instability. By assuming a stiff surface layer, swelling induced growth of surface wrinkles can be simulated. These numerical results not only demonstrate the robustness of the present finite element method, but also suggest interesting transient phenomena (e.g., swell induced growth of surface wrinkles or creases) for future studies using the numerical method.

Chapter 5

Indentation of Hydrogel Layers

This chapter focuses on the indentation of hydrogel layers, presenting numerical results and studying the inhomogeneous transient response of the hydrogels solving the appropriate initial/boundary value problems. The finite element method for hydrogels with incompressible constituents presented in Sections 3.2-3 will be used in this chapter.

Recently, the indentation method has been used to characterize poroelastic properties of hydrogels (Hui et al., 2006; Yoon et al., 2010; Hu et al., 2010, 2011 & 2012). Capturing the force relaxation behavior for known/fixed indentation displacement depth, and known geometric properties of the indenter, the material properties of the material are obtained based on a linear poroelasticity theory. The indentation displacements imposed on the are relatively shallow indentation even though this is often an issue due to the very small thickness of the hydrogel layers. In this chapter we want to demonstrate the capacity of the proposed finite element method to simulate hydrogel indentation, and also extend the the use of the indentation method to characterize the properties of the hydrogels based on the nonlinear continuum theory. The 2D finite element model for flat punch indentation adopted for this study is presented in Section 5.1. Numerical results for displacement controlled indentation are presented and discussed, in Section 5.2, and the work of this chapter on indentation of hydrogel layers is summarized in Section 5.3.

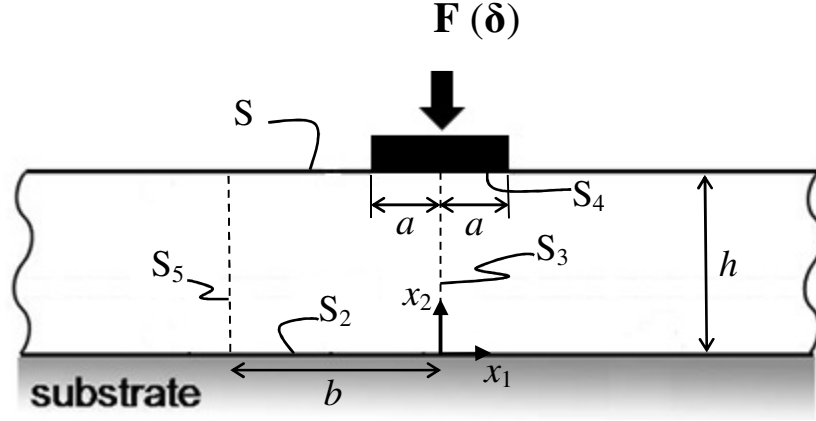


Figure 5.1: Schematic of a hydrogel layer subject to rigid flat-punch indentation.

5.1. FLAT PUNCH INDENTATION MODEL

For the second example, we consider a hydrogel layer subject to indentation by a rigid flat punch. Before indentation, the hydrogel is assumed to be fully swollen with $\mu=0$ and $\lambda_1 = \lambda_2 = \lambda_3 = \lambda_0$ ($h = \lambda_0 H$), where λ_0 can be determined analytically (Appendix A). As shown in Fig. 5.1, the flat punch has a width of $2a$ and an infinite length so that the plane strain condition applies. By symmetry, only half of the hydrogel is modelled with a symmetric boundary condition at $x_1 = 0$ (S_3). The surface under the flat punch is subjected to a mixed displacement/flux boundary condition (S_4), assuming a normal indentation displacement ($\Delta u_2 = -\delta$ for $t > 0$) along with zero tangential displacement ($\Delta u_1 = 0$, no slip) and zero flux ($J_2 = 0$); the rest of the surface is exposed with zero chemical potential and zero traction (S_1). Far away from the indenter, the effect of indentation diminishes, and the boundary condition on S_5 ($x_1 = -b$) is less significant as long as the computational domain is sufficiently large (e.g., $b \gg a$). In the present study, we take $b = 10a$ and assume the symmetric boundary condition on S_5 . The bottom

surface of the gel is attached to a rigid substrate with zero displacement and zero flux (S_2). Compared to Fig. 4.1, the flat-punch indentation problem introduces a new boundary condition S_4 , which has to be implemented with care for numerical accuracy. Throughout this section, the plane-strain 8u4p Taylor-Hood elements (Fig. 3.1) are used. In all simulations, a square domain of the gel ($b = h$) is modeled by a uniform mesh with $n_e = 50$, which is found to be sufficient for convergence except for the stress singularity near the edge of the flat punch. Time is normalized by the diffusion time scale associated with the contact width, $\tau = a^2 / D$.

5.2. DISPLACEMENT CONTROLLED INDENTATION

5.2.1. Instantaneous and equilibrium limits

For each indentation depth δ , two elastic limits are expected: an instantaneous response ($t \rightarrow 0$) and an equilibrium state ($t \rightarrow \infty$), with the transient response in between depending on the solvent diffusion kinetics. For shallow indentation ($\delta \ll a, h$), the indentation behavior of the hydrogel can be approximated by linear poroelasticity (Hui et al., 2006; Hu et al., 2010), with two linear elastic limits. As shown in Appendix A, the swollen hydrogel has an effective shear modulus following Eq. (A.18), while the effective Poisson's ratio is 0.5 (incompressible) for the instantaneous response and is less than 0.5 for the equilibrium response. The equilibrium Poisson's ratio is related to the intrinsic properties of the hydrogel by Eq. (A.8). In the present case, considering a hydrogel with $N\Omega = 10^{-3}$, $\chi = 0.2$, and $K = 10^3 Nk_B T$, we have $\nu_0 = 0.499$ for the instantaneous response and $\nu_\infty = 0.2415$ for the equilibrium state. The instantaneous Poisson's ratio is slightly less than 0.5, to be consistent with the finite bulk modulus. Therefore, the difference between the two linear elastic limits simply results from the Poisson's ratio effect.

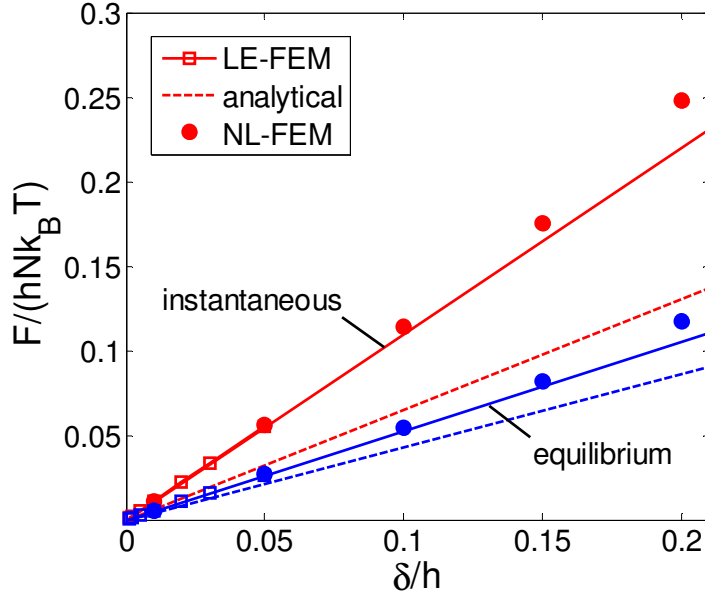


Figure 5.2: Normalized indentation force versus depth at the two elastic limits, predicted by linear and nonlinear finite element methods, for a hydrogel with $\chi = 0.2$, $N\Omega = 10^{-3}$ and $K = 10^3 Nk_B T$. The indenter half-width is $a/h = 0.1$. The approximate analytical solution in Eq. (B.5) is shown as dashed lines for comparison.

Using a linear elastic finite element model (LE-FEM) in ABAQUS Standard (ABAQUS, 2013) with the effective elastic properties of the hydrogel, we obtain the linear elastic limits for flat-punch indentation. Figure 5.2 plots the normalized indentation force versus the indentation depth at the elastic limits. The nearly incompressible instantaneous response imposes a numerical challenge even for the linear elastic model, which converges only for shallow indentation ($\delta/h < 0.05$). The numerical results are extrapolated linearly to deeper indentation for comparison. In addition, we present an approximate analytical solution in Appendix D based on an elastic half-space solution.

However, as shown in Fig. 5.2, the analytical solution considerably underestimates the indentation forces at the elastic limits for the hydrogel layer subject to a prescribed indentation depth. The presence of a rigid substrate underneath the hydrogel significantly increases the contact stiffness at both elastic limits under the plane strain condition, even for a very shallow indentation.

5.2.2. Application of boundary conditions

To simulate displacement controlled indentation of the hydrogel layer, the nodal displacements under the indenter are specified as a function of time (e.g., a step function). Due to the intimate coupling between the solvent diffusion and the network deformation, we have found that the application of the displacement boundary condition must be implemented with some care. Specifically, the process of updating only the known displacement increments, followed by computing the tangent stiffness matrix and internal forces associated with this new artificial state, and then solving for the remaining degrees of freedom leads to non-physical results. In particular, the instantaneous elastic limit is not correctly predicted using the above procedure.

To obtain accurate numerical results for the flat-punch indentation at the instantaneous limit ($t \rightarrow 0$), a penalty method (Hughes, 1987) was used in this work for the application of the displacement boundary condition under the indenter (S4). Essentially, as an approximation to the Lagrange multiplier method for imposing the displacement constraint, the tangent stiffness and residual in Eq. (3.26) are modified with sufficiently large spring stiffness associated with each prescribed boundary displacement. We note that other methods utilizing the tangent stiffness based upon the prior deformation and chemical potential state, and then applying the displacement boundary conditions can be implemented successfully as well.

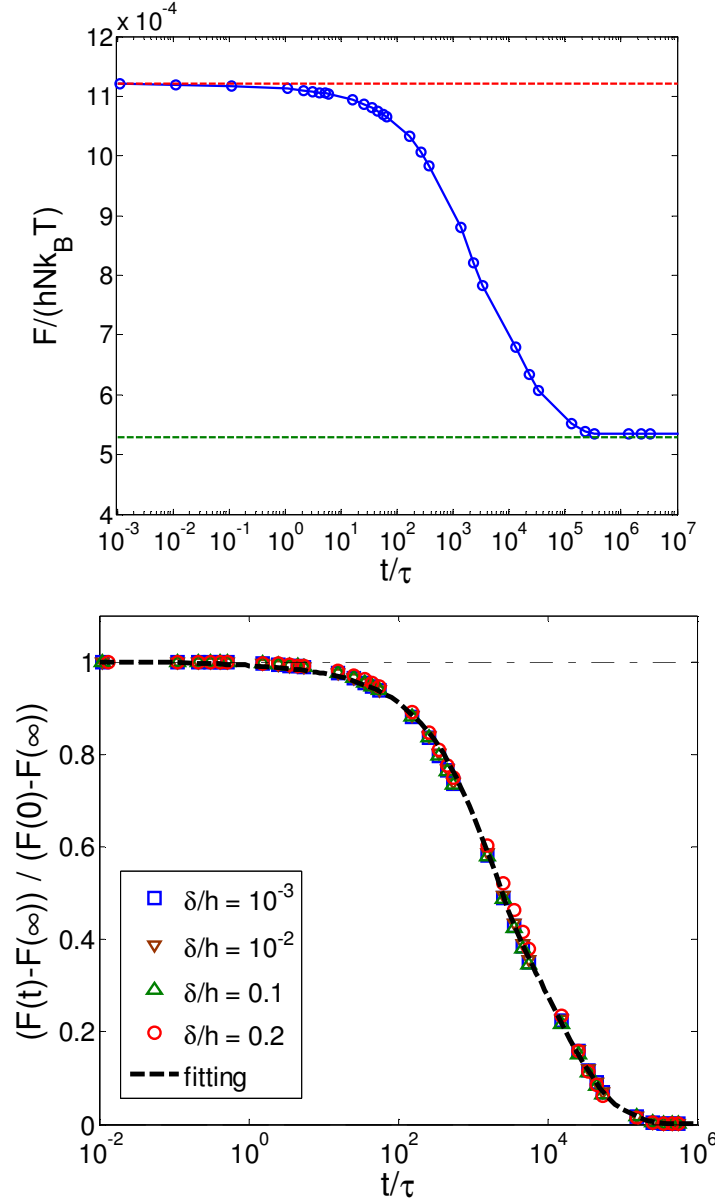


Figure 5.3: (a) Indentation force as a function of time for a shallow indentation ($\delta/h = 10^{-3}$), in comparison with the linear elastic limits (dashed lines) for instantaneous and equilibrium responses. (b) Normalized indentation force relaxation for various indentation depths, fitted by a function, $g(t/\tau) = 0.25 \exp(-7t/\tau) + 0.75 \exp(-\sqrt{t/\tau})$. Material parameters of the hydrogel are: $\chi = 0.2$, $N\Omega = 10^{-3}$, and $K = 10^3 Nk_B T$.

5.2.3. Transient response

Figure 5.3a shows the transient indentation relaxation behavior for a shallow indentation, $\delta/h = 10^{-3}$, bounded by the two linear elastic limits (dashed lines). Similar results are obtained for relatively deep indentation up to $\delta/h = 0.2$. As shown in Fig. 5.2, the instantaneous and equilibrium indentation forces obtained from the nonlinear finite element method (NL-FEM) are in good agreement with the linear elastic model in the shallow indentation regime ($\delta/h < 0.05$). As the indentation depth increases, the linear elastic model (LE-FEM) becomes less accurate and underestimates the indentation forces at both limits. Following Hu et al [2010], we re-normalize the force as $\bar{F}(t) = (F(t) - F(\infty)) / (F(0) - F(\infty))$ in Fig. 5.3b, where $F(0)$ and $F(\infty)$ are the two elastic limits obtained from the nonlinear finite element method. It is found that, for a specific set of material properties, the normalized indentation relaxation curve is independent of the indentation depth, even for relatively deep indentations. A function $g(t/\tau)$ can then be used to fit the transient indentation relaxation curve, which may be used to determine the time scale and the diffusivity by comparing to experimental measurements. We note that the present result is different from a previous study on spherical indentation of hydrogel layers (Hu et al., 2011), where the normalized relaxation curve was found to depend on the relative indentation depth δ/h . In the present study, the contact width (a) is relatively small compared to the layer thickness (h) and it does not depend on the indentation depth, a rather special case due to the use of rigid, flat punch.

Figure 5.4 shows transient evolution of the chemical potential and stress fields in a hydrogel layer subject to flat punch indentation with $\delta/h = 0.1$. Upon indentation, the chemical potential becomes inhomogeneous instantaneously, driving solvent diffusion in the hydrogel. Note that the chemical potential becomes positive under the indentation.

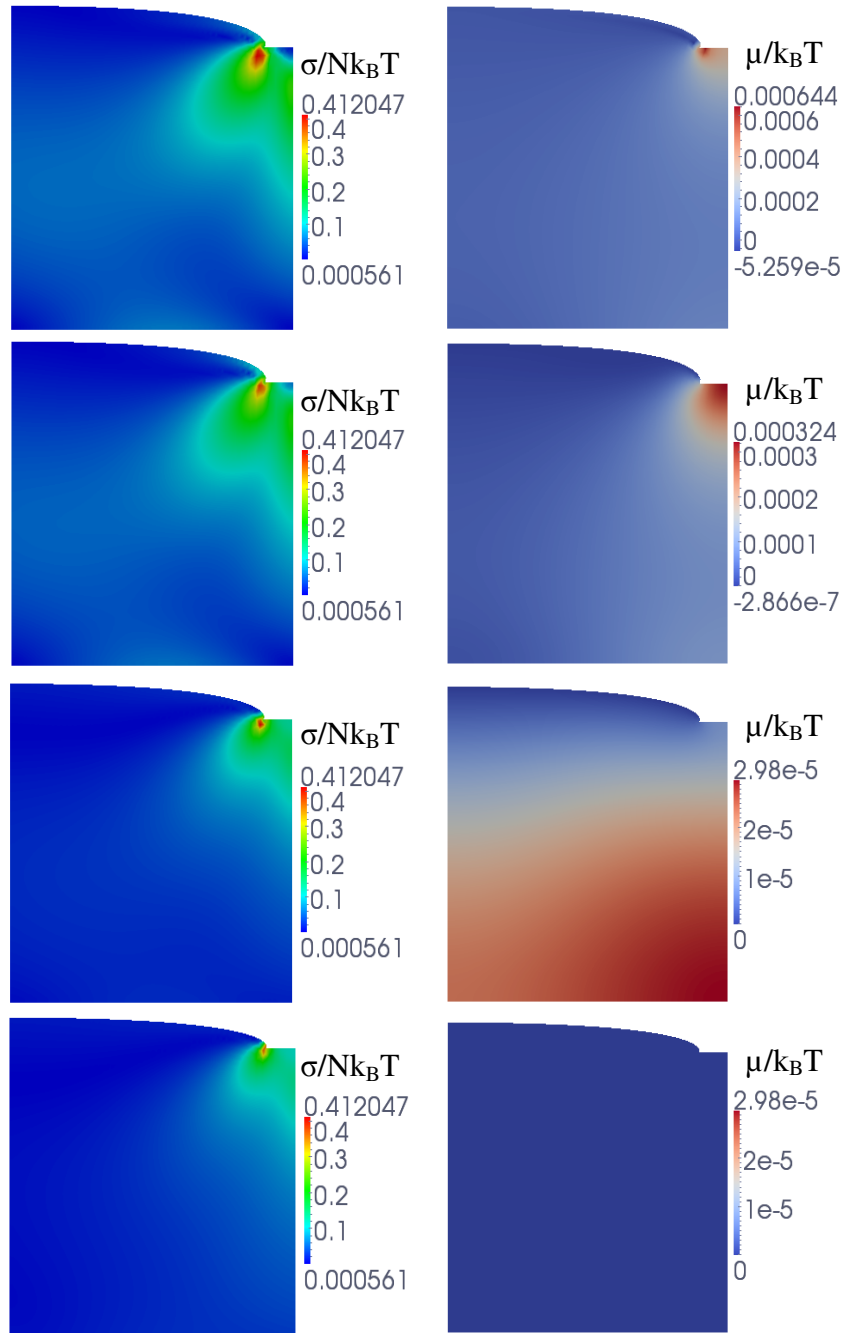


Figure 5.4: Evolution of the von Mises stress (left) and chemical potential (right) fields in a hydrogel layer ($\chi=0.2$, $N\Omega=10^{-3}$, $K=10^3 Nk_B T$) subject to flat punch indentation with $a/h=0.1$ and $\delta/h=0.1$, at normalized time $t/\tau=1, 10^2, 10^4, 10^7$ (from top to bottom).

The von Mises stress distribution exhibits a characteristic pattern of elastic contact, with a singularity at the edge of the flat punch. Solvent diffusion then leads to relaxation of the stress and indentation force, a poroelastic effect as discussed in previous studies (Hui et al., 2006; Hu et al., 2010). Eventually, the hydrogel reaches an equilibrium state with a homogeneous chemical potential ($\mu=0$) but an inhomogeneous stress distribution (with singularity). Correspondingly, the solvent concentration (not shown) evolves from the homogeneous initial state to an inhomogeneous equilibrium state under the indentation. Of particular interest are the distributions of the contact tractions. The analytical solution for an elastic half space as given in Eq. (D.1) predicts an oscillatory stress singularity at the edge of the flat punch ($|x_1| \rightarrow a$). As shown in Fig. 5.5, the numerical results for the instantaneous and equilibrium responses of the hydrogel layer are in good agreement with the analytical solution, despite the fairly coarse mesh used in the present study. The surface tractions were calculated by following the recovery procedure presented by Haber [1985] and using two quarter point elements adjacent to the edge of the indenter to capture the stress singularity. Interestingly, while the normal traction relaxes from the instantaneous limit to the equilibrium state, the magnitude of shear traction under the indenter increases due to the no-slip contact condition.

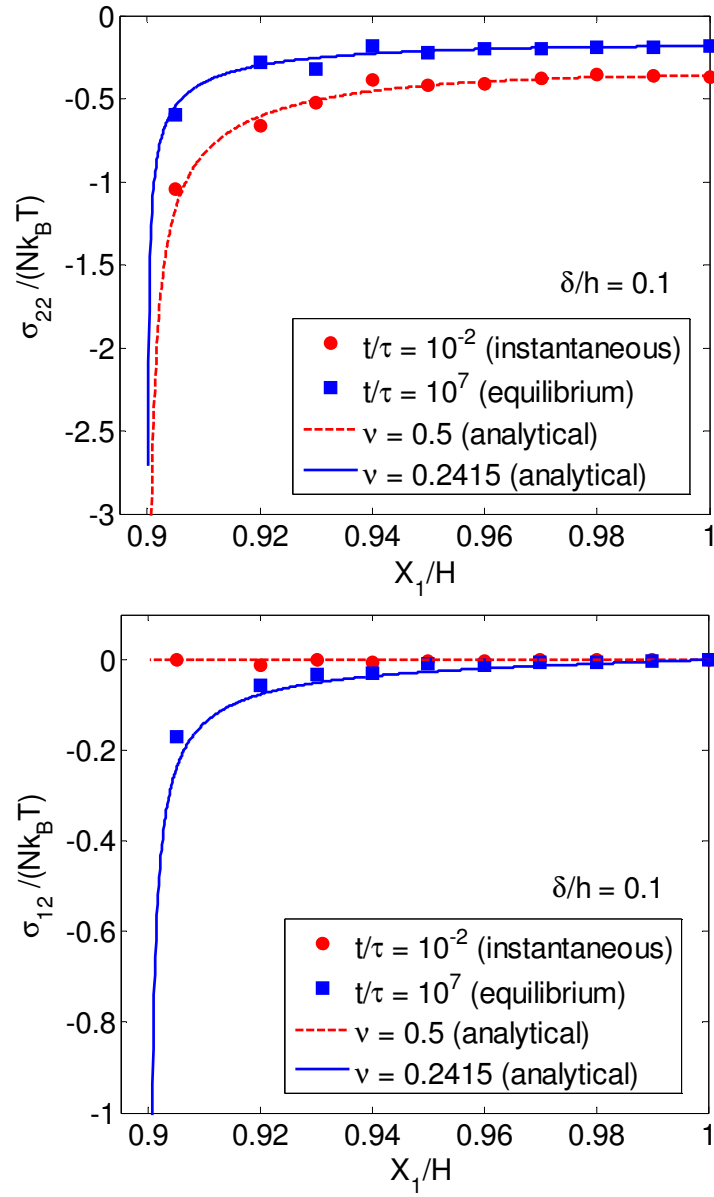


Figure 5.5: Normal and shear contact tractions under the flat-punch indenter with $a/h=0.1$ and $\delta/h=0.1$, comparing the numerical solutions with the analytical predictions at the elastic limits for a hydrogel layer ($\chi=0.2$, $N\Omega=10^{-3}$, $K=10^3 Nk_B T$).

5.2.3. Linear poroelastic indentation

Previous studies by Hu et al. (2010 and 2012) have found that the linear poroelastic indentation relaxation can be written in a general form as

$$\bar{F} = \frac{F(t) - F(\infty)}{F(0) - F(\infty)} = g(t / \tau_*) \quad (5.1)$$

where τ_* is a time scale in linear poroelasticity. By using the linearized elastic properties (G and ν_∞) of the hydrogel the effective diffusivity directly from Eq. (2.56),

$$D^* = \frac{2(1-\nu_\infty)(\lambda_0^3 - 1)\Omega G}{(1-2\nu_\infty)\lambda_0^3 k_B T} D \quad (5.2)$$

the linear poroelastic time scale is defined as $\tau_* = a^2 / D^*$. Numerical results by Hu et al. [2010 and 2012] suggested that the function $g(t / \tau_*)$ is independent of Poisson's ratio for a variety of indenters, but not including the case of plane-strain flat punch indentation. The numerical results from the present study show that the flat punch indentation relaxation does depend on the effective Poisson's ratio (ν_∞) of the hydrogel. By Eq. (A.8), we vary the effective Poisson's ratio by varying the intrinsic properties of the hydrogel. For each Poisson's ratio, we may have different combinations of the intrinsic properties (Table 5.1), but the numerical results after normalizing the time with τ_* collapse onto one curve, as shown in Figure 5.6.

However, the transient relaxation curve varies slightly with different Poisson's ratios. Define a characteristic relaxation time, t_{50} , by setting $\bar{F}(t_{50}) = 0.5$. Figure 5.7 shows that the normalized relaxation time increases with increasing Poisson's ratio. This dependence on Poisson's ratio could be pertinent for the specific geometry of the present problem, not necessarily applicable for other indentation geometries. In addition, it is found that the normalized relaxation time depends on the contact width (a/h), but

independent of the relative indentation depth up to $\delta/h=0.2$. As proposed and demonstrated in previous studies (Hui et al., 2006; Hu et al., 2010 and 2012)), the indentation relaxation behavior can be used as an experimental method for characterizing the mechanical and transport properties of hydrogels.

While the previous studies have used the linear poroelasticity theory, limited to shallow indentation, the present study suggests that the method can be extended to relatively deep indentation by using the nonlinear theory. Specifically, the measured instantaneous and equilibrium indentation forces may be used to determine the elastic properties of the hydrogel. Using the nonlinear theory, the elastic properties of a hydrogel depend on three parameters, χ , $Nk_B T$, and K , which can be determined from the indentation forces at the two elastic limits, $F(0)$ and $F(\infty)$, along with an independent measurement of the swelling ratio (λ_0). In the case of shallow indentation, the linearized elastic properties, G and ν_∞ , can be determined based on the linear elastic solution, and then the intrinsic properties can be deduced using Eqs. (A.18) and (A.8). Because of the introduction of a finite bulk modulus (K), an additional measurement is necessary. The kinetics of solvent diffusion in the hydrogel is characterized by the diffusivity (D), which can be determined from the transient indentation relaxation measurement. By comparing the experimental measurements and the normalized relaxation curves (Fig. 5.6), the time scale τ_* can be determined, with which the effective diffusivity D^* can be obtained and the intrinsic diffusivity D can then be deduced from Eq. (5.2). The time scale can also be determined more directly from measurement of t_{50} in comparison with the numerical results in Fig. 5.7.

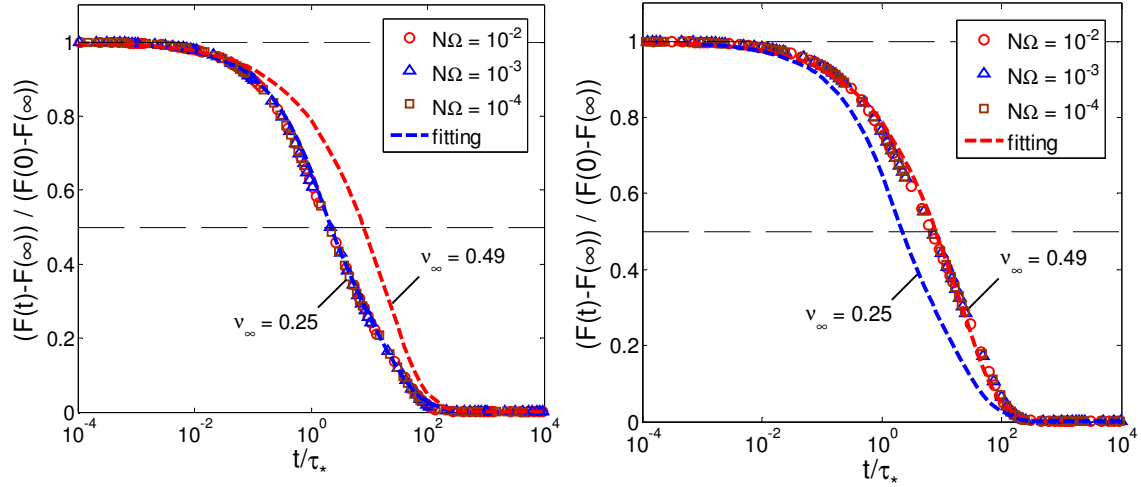


Figure 5.6: Normalized indentation force relaxation for plane-strain flat punch indentation, with various combinations of material parameters (Table 5.1) corresponding to two effective Poisson's ratios: (a) $\nu_\infty = 0.25$ and (b) $\nu_\infty = 0.49$. The numerical results are fitted by two functions,

$$g_1(t/\tau_*) = 0.25 \exp(-7910t/\tau_*) + 0.75 \exp(-33.6\sqrt{t/\tau_*})$$

$$g_2(t/\tau_*) = 0.2 \exp(-330t/\tau_*) + 0.8 \exp(-28\sqrt{t/\tau_*})$$

	$N\Omega = 10^{-2}$	$N\Omega = 10^{-3}$	$N\Omega = 10^{-4}$
$\nu_\infty = 0.25$	$\chi = 0.39$	$\chi = 0.4$	$\chi = 0.42$
$\nu_\infty = 0.49$	$\chi = 0.95$	$\chi = 0.68$	$\chi = 0.57$

Table 5.1: Intrinsic properties of hydrogels for two different Poisson's ratios ($K = 10^3 Nk_b T$ for all cases).

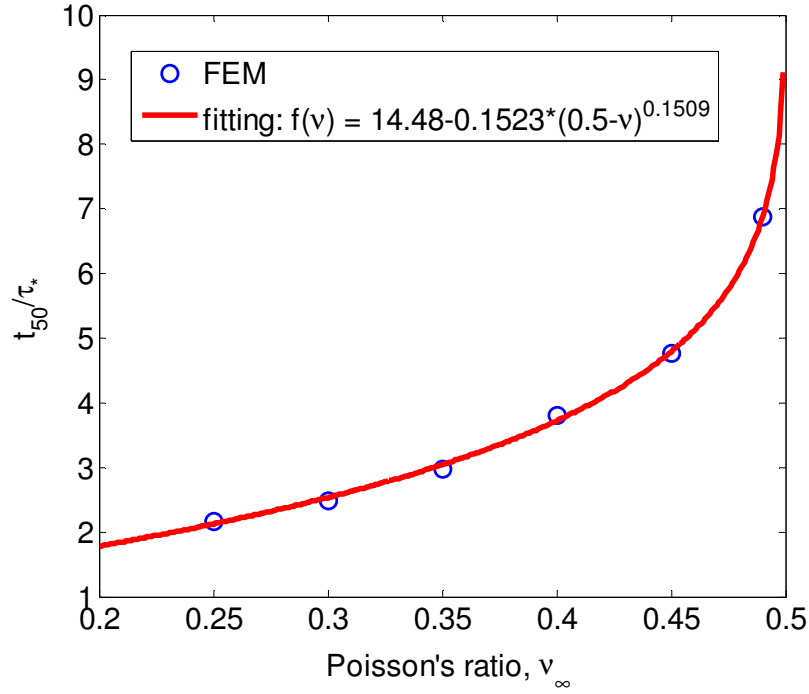


Figure 5.7: Normalized characteristic relaxation time t_{50}/τ_* as a function of Poisson's ratios for plane-strain flat punch indentation with $a/h = 0.1$.

5.2.4. Effect of loading rate

Finally we consider the effect of loading rate on the transient indentation relaxation behavior. Instead of imposing a constant indentation depth instantaneously, a linear ramping of the indentation displacement in time is applied until it reaches a final value δ^* (inset of Fig. 5.8). The time to reach the final depth is denoted as t^* , with a loading rate δ^*/t^* . In Figure 5.8, the indentation force relaxation is plotted for three different loading rates with $\delta^*/h = 0.1$, in comparison with the result for instantaneous loading ($t^* = 0$). It is found that the peak force decreases with decreasing loading rate, a result of poroelastic relaxation due to solvent diffusion during the loading period (

$0 < t < t^*$). For the case of high loading rate, the peak force is close to the instantaneous elastic limit and the subsequent relaxation follows the curve for instantaneous loading. For a relatively low loading rate, however, the peak force is lower than the instantaneous elastic limit but higher than the force corresponding to the same time (t^*) for the instantaneous loading. In other words, the indentation force overshoots the baseline curve for an infinite loading rate. This may be understood intuitively as a result of less solvent diffusion under the linear loading compared to the instantaneous loading over the same period of time. Consequently, the transient indentation force relaxation curve in general depends on the loading rate, while approaching the same equilibrium state eventually. Hence, in order to determine the elastic properties and solvent diffusivity of a hydrogel by the indentation relaxation measurements following the procedures described above, a sufficiently high loading rate should be imposed, e.g., $t^* / \tau < 10$, according to Fig. 5.8 for the plane-strain flat punch indentation.

5.3. SUMMARY

Numerical results are presented for flat-punch indentation of a hydrogel to validate the proposed finite element method proposed in Chapter 3 and further study the nonlinear response of hydrogels to indentation. For plane strain flat-punch indentation of hydrogels, the transient relaxation is bound by two elastic limits. A penalty method is used for the indentation displacement boundary condition to ensure accurate numerical solution of the instantaneous response. It is found that the normalized indentation relaxation curve depends on the effective Poisson's ratio of the hydrogel, for the case of plane strain flat-punch indentation. Moreover, the effects of loading rate on indentation relaxation are discussed

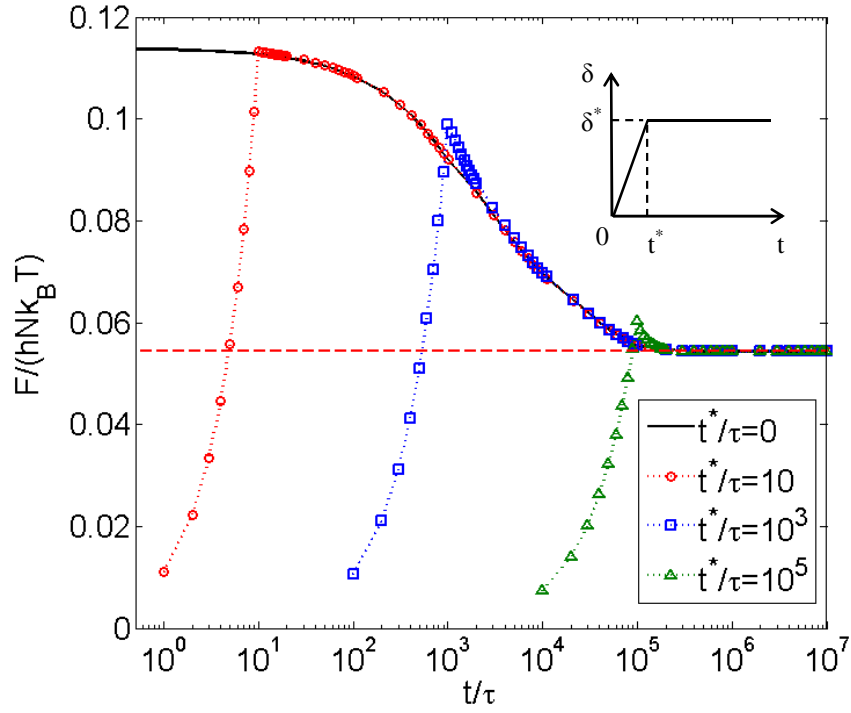


Figure 5.8: Effect of loading rate on indentation force relaxation. The inset shows the linear ramp of the indentation displacement with $\delta^*/h=0.1$. The horizontal dashed line corresponds to the equilibrium-state solution. Material parameters of the hydrogel are: $\chi=0.2$, $N\Omega=10^{-3}$, and $K=10^3 Nk_B T$; Half-width of the flat-punch indenter: $a/h=0.1$.

Chapter 6

Effect of Diffusion on Hydrogel Fracture

Structural integrity of hydrogels used in modern applications as load bearing components is of critical importance due to the fact that they are inherently soft materials with low fracture toughness, defining whether hydrogels can indeed be used in such applications (Nowak et al. 2002, Drury et al. 2003, Luo et al. 2004, Suciu et al. 2004). The biointegrability of hydrogels allows them to be used in a variety of bioengineering applications (Jagur 2006) and often such issues appear. There has been a lot of work recently in trying to create stronger types of hydrogels that are less prone to failure, and some have been very successful, for example, the creation of double network hydrogels (Gong et al. 2003); or the use of self-healing hydrogels (Zhao 2014). Existence of macroscopic damage in form of cracks is what mainly defines failure in hydrogels, thus, it is critical to study hydrogel fracture in depth, and it is necessary to conduct a consistent study, taking into account all the thermodynamic forces that act on the material throughout the transient loading and relaxation process.

So far, fracture of hydrogels is mainly studied by considering the instantaneous response to loading and treating them as elastomers (Kwon et al. 2011) neglecting solvent migration. Some recent studies have considered the effect of solvent diffusion in hydrogel fracture (Baumberger et al. 2006, Wang et al. 2012b, Zhang et al. 2012) and either used the framework of poroelasticity (Rice et al. 1976, Bouklas et al. 2012, Hui et al. 2013) or the nonlinear theory proposed by Hong et al. (2008), to model such phenomena. Similar studies have been considered in the field of geomechanics using the theory of poroelasticity, mainly to study hydraulic fracture (Ruina 1978, Cheng et al. 1993), providing important insight to the problem of fracture of a poroelastic medium,

but without answering the question about transient energy release rate. In thermoelasticity and poroelasticity, where along with the mechanical field there exists diffusion which dissipates energy, there has been work on trying to obtain the energy release rate, through conservation laws that usually apply to equilibrium or steady state solutions of the boundary value problems that are studied (Wilson et al. 1978, Gurtin 1979, Kishimoto et al. 1980, Chien et al. 1996). In the field electro-chemo-mechanical solid state diffusion, relevant work has been done recently by Gao et al. 2013 for steady state and Haftbaradaran et al. 2014 for equilibrium conditions. For the study of quasi-static evolution of hydrogels, finite element methods have been developed (Hong et al. 2009, Kang et al. 2010a) and interesting phenomena have been studied (Kang et al. 2010b, Wu et al 2013). But for the study of the full transient response of hydrogels, transient finite element methods have been proposed recently (Lucantonio et al. 2012, Wang et al. 2012a, Toh et al. 2013, Bouklas et al. 2014).

In this chapter the authors are motivated by interesting phenomena that have been observed in hydrogel fracture, like delayed fracture (Bonn et al. 1998, Wang et al. 2012b) and stick-slip behavior in dynamic crack propagation (Tanaka et al. 2009, Liang et al. 2012) to study the fundamentals of poroelastic fracture. The main objective of this work is the consistent derivation of a conservation law that provides the energy release rate at any state of the transient relaxation, during hydrogel fracture. The derivation of a modified transient J-integral along with the nonlinear theory used to model the physical processes taking place in hydrogels and the use of a domain integral to calculate the surface part of the transient J-integral are presented in section 6.1. A material model with incompressible constituents and a kinetic law are assumed following, and a nonlinear finite element method based to the one presented in Chapter 3 are used. The numerical results are then discussed in section 6.2 and involve Mode I displacement controlled

loading simulations for center crack hydrogel models in generalized plane strain conditions that are either immersed or not immersed in solvent. Since hydrogels often fail at very large strains with respect to their initial state (Sun et al. 2012), a wide range of loading is studied, and models with a sharp crack and a rounded notch are considered and compared. A detailed description of solvent migration is also presented for the various boundary value problems that are solved to provide a better understanding of the transient procedure. Finally in section 6.3 the conclusions of this work along with the extension of the proposed methods to crack propagation in hydrogels and the necessary experimental studies are discussed.

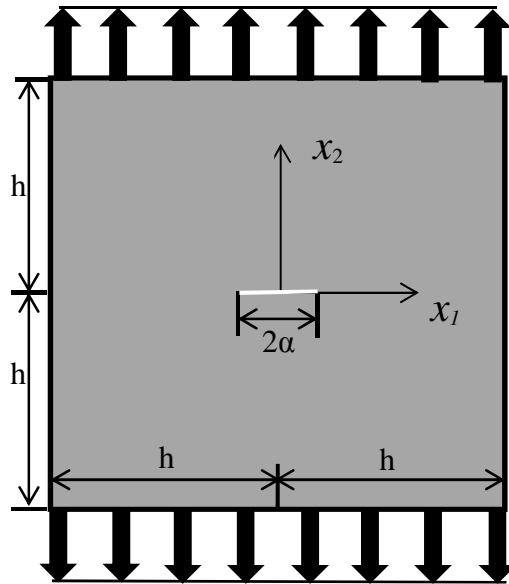


Figure 6.1. Center crack model in Mode I loading

6.1 GENERAL FORMULATION

6.1.1. A nonequilibrium thermodynamic approach

Hydrogels in their simplest form consist of two components, long crosslinked polymer chains that form a three dimensional network structure and small solvent molecules that can migrate within the network. The aggregate is then capable of large and reversible deformation subject to mechanical forces and/or environmental stimuli (e.g., humidity, temperature, etc). The nonlinear transient behavior of hydrogels with coupled deformation and diffusion has been studied by many (Tanaka et al. 1973; Dolbow et al. 2004; Hong et al., 2008; Duda et al. 2008; Doi 2009; Chester & Anand 2010; Wang et al. 2012a). The general formulation by Hong et al. (2008) is adopted in the present study.

The deformation of the aggregate can be traced by considering markers on the network with coordinates \mathbf{X} in a reference configuration, which is chosen to coincide with the dry state of the hydrogel. In the current configuration, the markers have coordinates \mathbf{x} , and the deformation is characterized by the deformation gradient tensor \mathbf{F} or $F_{ij} = \partial x_i / \partial X_j$ in Cartesian components. The nominal concentration of solvent molecules C is defined as the number of solvent molecules per unit volume of the polymer network. The free energy density is taken to be a function of the deformation gradient and the solvent concentration, $U(\mathbf{F}, C)$, which describes the constitutive behavior of the hydrogel. The nominal stress and the chemical potential are obtained as thermodynamic work conjugates by

$$s_{ij}(\mathbf{F}, C) = \frac{\partial U}{\partial F_{ij}} \quad (6.1)$$

$$\mu(\mathbf{F}, C) = \frac{\partial U}{\partial C} \quad (6.2)$$

Mechanical equilibrium is to be maintained at all time during the transient process so that

$$\frac{\partial s_{ij}}{\partial X_j} + b_i = 0 \text{ in } V_0 \quad (6.3)$$

$$s_{ij}N_j = T_i \text{ on } S_0 \quad (6.4)$$

where b_i is the nominal body force (per unit volume), V_0 and S_0 are the body and its boundary in the reference configuration, N_j is the outward unit normal on the surface of the reference configuration, and T_i is the nominal traction on the boundary.

Conservation of solvent molecules leads to a rate equation for the nominal concentration:

$$\frac{\partial C}{\partial t} + \frac{\partial J_k}{\partial X_k} = r \text{ in } V_0 \quad (6.5)$$

$$J_k N_k = -i \text{ on } S_0 \quad (6.5)$$

where J_k is the nominal flux of solvent, defined as the number of solvent molecules crossing unit reference area per unit time, r is a source term for the number of solvent molecules injected into unit reference volume per unit time, and i is the inward surface flux rate. The chemical boundary condition for the gel in general can be split into two regions, with specified solvent flux or chemical potential.

There are two ways to do work on the hydrogel aggregate. One is by the application of mechanical forces, including body forces and surface tractions. The second is the exchange of solvent molecules through the sources or the surface flux. Using the approach of nonequilibrium thermodynamics (Prigogine 1967; Coleman & Noll 1963), the potential energy of the aggregate system Π can be written as a sum of the internal stored energy and the work of the external mechanisms, and the rate of the potential energy is

$$\frac{d\Pi}{dt} = \int_{V_0} \frac{dU}{dt} dV - \int_{V_0} b_i \frac{dx_i}{dt} dV - \int_{S_0} T_i \frac{dx_i}{dt} dS - \int_{V_0} \mu r dV - \int_{S_0} \mu i dS \quad (6.7)$$

With Eqs. (6.1-6.6), the rate of the potential energy reduces to

$$\frac{d\Pi}{dt} = \int_{V_0} J_K \frac{\partial \mu}{\partial X_K} dV \quad (6.8)$$

Through an isothermal consideration the second law of thermodynamics dictates that the potential energy should never increase and hence

$$\frac{d\Pi}{dt} \leq 0 \quad (6.9)$$

For Eq. (6.9) to hold in any part of the body, it requires that

$$J_K \frac{\partial \mu}{\partial X_K} \leq 0 \text{ in } V_0 \quad (6.10)$$

This imposes a constraint on the kinetics relating the nominal flux to the gradient of chemical potential. A specific form of the kinetics is adopted for numerical simulations as described in Chapter 2.

By eq. (6.8), the change of the potential energy is related to the energy dissipation associated with solvent diffusion. Define the rate of energy dissipation as

$$\frac{d\Sigma}{dt} = - \int_{V_0} J_K \frac{\partial \mu}{\partial X_K} dV \quad (6.11)$$

In terms of the accumulative flux, $I_K = \int_0^t J_K dt$, the rate of energy dissipation can be written as

$$\frac{d\Sigma}{dt} = - \int_{V_0} \frac{\partial \mu}{\partial X_K} \frac{dI_K}{dt} dV \quad (6.12)$$

The total energy of the system can be defined as the sum of the potential energy and the energy dissipation due to solvent diffusion:

$$\Omega = \Pi + \Sigma \quad (6.13)$$

Considering the solvent diffusion as the only dissipative process, the total energy in Eq. (6.13) is conserved throughout the transient stage, i.e., $d\Omega/dt = 0$. Equivalently, the variation of the total energy must vanish at any time, i.e.,

$$\delta\Omega = \int_{V_0} \left(\delta U - \frac{\partial\mu}{\partial X_K} \delta I_K - b_i \delta x_i - \mu r \delta t \right) dV - \int_{S_0} (T_i \delta x_i - \mu N_K \delta I_K) dS = 0 \quad (6.14)$$

6.1.2. Transient energy release rate

In this section we derive the energy release rate for quasistatic crack propagation in a hydrogel. Consider a hydrogel body that contains a crack of length a in the current configuration as shown in Figure 6.2a. In the corresponding reference configuration, the crack length is denoted \tilde{a} , $\tilde{\mathbf{X}}$ refers to a fixed coordinate system, and \mathbf{X} refers to a moving coordinate system with its origin at the crack tip. The two coordinate systems are set such that $X_1 = \tilde{X}_1 - \tilde{a}$ and $X_2 = \tilde{X}_2$. Growth of the crack in the hydrogel is accompanied by deformation of the polymer network and migration of the solvent molecules. As the crack grows, the potential energy of the system changes. Following Eq. (6.14), the rate of change of the total energy with respect to the crack length is

$$\frac{d\Omega}{d\tilde{a}} = \int_{V_0} \frac{dU}{d\tilde{a}} dV - \int_{S_0} s_{ij} N_j \frac{dx_i}{d\tilde{a}} dS + \int_{S_0} \mu N_K \frac{dI_K}{d\tilde{a}} dS - \int_{V_0} \frac{\partial\mu}{\partial X_K} \frac{dI_K}{d\tilde{a}} dV \quad (6.15)$$

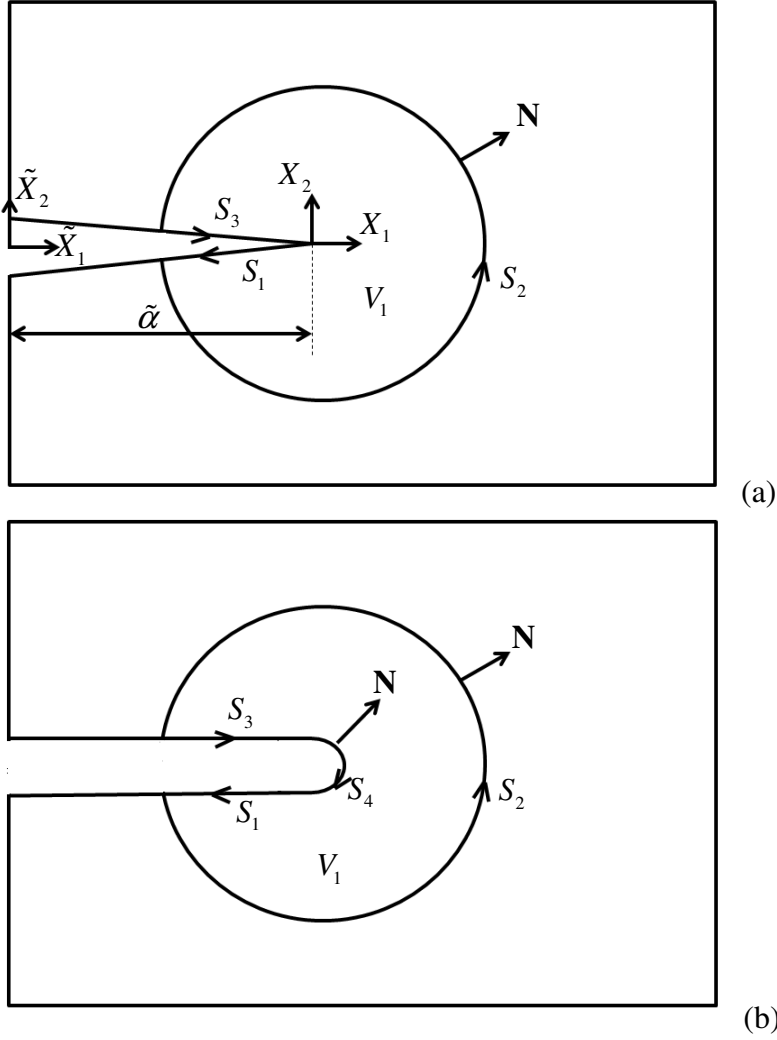


Figure 6.2: Schematic (a) of a body containing a sharp crack, and (b) of a body containing a rounded notch crack, both at the reference/dry configuration.

where the body force and solvent injection have been ignored. Eq. (6.15) gives the total energy change due to crack extension, which is separated from the energy dissipation due to diffusion by using the total energy Ω instead of the potential energy Π .

With respect to the moving coordinate \mathbf{X} , we have

$$\frac{d}{d\tilde{a}} = \frac{\partial}{\partial \tilde{a}} + \frac{\partial X_1}{\partial \tilde{a}} \frac{\partial}{\partial X_1} = \frac{\partial}{\partial \tilde{a}} - \frac{\partial}{\partial X_1} \quad (6.16)$$

Hence, the rate of the total energy change becomes

$$\begin{aligned} \frac{d\Omega}{d\tilde{a}} = & \int_{V_0} \left(\frac{\partial U}{\partial \tilde{a}} - \frac{\partial U}{\partial X_1} \right) dV - \int_{S_0} s_{ij} N_j \left(\frac{\partial x_i}{\partial \tilde{a}} - \frac{\partial x_i}{\partial X_1} \right) dS \\ & + \int_{S_0} \mu N_K \left(\frac{\partial I_K}{\partial \tilde{a}} - \frac{\partial I_K}{\partial X_1} \right) dS - \int_{V_0} \frac{\partial \mu}{\partial X_K} \left(\frac{\partial I_K}{\partial \tilde{a}} - \frac{\partial I_K}{\partial X_1} \right) \end{aligned} \quad (6.17)$$

Considering the first term on the right hand side of Eq. (6.17), with Eqs. (6.1-6.2), we obtain that

$$\int_{V_0} \frac{\partial U}{\partial \tilde{a}} dV = \int_{V_0} \left(s_{ij} \frac{\partial F_{ij}}{\partial \tilde{a}} + \mu \frac{\partial C}{\partial \tilde{a}} \right) dV \quad (6.18)$$

By integrating Eq. (6.5) over time with $r = 0$ (no solvent injection), the solvent concentration is obtained as

$$C - C_0 + \frac{\partial I_K}{\partial X_K} = 0 \quad (6.19)$$

where C_0 is the nominal concentration at the initial state of the hydrogel. The initial state of the hydrogel does not have to coincide with the dry state (reference). It is often taken as a free swollen state with a homogeneous solvent concentration and an isotropic deformation gradient, $F_{11} = F_{22} = F_{33} = \lambda_0$. With Eq. (6.19) and Eqs. (6.3-6.4), applying the divergence theorem, Eq. (6.18) becomes

$$\int_{V_0} \frac{\partial U}{\partial \tilde{a}} dV = \int_{S_0} \left(s_{ij} N_j \frac{\partial x_i}{\partial \tilde{a}} - \mu N_K \frac{\partial I_K}{\partial \tilde{a}} \right) dS + \int_{V_0} \frac{\partial \mu}{\partial X_K} \frac{\partial I_K}{\partial \tilde{a}} dV \quad (6.20)$$

Inserting Eq. (6.20) into Eq. (6.17), we obtain

$$-\frac{d\Omega}{d\tilde{a}} = \int_{V_0} \frac{\partial U}{\partial X_1} dV - \int_{S_0} s_{ij} N_j \frac{\partial x_i}{\partial X_1} dS + \int_{S_0} \mu N_K \frac{\partial I_K}{\partial X_1} dS - \int_{V_0} \frac{\partial \mu}{\partial X_K} \frac{\partial I_K}{\partial X_1} dV \quad (6.21)$$

Applying the divergence theorem to the first integral on the right hand side of Eq. (6.21), we obtain the transient J-integral as

$$J^* = -\frac{d\Omega}{d\tilde{a}} = \int_{S_0} \left(UN_1 - s_{ij}N_j \frac{\partial x_i}{\partial X_1} + \mu N_K \frac{\partial I_K}{\partial X_1} \right) dS - \int_{V_0} \frac{\partial \mu}{\partial X_K} \frac{\partial I_K}{\partial X_1} dV \quad (6.22)$$

A more convenient form of the J-integral is obtained by combining the flux terms with Eq. (6.19) so that

$$J^* = \int_{S_0} \left(UN_1 - s_{ij}N_j \frac{\partial x_i}{\partial X_1} \right) dS - \int_{V_0} \mu \frac{\partial C}{\partial X_1} dV \quad (6.23)$$

where the initial solvent concentration has been assumed to be homogeneous. It can be shown that, for a simply connected domain without singularities, the J-integral is necessarily zero by the mechanical equilibrium and mass conservation conditions in Eqs. (6.1-6.6). For a domain containing a crack tip, the transient J-integral is path-independent, giving the energy release rate for the crack growth.

Alternatively, by using the Legendre transform of the free energy function

$$\hat{U}(\mathbf{F}, \mu) = U(\mathbf{F}, C) - \mu C \quad (6.24)$$

the transient J-integral can be re-written as

$$J^* = \int_{S_0} \left(\hat{U}N_1 - s_{ij}N_j \frac{\partial x_i}{\partial X_1} \right) dS + \int_{V_0} \frac{\partial \mu}{\partial X_1} C dV \quad (6.25)$$

which will be used for the rest of this study. The form of the J-integral in Eq. (6.25) is preferable for numerical calculations in the finite element framework, as it does not include derivatives of the nominal concentration, which would usually require higher order interpolations (Wang et al 2012a, Bouklas et al. 2014).

We note that the transient J-integral has two parts, a surface integral, similar to the classic definition of J-integral (Rice 1968a), and in addition, a volume integral containing the gradient of the chemical potential and the concentration. The volume integral is not expected to pose any difficulties for numerical calculation, as the integral remains finite at the crack tip. This form of J-integral is similar to the cases with solid state diffusion, for which Gao and Zhou (2013) considered steady state fracture and Haftbaradaran and Qu (2014) derived a path-independent integral in the equilibrium state. Similar integrals were also used for thermoelasticity and poroelasticity (Kishimoto et al. 1980). We note that, by using the Legendre transform of the free energy function, the volume integral in Eq. (6.25) vanishes in the equilibrium state (constant μ). However, using the original free energy function, the volume integral in Eq. (6.23) remains unless $\mu = 0$.

The transient J-integral could be used to calculate the energy release rate for a sharp crack model (Figure 6.2a) using a contour around the crack tip (Rice 1968a). In a blunt crack model (Rice 1968b) with a rounded notch at the crack tip (Figure 6.2b), the integral has to be modified to account for the initial free energy at the notch, as further discussed in Section 6.2.2.

6.1.3. Domain integral method

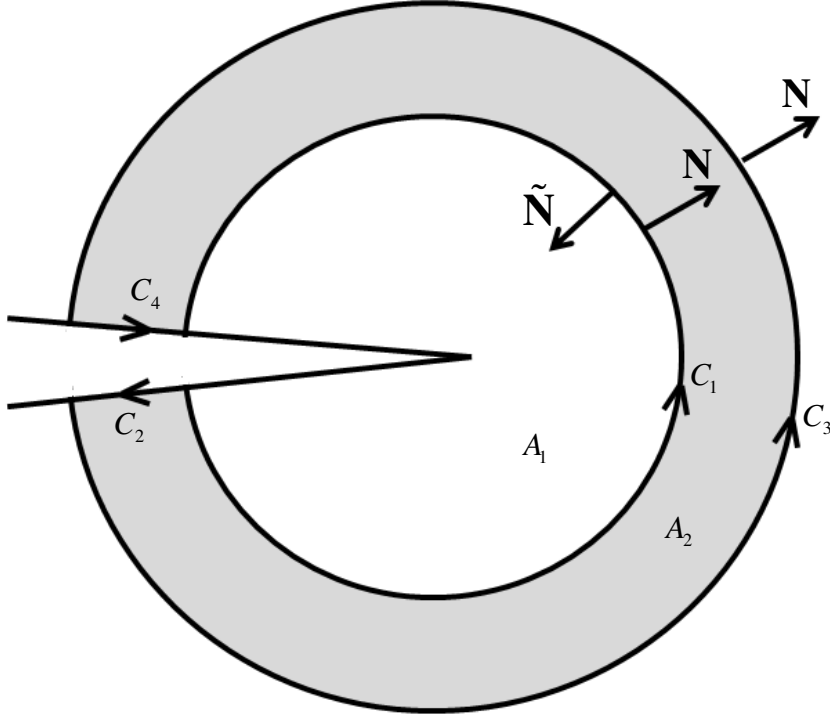


Figure 6.3: Simply connected region A_2 enclosed by contour $C = C_4 - C_1 + C_2 + C_3$.

For an accurate calculation of the standard J-integral (Rice 1968a) by the finite element method, it is advantageous to convert the surface integral to a volume integral. This procedure is known as the domain integral method. The approach of Li et al. (1985) is adopted in the present study for a two-dimensional case to convert the contour integral into a domain integral to calculate the transient energy release rate for quasi-static crack propagation in hydrogels. Considering the two-dimensional case of an annular region in a body, as shown in Figure 6.3, the energy release rate for a sharp crack can be obtained from the J-integral with the contour C_1 and the enclosed domain A_1 as

$$J^* = \int_{C_1} \left(\hat{U}N_1 - s_{ij}N_j \frac{\partial x_i}{\partial X_1} \right) d\Gamma + \int_{A_1} \frac{\partial \mu}{\partial X_1} CdA \quad (6.26)$$

Now consider a closed contour $C = C_4 - C_1 + C_2 + C_3$ bounding the area A_2 . Denote $\tilde{\mathbf{N}}$ as the outward normal on C with respect to A_2 , which coincides with \mathbf{N} on C_3 , but is opposite to \mathbf{N} on C_1 . The J-integral in Eq. (6.26) can then be re-written with a closed contour integral as

$$J^* = -\oint_C \left(\hat{U} \tilde{N}_1 - s_{ij} \tilde{N}_j \frac{\partial x_i}{\partial X_1} \right) q d\Gamma + \int_{A_1} \frac{\partial \mu}{\partial X_1} C dA \quad (6.27)$$

where q is a sufficiently smooth function in A_2 , varying from unity on C_1 to zero on C_3 . In addition, we set $q = 1$ in A_1 . Note that the contour integrals along the crack faces (C_2 and C_4) vanishes because they are assumed to be traction free and $N_1 = 0$. Since the area A_2 does not include any singularities and is simply connected, we apply the divergence theorem on the closed contour integral in Eq. (6.27) and obtained that

$$J^* = -\int_{A_2} \left[\hat{U} q_{,1} - s_{ij} x_{i,1} q_{,j} \right] dA + \int_{A_1+A_2} C \frac{\partial \mu}{\partial X_1} q dA \quad (6.28)$$

which is similar to the domain integral obtained by Li et al. (1985) but includes an additional term associated with the solvent. We note that the additional term vanishes when the hydrogel reaches chemical equilibrium with a constant chemical potential or when $C = 0$ for the dry state. As will be shown in Section 6.2, the domain integral in Eq. (6.28) is convenient for numerical calculations using the finite element method.

6.2. NUMERICAL RESULTS

In this section the focus will be Mode I displacement controlled loading of center crack hydrogel models (Figure 6.1), in generalized plane strain conditions, that are either immersed in solvent, or not-immersed and isolated from the environment. The material

model for a hydrogel with incompressible constituents presented in Chapter 3 and the equivalent mixed finite element method will be employed in the numerical simulations.

Two variations of a two-dimensional finite element mesh, will be used to simulate the hydrogel model for the rectangular domain. Only a quarter (Figure 6.1) of the domain is modeled, invoking the symmetry of the model. The crack length is $2a$ and the height and width of the full rectangular domain are $2h$. The first mesh, features a sharp crack geometry (Figure 6.4a), using 8u4p Taylor-Hood elements for the majority of the model, with the exception of the crack tip where collapsed quarter point 6u3p Taylor-Hood elements are used. In this model, the mesh features concentric rings of elements around the crack tip. The second model, features a rounded notch at the crack tip (Figure 4b), that is used in order to accommodate large far-field deformations with respect to the initial state, and uses 8u4p Taylor-Hood elements throughout. In this section, the first model will be used for loading conditions that cause small, and moderately large far-field deformations, and the second model for moderately large, and large far-field deformations. The two models will be compared for moderately large far-field deformations. The small deformation results will be compared through the linearization procedure of Bouklas and Huang (2012) presented in Chapter 2 to results from linear elastic fracture mechanics (Broberg, 1999).

At the initial state, hydrogels will be considered at a homogeneous, fully swollen, stress-free state, and at equilibrium; characterized by a homogeneous swelling ratio λ_0 corresponding to an initial chemical potential, $\mu_0 = 0$, which can be determined analytically similarly to Chapter 2. Relative to the dry state, the initial displacement is: $\mathbf{u}_0 = \lambda_0 \mathbf{X} - \mathbf{X}$. The center of the crack is used as the origin of the coordinate system, and coordinate X_1 is set as the crack direction.

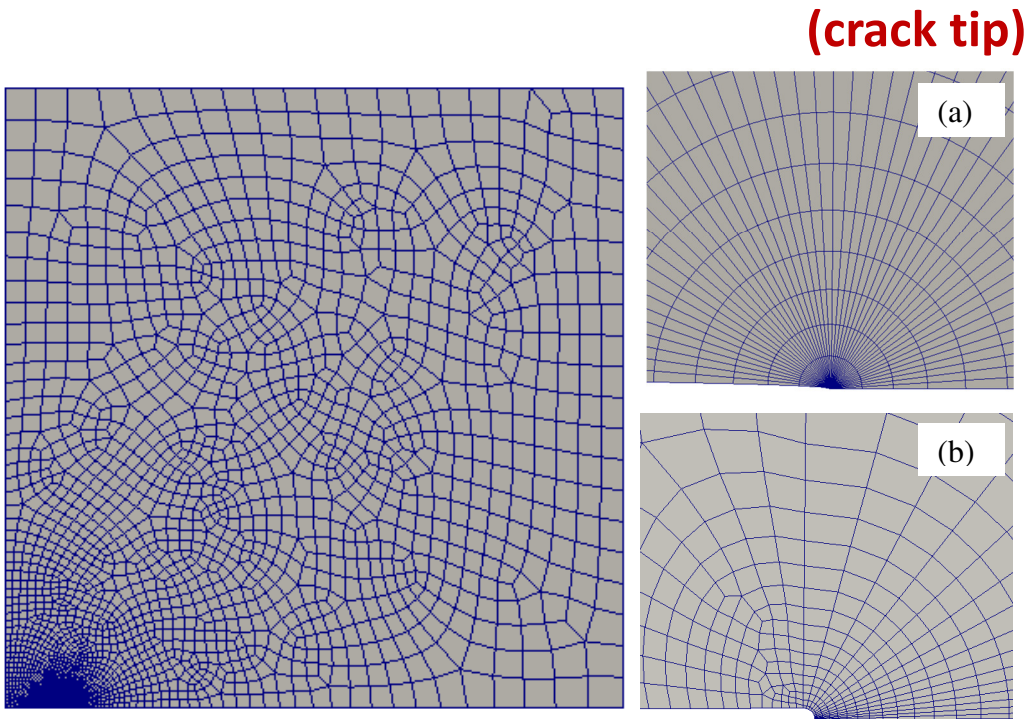


Figure 6.4: Mesh for one quartet of the domain. (a) For the sharp crack model, Taylor-Hood 8u-4p quadrilateral elements used everywhere except for the crack tip, where 50 quartet point Taylor-Hood 6u-3p elements are used. (b) Mesh for notched specimen. Taylor-Hood 8u-4p quadrilateral elements are used. The radius of the notch is taken to be three orders of magnitude smaller the crack length $r_n / \alpha = 10^{-3}$ to study very large deformations with respect to the initial state.

Symmetry boundary conditions are imposed as no displacement relative to the initial state and no flux, following $\Delta u_1|_{X_1=0} = 0$, $J_1|_{X_1=0} = 0$ and $\Delta u_2|_{X_2=0, X_1 \geq \tilde{a}} = 0$, $J_2|_{X_2=0, X_1 \geq \tilde{a}} = 0$, where the change of displacement with respect to the initial state is denoted as $\Delta \mathbf{u} = \mathbf{u} - \mathbf{u}_0$, and $2\tilde{a}$ the dry crack length (noting $a = \lambda_0 \tilde{a}$). Loading is applied through a displacement boundary condition to the top surface $\Delta u_2|_{X_2=H} = \overline{\Delta u_2}$, where the dry thickness of the hydrogel is $2H$ (noting $h = \lambda_0 H$). The crack face and the unloaded far-field boundary at $X_1 = H$ are traction free $T_i = 0$. In the case of a hydrogel immersed in solvent, the crack face and the outer surfaces of the model are in equilibrium with the environment by setting $\mu|_{X_2=0, X_1 \leq \tilde{a}} = 0$, $\mu|_{X_1=H} = 0$ and $\mu|_{X_2=H} = 0$. Otherwise if the hydrogel is not immersed in solvent, no flux boundary conditions are enforced on the crack face $J_2|_{X_2=0, X_1 \leq \tilde{a}} = 0$ and the outer boundaries $J_1|_{X_1=H} = 0$, $J_2|_{X_2=H} = 0$ of the model following (Wang et al. 2012b). For convenience, dimensionless quantities are used as follows: all lengths are normalized by the crack length (a), time is normalized by the characteristic diffusion time, $\tau = \alpha^2 / D$, stresses are normalized by $Nk_B T$, chemical potential by $k_B T$, and solvent concentration by Ω^{-1} .

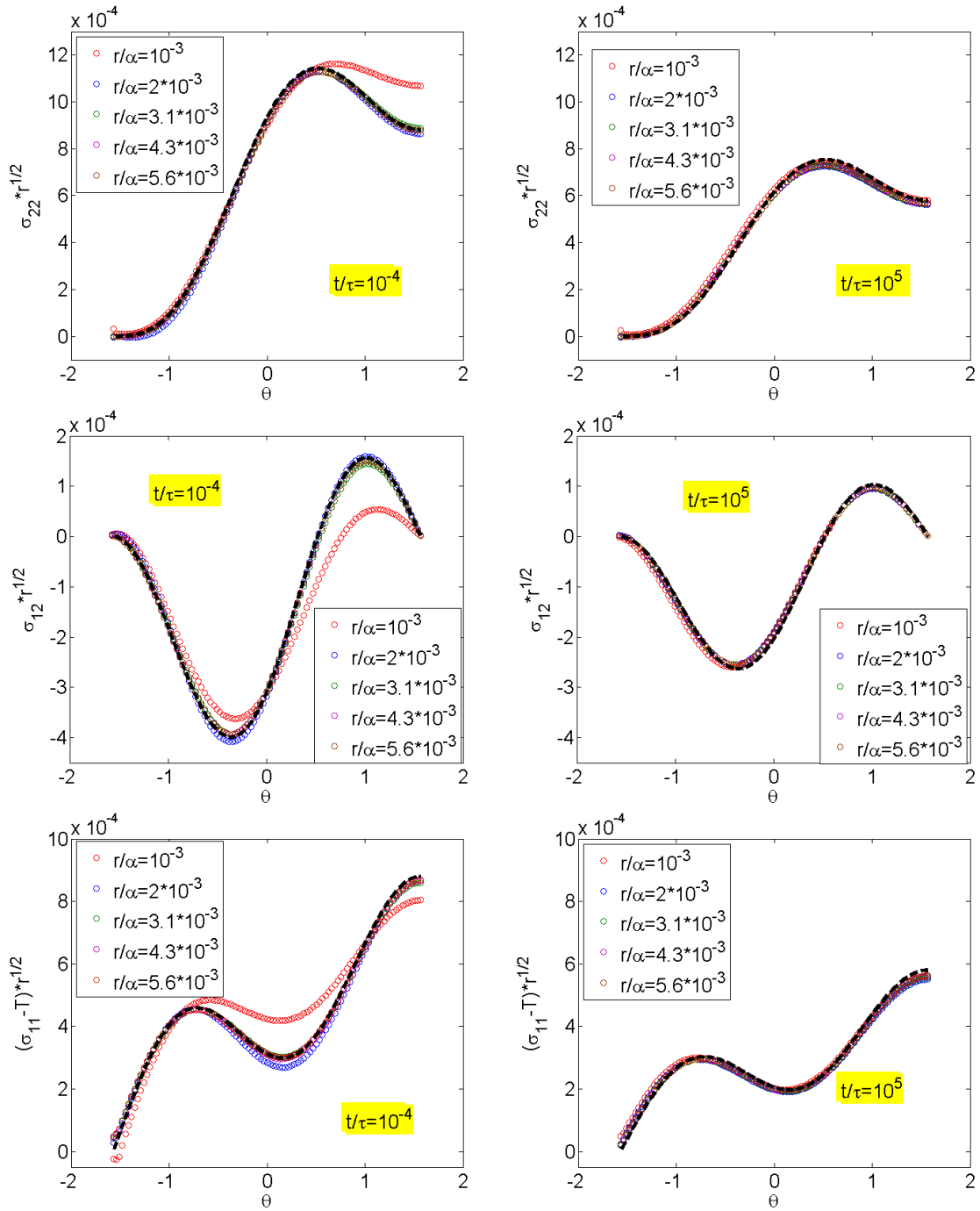


Figure 6.5: Immersed center crack specimen in Mode I loading. Cauchy stress distribution for the instantaneous response and at equilibrium for rings of nodes with an increasing distance from the tip,. Dashed lines are obtained from the linear elastic solution.

6.2.1. Sharp crack model

6.2.1.1. Small far-field deformations

The first simulations using the sharp crack geometry, involve small far field deformations and use a ratio between the crack length and domain thickness $h/\alpha=10$. The values for the combined material parameters that are used throughout this section (unless otherwise noted) are: $N\Omega=10^{-3}$ and $\chi=0.2$, giving an initial swelling ratio of $\lambda_0=3.215$. A way to quantify the averaged deformation is to approximate the far-field strain in the loading direction as $\epsilon^\infty = [h(t)-h(0)]/h(0)$, where $2h(t)$ is the thickness of the hydrogel in the x_2 direction as a function of time; when the time is not specified, we will be referring to the initial value of the thickness.

For the simulation related to Figure 6.5, an immersed center crack hydrogel model is subject to displacement loading, applied through the boundary condition $\Delta u_2|_{x_2=H} = 10^{-2}\alpha$ leading to far field strain equal to $\epsilon^\infty = 10^{-3}$. To examine the nature of the singularity at the crack tip, the Cauchy stress $\sigma_{ij} = s_{iK}J_{jK} / \det(\mathbf{F})$ is plotted at rings of nodes with increasing distance from the tip, at the instantaneous state $t=10^{-4}$, (right after loading is applied) capturing the incompressible response of the hydrogel, and after the poroelastic relaxation,, at the equilibrium state $t=10^5$. The results are normalized by multiplying the stresses with the square root of the distance of the rings from the tip as $\sigma_{ij}\sqrt{r} / Nk_B T$ and plotted as a function of the angle defined positive clockwise from the axis starting from the crack tip and parallel to X_2 . After such a normalization, the results from the different rings overlap, leading to the fact there is a square root singularity at the crack tip field as expected for small deformations .

It should be noted that a T-stress appears in the σ_{11} stress component, as the loading is uniaxial. The magnitude of the T-stress related to the far field stress as $T = -\sigma^\infty$. The far-field stress can be calculated using the plane strain Young's modulus

and the far field strain as $\sigma^\infty = E^* \varepsilon^\infty$. The plane strain Young's modulus is defined as $E^* = E/(1-\nu^2)$, where $E = 2G_0(1+\nu)$. The effective shear modulus based on the linearized results from (Bouklas and Huang, 2012) can be defined for a homogeneously swollen gel following Eq. (A.18) while the effective Poisson's ratio is 0.5 (incompressible) for the instantaneous response and is less than 0.5 for the equilibrium response. The equilibrium Poisson's ratio is related to the intrinsic properties of the hydrogel by Eq. (A.8)

Thus leading to an instantaneous and an equilibrium value for the T-stress that are used in the normalization of the results as $(\sigma_{12} - T)\sqrt{r} / Nk_B T$. The collapsed results are then compared to the linear elastic solution for the crack tip stress field obtained from

$$\sigma_{ij} = \frac{K^I}{2\pi r} f_{ij}^I(\theta) \quad (6.29)$$

where K^I is the stress intensity factor for Mode I loading. For an infinite domain, it is defined as a function of the far-field stress and the crack length as

$$K^I = \sigma^\infty \sqrt{\pi\alpha} \quad (6.30)$$

and the functions of radial position are known to be

$$\begin{aligned} f_{11}^I &= \cos\frac{\theta}{2} \left(1 - \sin\frac{\theta}{2} \sin\frac{3\theta}{2} \right) \\ f_{12}^I &= \cos\frac{\theta}{2} \sin\frac{\theta}{2} \cos\frac{3\theta}{2} \\ f_{22}^I &= \cos\frac{\theta}{2} \left(1 + \sin\frac{\theta}{2} \sin\frac{3\theta}{2} \right) \end{aligned} \quad (6.31)$$

It is noted that for immersed swelling, the instantaneous and the equilibrium results have to be compared to two sets of linear solutions, resulting from the fact that Poisson's ratio changes from $\nu_0 = 0.5$, to the equilibrium value $\nu_\infty = 0.2415$ (specific to the material parameters in this simulation). The comparison to the linear results is satisfactory, where the linear elastic solution is plotted with a dashed line in Figure 6.5. Stress relaxation from solvent redistribution leads to lower stress values at the equilibrium state. One detail to note, is that the results from the first ring of nodes, that belong to the collapsed, quartet-point, 6u3p elements slightly deviate from the rest of the results, for the instantaneous case. This can be attributed to the fact, that at the instantaneous limit, as discussed in Chapter 2, the chemical potential on the boundary is discontinuous from the value in the volume, creating a sharp gradient, that cannot be resolved, not even with mesh refinement, and causes mild oscillation of the numerical results close to the boundary. The oscillations dissipate over time. One possible way to avoid this, is by introducing, physical or numerical viscosity (Wang et al. 2012b), where an additional timescale associated with the viscous process has to be defined.

With the same normalization procedure, the results from a not-immersed hydrogel model loaded to the same level of far-field strain $\varepsilon^\infty = 10^{-3}$ are presented in Figure 6.6, linear elastic solutions are again plotted with a dashed line. To point out the difference between immersed and not-immersed cases, first the evolution process in each will be described. In the immersed case, before loading everything is in equilibrium. When loading is applied, the chemical potential drops globally. Following, solvent enters through the external and crack face boundaries, and solvent is redistributed in the domain. The total volume is not conserved in this process. Whereas in the not-immersed case, following loading, the solvent redistributes locally close to the crack tip, but the total volume is

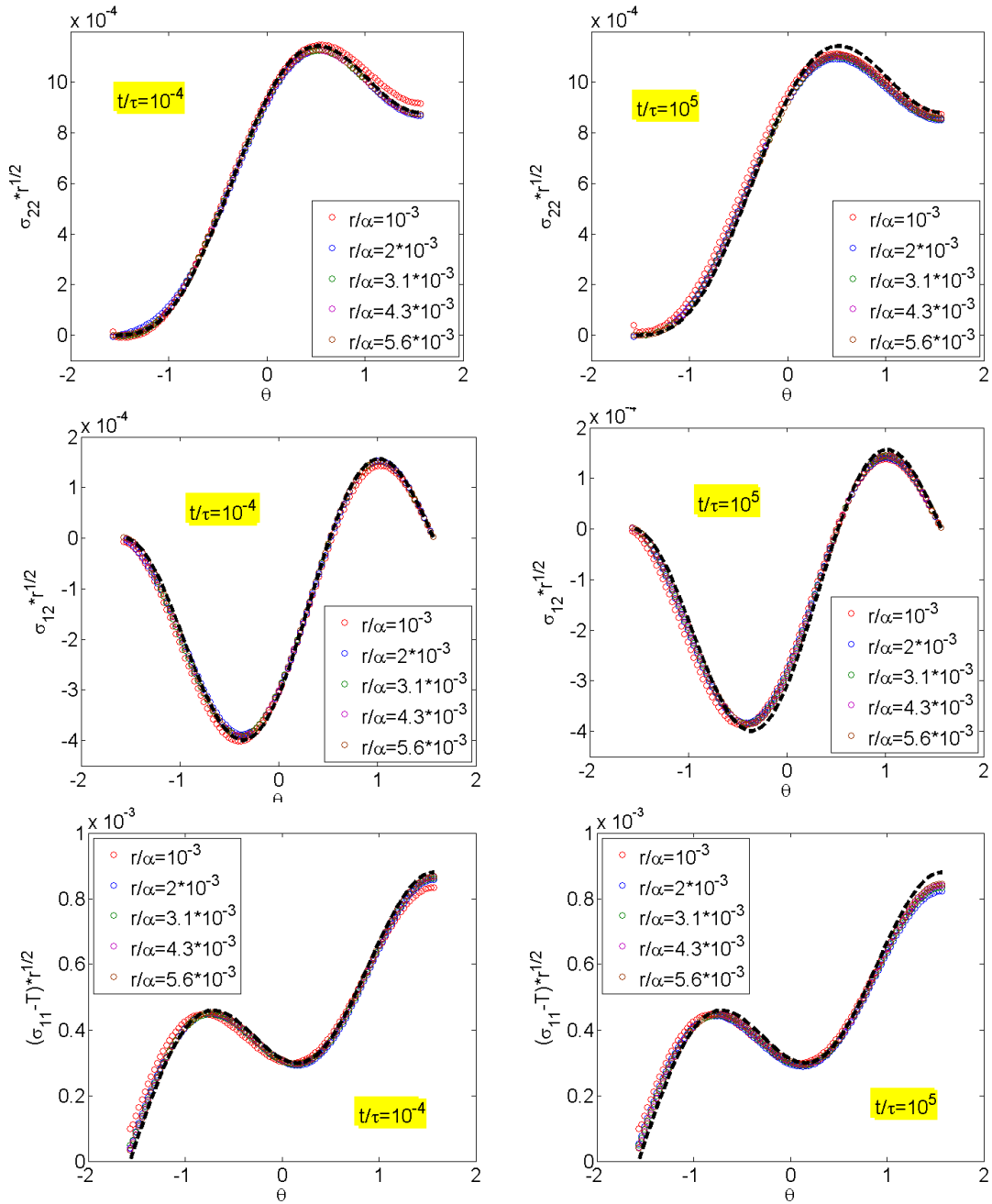


Figure 6.6: Not-immersed center crack specimen in Mode I loading. Cauchy stress distribution for the instantaneous response and at equilibrium for rings of nodes with an increasing distance from the tip Dashed lines are obtained from the linear elastic solution.

conserved and there is minimal solvent migration in the far field. Thus, the not-immersed process can be approximated, using the incompressible value for Poisson's ratio 0.5 for both the instantaneous and the equilibrium response.

The approximation at equilibrium will not be as accurate as the approximation of the instantaneous response, due to the local redistribution of solvent. Thus, the linear solutions that are plotted for the two limits are identical, and there is good agreement with the numerical results. The value of the T-stress is also taken as constant for the instantaneous and equilibrium responses. The relaxation observed is minimal, compared to the immersed case, and as pointed out it occurs due to the local redistribution of the solvent around the tip. In this case, even for the instantaneous solution, the results from all of the rings, including the first ring of elements, collapse more accurately than in the immersed case, confirming the boundary effect discussed previously.

In the same simulations, where $\epsilon^\infty = 10^{-3}$, the chemical potential in the immersed and not-immersed cases evolves in a different fashion. If the symmetry plane ahead of the crack tip is examined, in the immersed case, the value of the chemical potential starts from zero at the crack tip, and after loading, drops to a lower value ahead of the crack tip and increases monotonically after that. At equilibrium, the chemical potential reaches zero everywhere in the domain. This result is plotted in the top part of Figure 6.7. The shape of this curve, gives important information regarding the flux in the direction of the crack, as it can be obtained from the gradient of the chemical potential. Thus, it is pointed out, that the solvent mainly migrates towards the point ahead of the crack tip where chemical potential has reached a minimum.

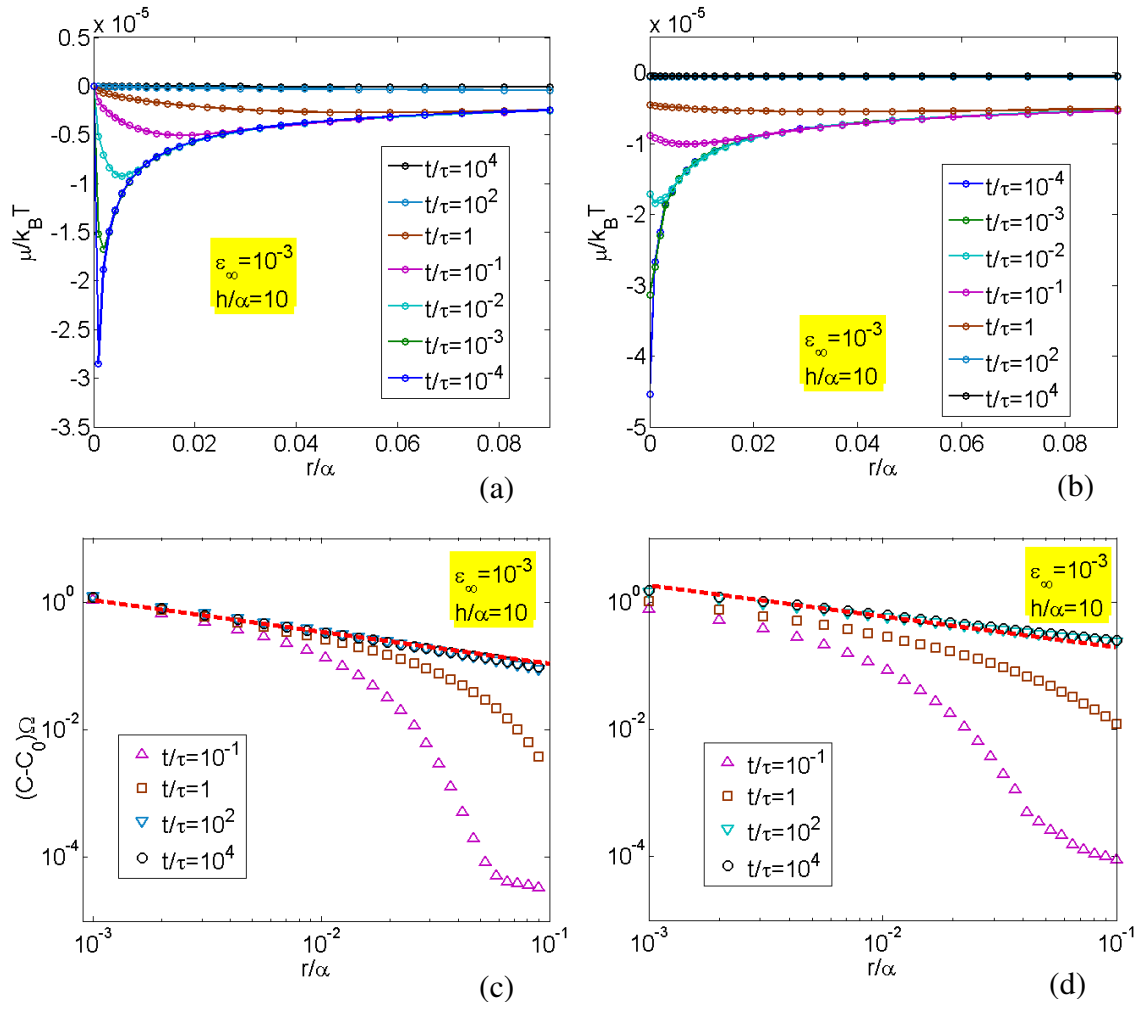


Figure 6.7: Evolution of the chemical potential (a,b) and concentration fields (c,d) ahead of the crack tip for the immersed (a,c) and the not-immersed (b,d) cases, where the dashed line is square root singular.

In the not-immersed case, the value of the chemical potential at the crack tip is not fixed, and at the early stages of evolution it has the minimum chemical potential value, and solvent migrates towards that location. At equilibrium, chemical potential assumes a value lower than zero throughout the domain. At the instantaneous limit $t \rightarrow 0$, the chemical potential field close to the crack tip is plotted in Figure 6.8 for both the immersed and the not immersed cases. The difference for the location of the minimum chemical potential between the immersed and the not immersed model, is showcased in this plot. The fields are similar further away from the crack tip and the crack face. Another difference to note is the boundary condition, where in the not immersed case there is a no-flux condition in the crack face, whereas in the immersed the chemical potential is set to zero on the crack face creating a sharp change in the chemical potential distribution at the instantaneous response limit. As seen in these contour plots, instantaneously (and at the early stage of evolution), solvent tends to move from the area behind the crack tip to the area ahead of the crack tip.

The evolution of the concentration ahead of the crack tip is another interesting feature of this solution. The linearized volumetric strain about the initial state, for the instantaneous incompressible response is $\epsilon_{kk}^0 = 0$. As time evolves and solvent migrates in the region close to the crack tip, the linearized volumetric strain is expected to follow the behavior of the stress and become square root singular $\epsilon_{kk} \sim 1/\sqrt{r}$. The linearized volumetric strain is related to the determinant of the deformation gradient like $\epsilon_{kk} = \det(\mathbf{F}) - \det(\mathbf{F}^0)$, where $\det(\mathbf{F}^0)$ represent the value of the deformation gradient at the initial state. Using the incompressibility constraint from Eq. (3.4), the behavior of the

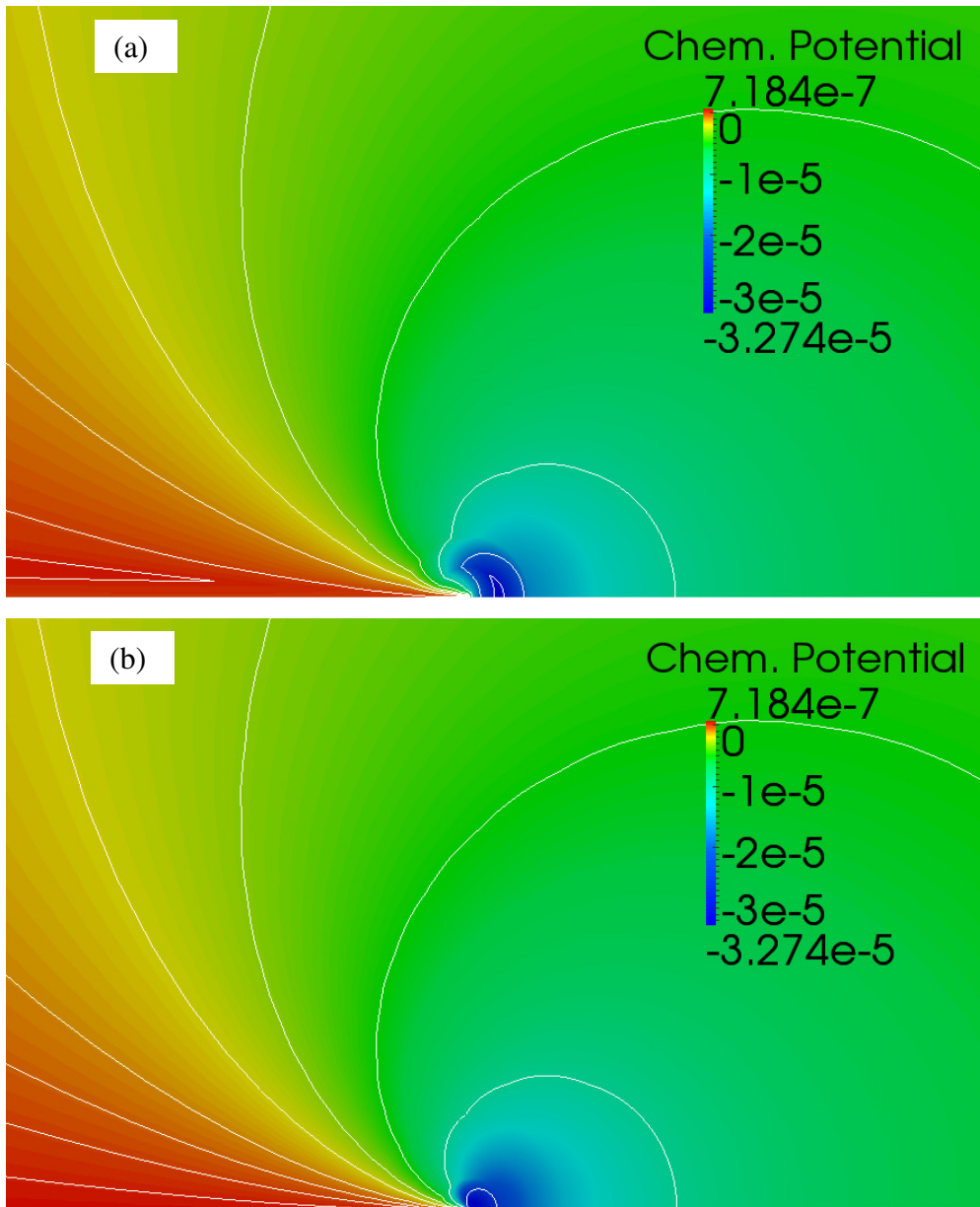


Figure 6.8: Chemical potential contours at the instantaneous response limit, showing the difference in the crack tip chemical potential field for (a) the immersed and (b) the not-immersed cases.

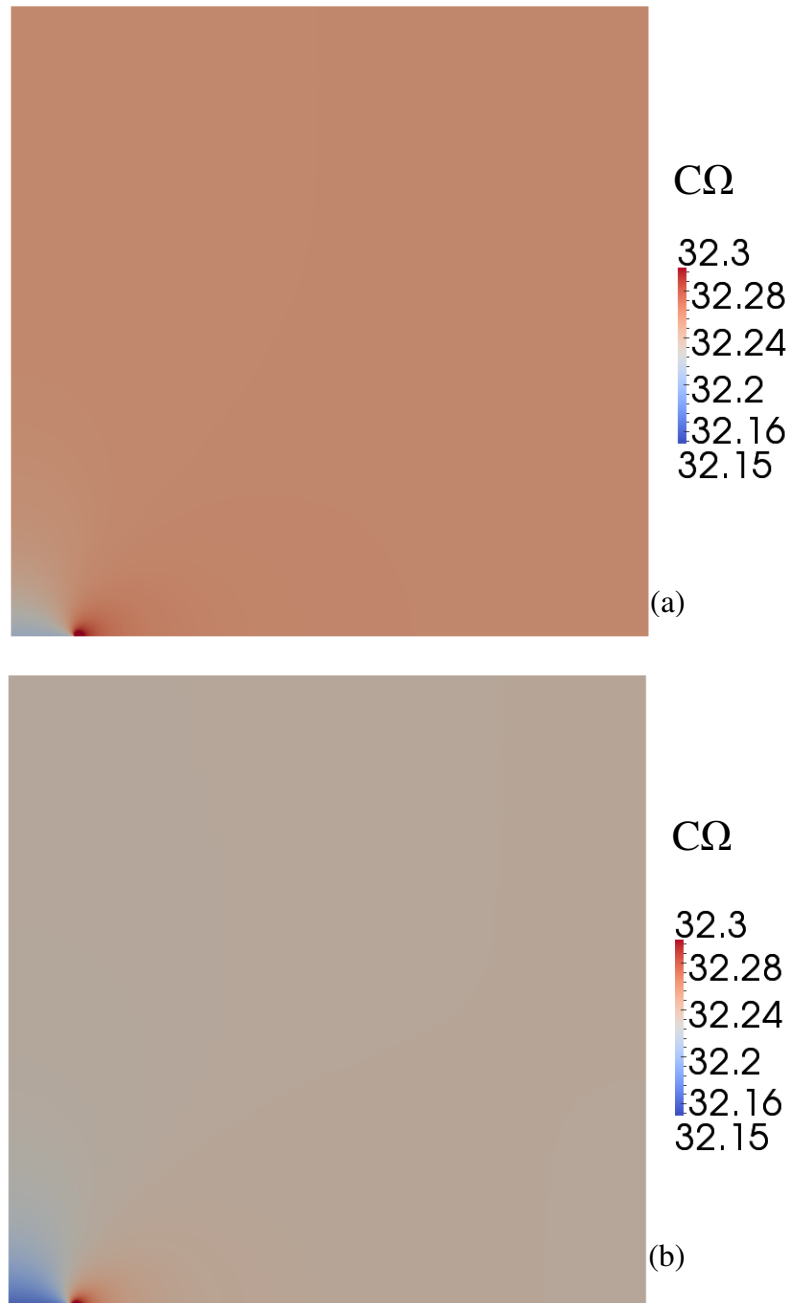


Figure 6.9: Normalized nominal concentration contours at the equilibrium response limit for the (a) immersed and (b) not immersed cases..

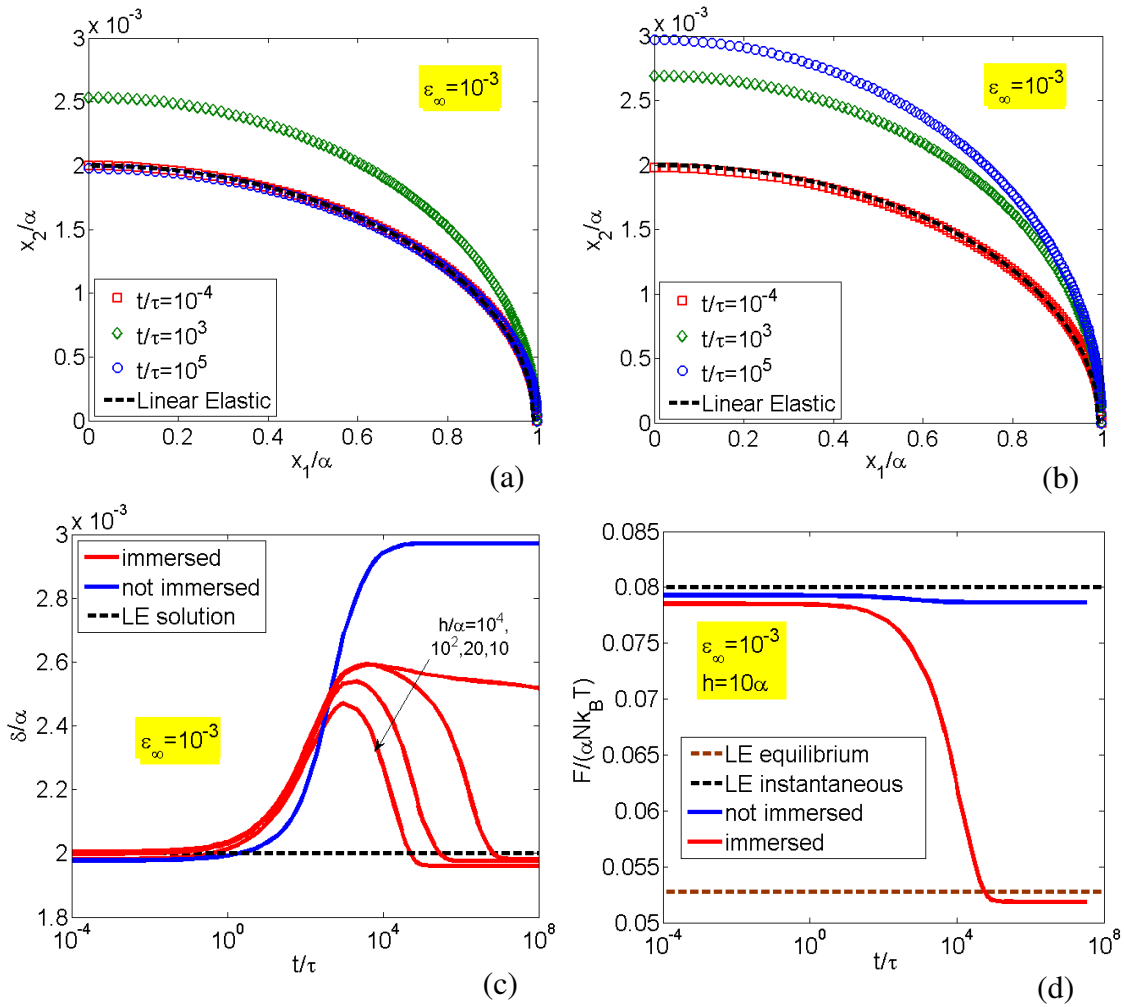


Figure 6.10: Crack opening displacement profile evolution for (a) immersed and (b) the not-immersed case. (c) Maximum crack opening displacement evolution for the two cases and a limiting behavior for the immersed case. (d) Evolution of the total force applied to a $h/a = 10$ model for far field strain $\epsilon_\infty = 10^{-3}$ for both the immersed and the not-immersed cases. Dashed lines are linear elastic solutions for all plots.

change of concentration around the crack tip is also expected to be square root singular $(C - C_0) \sim 1/\sqrt{r}$. In Figure 6.7, the change of concentration is plotted ahead of the crack tip as a function of the radius from the crack tip. The square root singular behavior is confirmed for both the immersed and the not immersed cases, as the hydrogel evolves towards equilibrium, where the dashed line is square root singular. At the instantaneous response limit, the change of concentration is zero, and as time progresses, the size of the region where the change of concentration assumes an approximately square root singular increases until equilibrium is achieved.

The concentration at equilibrium is plotted over the whole domain in Figure 6.9. Both the immersed and the not-immersed hydrogel model start from the same initial normalized concentration $C_0\Omega \approx 32.23$. In the immersed model, the total volume is not conserved, and at equilibrium, the concentration has risen moderately from its initial value in the bulk of the material, far from the tip. The concentration drops behind the crack tip and significantly rises ahead of the crack tip. On the contrary, in the not-immersed case, the total volume of the hydrogel is conserved. At equilibrium, away from the crack tip, where there are no stress concentrations, the concentration virtually remains unchanged. Closer to the crack tip, local redistribution of the solvent occurs, and the same behavior with the immersed case is observed, as predicted from Figure 6.8.

Next, the crack opening displacement profile evolution for the immersed and not immersed case is considered for $\varepsilon^\infty = 10^{-3}$. The instantaneous profile that is assumed at $t = 10^{-4}$, another at $t = 10^3$, and the equilibrium profile at $t = 10^5$ are shown in Figure 6.10(a,b). For the immersed case, an interesting behavior for the crack opening displacement is observed. Instantaneously, when the model is loaded, the crack assumes an opening profile, as the solvent migrates, the crack opens and then gradually closes and assumes a profile very close to the initial. The instantaneous and equilibrium profiles are

confirmed exhibit the same deformation, regardless of the change of Poisson's ratio, following the linear elastic solution given by

$$u_1(x_1, 0) = -\frac{4(1-\nu)}{G} \sigma^\infty x_1 = -8\varepsilon^\infty x_1 \quad (6.32)$$

$$u_2(x_1, 0) = \frac{(1-\nu)}{G} \sigma^\infty \sqrt{a^2 - x_1^2} = 2\varepsilon^\infty \sqrt{a^2 - x_1^2} \quad (6.33)$$

using the plane strain relationships that were discussed previously. The linear elastic solution is also plotted as a dashed line, and is in good agreement with the instantaneous and equilibrium solution for the immersed case. For the not immersed case, there is a monotonic behavior observed, where the crack profile keeps opening throughout the evolution, and the elastic solution only captures the instantaneous response. This is expected as in the not-immersed case, the solvent migrates locally due to the stress concentration at the tip and the linearized solution about the instantaneous incompressible homogeneous state cannot represent that local effect. On the other hand, in the immersed case the linearized solution about the equilibrated state capture the dominant effect of the solvent migration from the environment into the hydrogel. In Figure 6.10(c) the evolution of the maximum opening δ at the center of the crack, is evaluated for $\varepsilon^\infty = 10^{-3}$, for the immersed and the not-immersed cases. The opening-closing behavior of the immersed hydrogel model, versus the monotonic opening behavior of the not-immersed model are clearly visualized here. Also, a limiting behavior for peak of the immersed case is obtained by considering an increasing size for the rectangular domain, keeping the crack length fixed, as $h/a = 10, 20, 10^2, 10^4$. This limiting behavior is related to the local migration of solvent near the crack tip with respect to the far-field boundary solvent migration.

Another way to track the intensity of the relaxation procedure from the immersed and not-immersed cases, resulting from displacement controlled mode I loading, is to track the resultant force, applied at the top boundary of the domain. This is an interesting quantity as it could easily be measured experimentally. In Figure 6.10(d) the resultant force in the x_2 direction is plotted for the same simulation, with $\varepsilon^\infty = 10^{-3}$, and $h/a = 10$. The magnitude of the force relaxation for the immersed case is much larger than for the not-immersed case. The force per unit length in the out of plane direction, can be captured for both cases at the instantaneous linear elastic limit using the far-field stress σ^∞ for Poisson's ratio $\nu_0 = 0.5$, and at the equilibrium limit the immersed case can be captured using $\nu_\infty = 0.2415$ for the far-field stress. The small difference from the linear solution is attributed to the finite size of the domain and the comparable crack/thickness dimensions. The difference at the instantaneous limit between the immersed and not-immersed cases is attributed to the instantaneous relaxation due to the $\mu = 0$ boundary condition applied in the immersed case on the loading boundary, as discussed for hydrogel swelling in (Bouklas and Huang, 2012).

For this study of mode I displacement controlled loading, the energy release rate will be calculated from the modified transient J-integral formula from Eq. (6.25). In order to prove path independence for the transient J-integral at any state of the evolution process, it will be calculated for circular domains of increasing area, that consecutively include additional rings of elements with increasing radii from the crack tip. For the complete calculation of the transient J- integral in this two-dimensional calculation, an area integral will have to be calculated, and also a contour integral calculated with the help of Eq. (6.28) using the domain integral method. A linearly varying parameter q will be used in Eq. (6.28). The crack faces will not have a contribution to the contour integral

of Eq. (6.25). In Figure 6.11 (a), the values of the transient J-integral for an immersed specimen are plotted as a function of the radii of the circular regions they correspond to. Also, three different times are considered $t = 10^{-4}, 10^3, 10^5$, confirming path independence throughout the relaxation process. The parameters, size of the domain and loading, are the same as the ones used previously. The classic definition of the J-integral (Rice 1968a) is not meaningful in the poroelastic model, as it does not provide the energy release rate, and also it is expected to be path-dependent. Path-dependence can be confirmed by calculating the classic J-integral using the following definition

$$J = \int \left(\hat{U} N_1 - s_{ij} N_j \frac{\partial x_i}{\partial X_1} \right) dS \quad (6.34)$$

where the domain integral method can still be applied. In Figure 6.11(b) path-dependence is confirmed for the classic J-integral used in a poroelastic medium, as the values obtained at $t = 10^3$ vary significantly as the radius of the domain increases. It is noted though that instantaneously and at equilibrium, the results seem to imply path-independence at those states. Whether the Legendre transformed free energy density \hat{U} or free energy density U is used in Eq. (6.34), the classic J-integral is expected to remain path-dependent. The value of the J-integral has been normalized by $(aNk_B T)$.

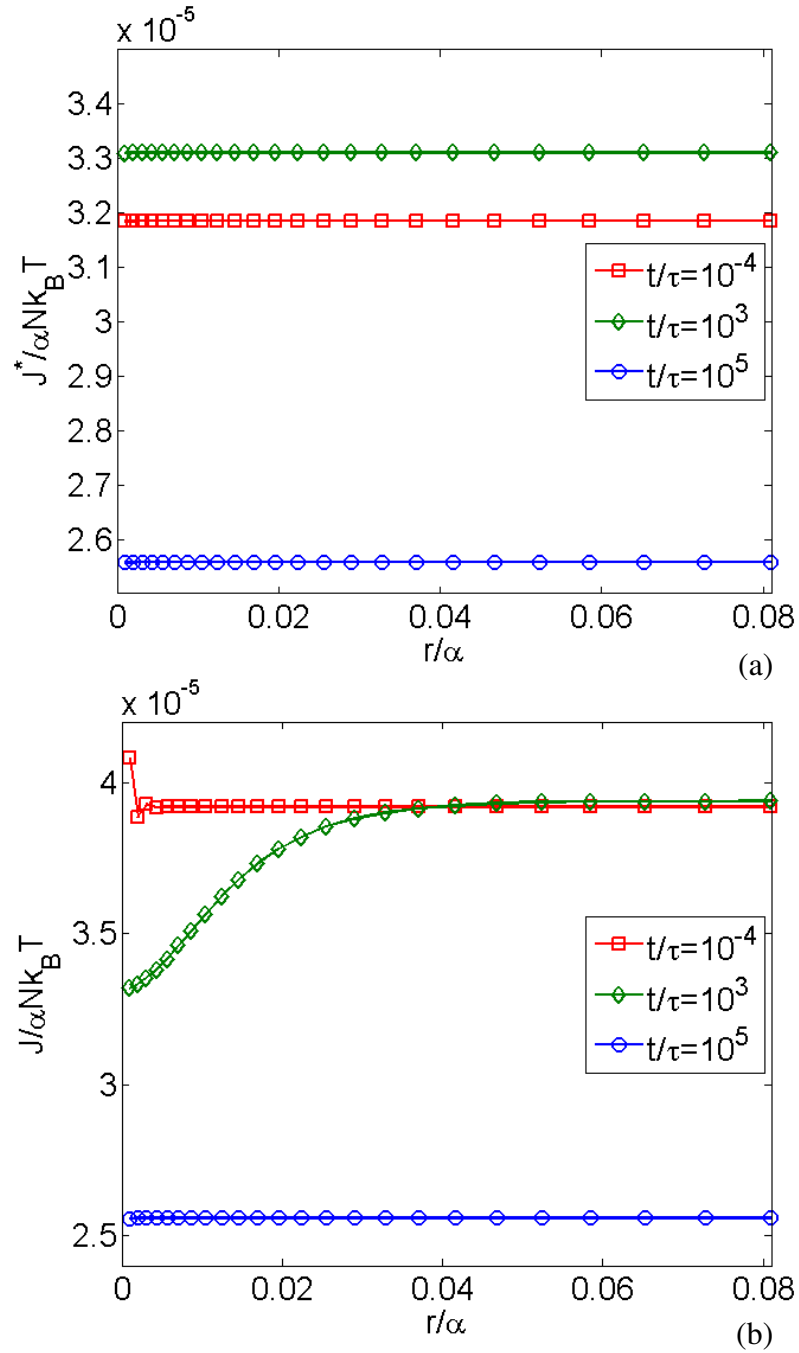


Figure 6.11: (a) transient J integral values for paths at different radial distances from the crack tip and at different times, showing path independence for the integral we have defined here, (b) path dependence for classical definition of the J integral if used in a poroelastic system.

In Figure 6.12, the transient J-integral evolution, is first plotted for small far-field deformations $\epsilon^\infty = 10^{-3}$, and $h/a=10$, for both the immersed and the not immersed case. A behavior that follows the maximum crack opening displacement is observed for both cases. For the not immersed case, a monotonic increase of the J-integral is observed. This is consistent with the calculations of Wang et. al.,(2012) and the observations by Bonn et al. (1998), and implies that delayed fracture is a possible symptom of this behavior. If a critical energy release rate J_{cr} is assumed (enough for the initiation of fracture in the hydrogel), and the initial value of the transient J-integral is less than the critical value, along with the equilibrium value being higher or equal to the critical value, $J_0^* < J_{cr} \leq J_\infty^*$, then these are sufficient conditions to imply that fracture could initiate at a time $t > 0$ after the loading has been applied. This is referred to as delayed fracture. Physically this can be interpreted, as a result of the increase of solvent concentration ahead of the crack tip, which in its turn results to polymer chains, whose fracture toughness remains constant, being less dense ahead of the crack tip. This of course is not a complete picture of the phenomena, which has to be obtained through physically evaluating every term in the transient J-integral of Eq. (6.25). One assumption that has been made in this discussion, is that the critical fracture toughness is a material parameter depending on the initial state of the gel and remains constant throughout the relaxation process.

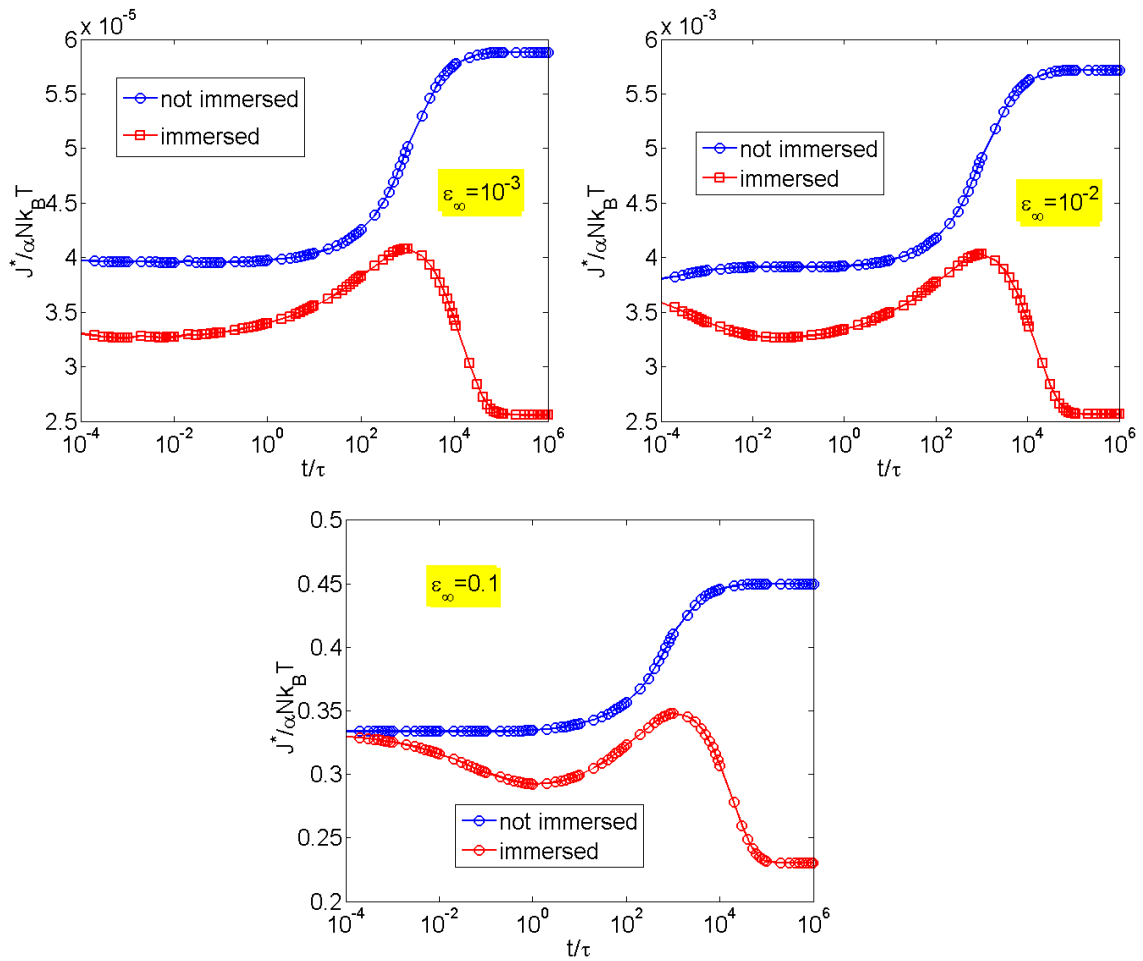


Figure 6.12: Transient J-integral evolution for immersed and not-immersed cases for increasing loading resulting to far field strains $\epsilon^\infty = 10^{-3}, 10^{-2}, 10^{-1}$.

For the immersed case, the instantaneous response at $t \rightarrow 0$ is expected to be the same as the not-immersed case, and the values of the transient J-integral at that time are expected to be equal. In Figure 6.12, for $\varepsilon^\infty = 10^{-3}$, the expected instantaneous behavior, is not captured, and this is believed to be an effect of the boundary condition $\mu=0$, being interpolated to the integration points located in the crack tip elements at the instantaneous limit. This effect is present even if the size of the element is reduced. As it will be discussed later, the instantaneous behavior is captured more successfully when larger loading is considered and the possibility for delayed fracture for the immersed case will also be discussed.

Considering a variation of the material parameters, for $\varepsilon^\infty = 10^{-3}$, and $h/a = 10$, the evolution of the transient J-integral for a not-immersed hydrogel model is presented in Figure 6.13. First, holding the Flory parameter fixed at $\chi = 0.2$, while the crosslink density will be considered at $N\Omega = 10^{-2}, 10^{-3}, 10^{-4}$ and following, the Flory parameter will be considered at $\chi = 0.2, 0.4, 0.6$, and the crosslink density will be fixed at $N\Omega = 10^{-2}$. When plotted using the previous normalization, there is a large variation in values, even though the monotonically increasing behavior is still observed for all cases. Following, the time is normalized using the linear poroelastic timescale defined as $\tau_* = a^2 / D^*$, by using the linearized elastic properties (G_0 and ν_∞) of the hydrogel and the effective diffusivity from Eq. (2.56)

$$D^* = \frac{2(1-\nu_\infty)(\lambda_0^3 - 1)\Omega G_0}{(1-2\nu_\infty)\lambda_0^3 k_B T} D \quad (6.35)$$

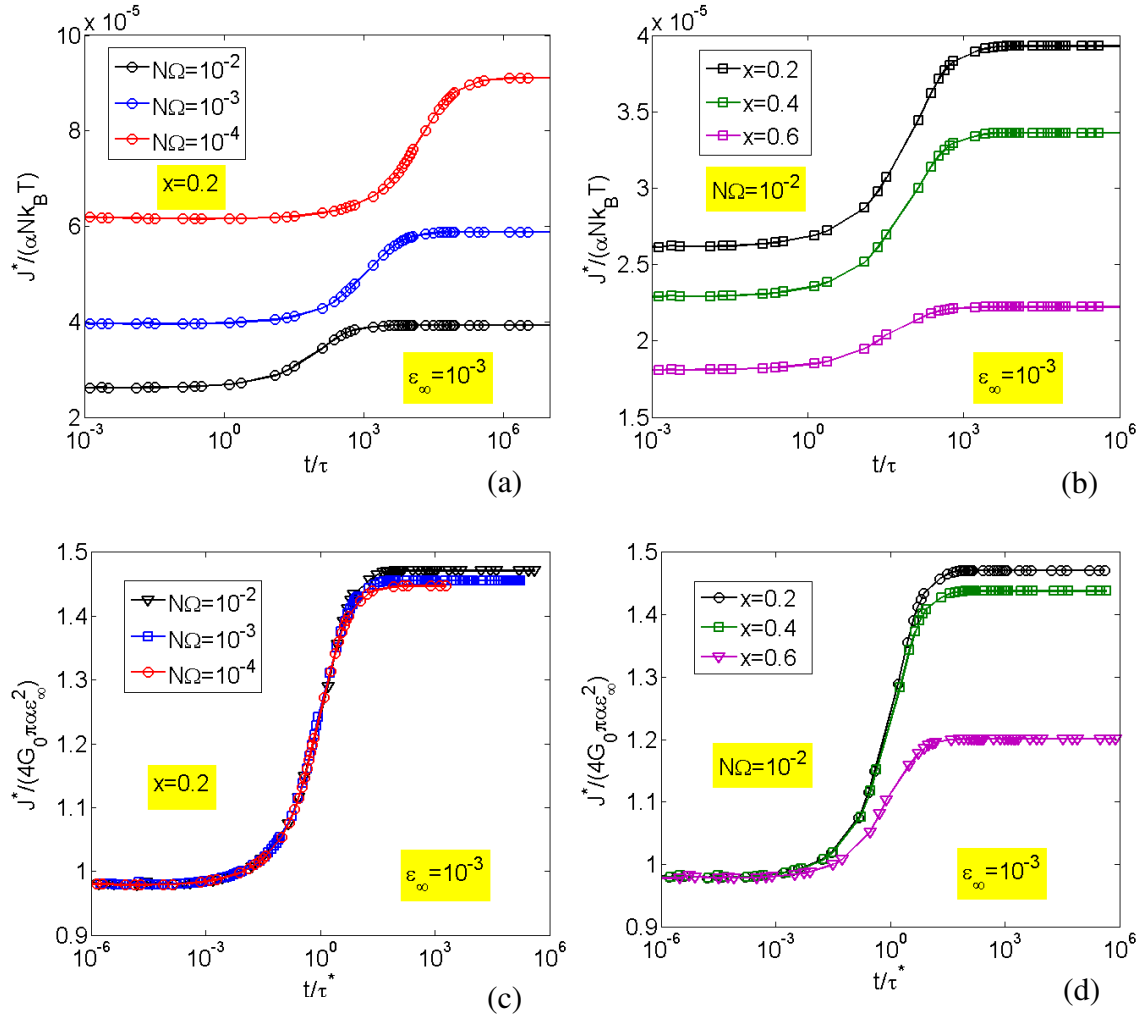


Figure 6.13: Material parameter dependence of the transient J-integral for a not-immersed hydrogel with a center crack is studied. Variation of the crosslink density $N\Omega$ (a,c) and of χ (b,d) are considered for the same type of displacement controlled Mode I loading up to $\epsilon^\infty = 0.1$ for a domain of size $h/\alpha = 10$, using timescale τ for plots (a,b) and timescale τ^* for plots (c,d).

Also, the value of the J integral is normalized by $(4G_0\pi a\epsilon_\infty^2)$, using the value obtained from linear elasticity for the instantaneous response from $J = K_I^2 / E^*$, where the intensity follows Eq. (6.29), Poisson's ratio is $\nu_0 = 0.5$ and the shear modulus G_0 by Eq. (A.18). Using this normalization, the results collapse at the instantaneous limit, showing the energy release is close to the prediction from linear elasticity $J^* / (4G_0\pi a\epsilon_\infty^2)|_{t=0} \approx 1$, the deviation from the value of 1 could again be attributed to the finite size of the domain. The equilibrium limit is significantly larger at $J^* / (4G_0\pi a\epsilon_\infty^2)|_{t=\infty} \approx 1.4 \sim 1.5$. The transient evolution also collapses for most cases, using the new timescale. Equilibrium responses do not collapse because there is not an accurate linear approximation for that state for a not-immersed hydrogel. Also, the material with parameters $\chi = 0.6$, $N\Omega = 10^{-2}$ shows a more mild increase of the value of the transient J-integral. This can be explained based on the fact that $\chi > 0.5$, which characterizes the solvent as “poor” as discussed in Chapter 2 (Bouklas and Huang, 2012) and leads to significantly less swelling/solvent migration.

6.2.1.2. Moderate far-field deformations

Returning to Figure 6.12, higher loading cases are considered, still using the same sharp crack model $h/a = 10$. Far-field strains of $\epsilon^\infty = 10^{-2}$, and $\epsilon^\infty = 0.1$ are obtained through mode I displacement controlled loading. The transient J-integral evolution for the not-immersed case, follows the same pattern as for the small strain case. For the immersed case, the predicted behavior is captured for both cases. The transient J-integral starts from approximately the same value as the initial value for the not-immersed case, slightly drops, and then rises to a maximum value $J_\infty^* < J_0^* < J_{\max}^*$, following a drop to the equilibrium value. The maximum value can still be slightly higher than that of the

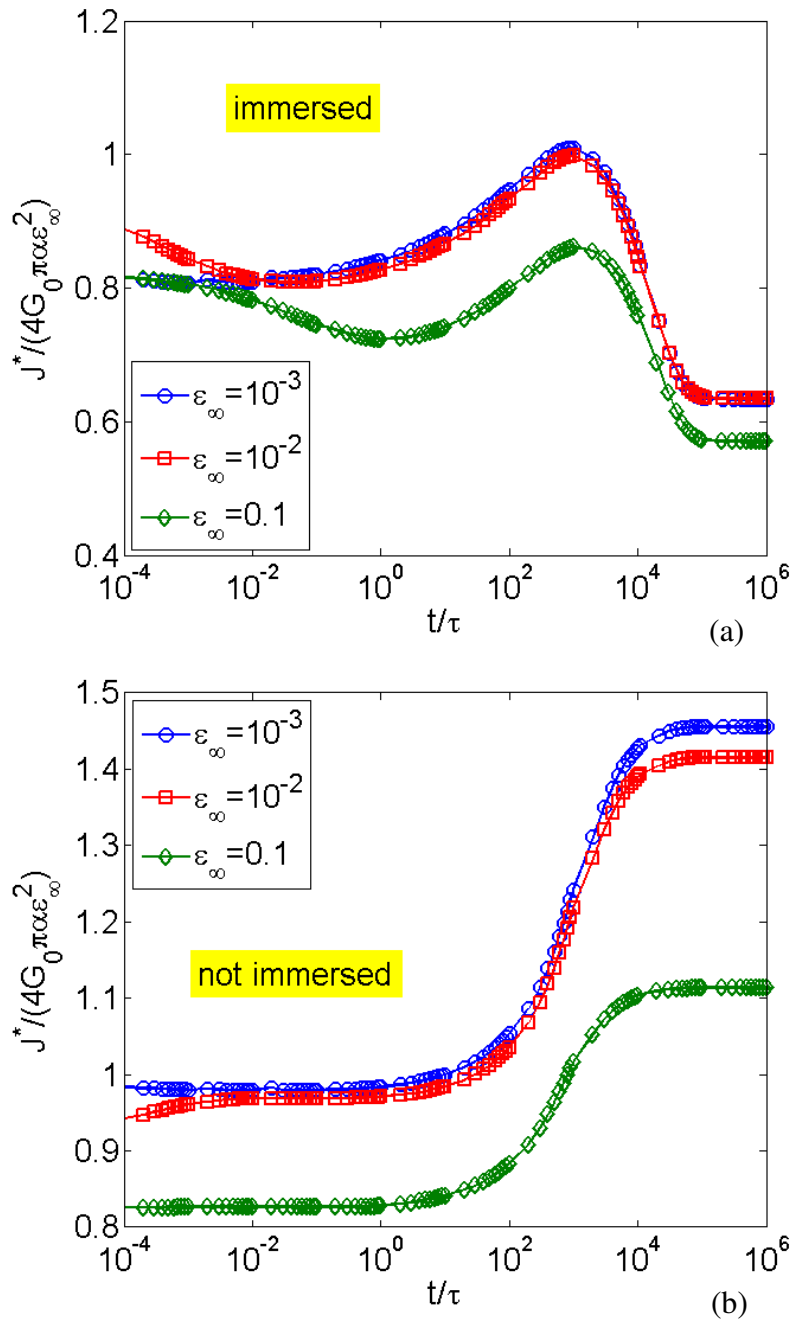


Figure 6.14: Normalized transient J-integral evolution comparing to the linear elastic solution for immersed (a) and not-immersed (b) cases for increasing loading specified by the far field strain.

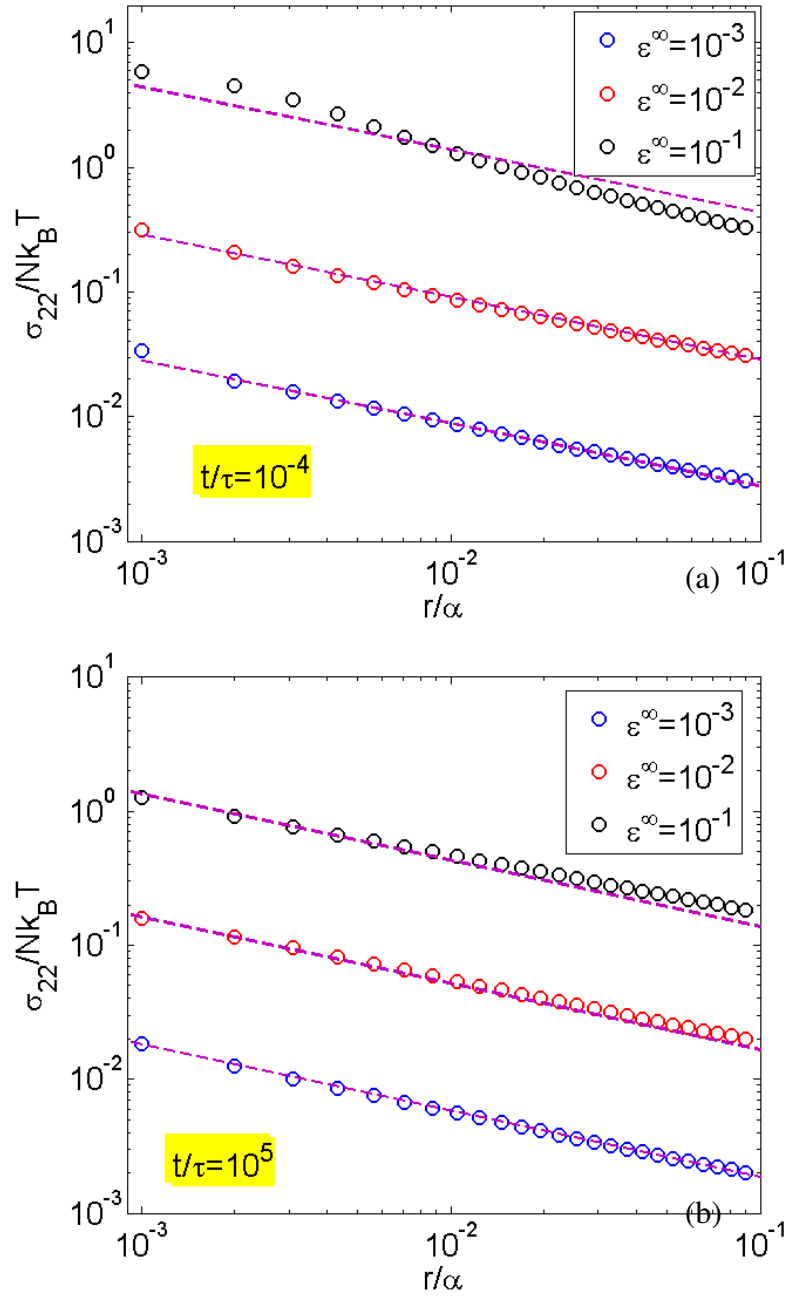


Figure 6.15: Cauchy stress σ_{22} component for the instantaneous (a) and equilibrium (b) response for an immersed center crack model loaded in Mode I for increasing loading indicated by the averaged quantity of the far field strain.

instantaneous value, which leaves the possibility for delayed fracture open. In Figure 6.12, the results of Figure 6.11 are plotted normalizing the transient J-integral based on the linear elastic solution. As higher loading is considered, the solution deviates from the instantaneous limit for both the immersed and the not immersed cases.

For the range of far field strains considered so far $\epsilon^\infty = 10^{-3}, 10^{-2}, 0.1$, the behavior of the stress field ahead of the crack tip is examined. The σ_{22} component of the Cauchy stress is plotted as a function of the radius from the crack tip in Figure 6.15. As observed by Zang et al. (2012), the singularity becomes stronger than square root singular at the instantaneous response as higher loading is considered. This can be attributed as a hyperelastic effect (Krishnan et al. 2008). On the contrary at the equilibrium limit, focusing on the highest loading case $\epsilon^\infty = 0.1$, a weaker than square root singular behavior is assumed. All the results so far have been obtained with a sharp crack model. One of the issues with this model is that the crack tip elements, due to their small size, which needs to be able to resolve the stress and chemical potential fields, become severely distorted, especially for higher loading ranges and cause convergence issues to the finite element analysis. Even $\epsilon^\infty = 0.1$ is a very moderate deformation for some hydrogels that are very stretchable (Sun et al. 2012) and often, higher levels of stretch are obtained. Thus it is necessary to accommodate even larger deformations with respect to the initial state.

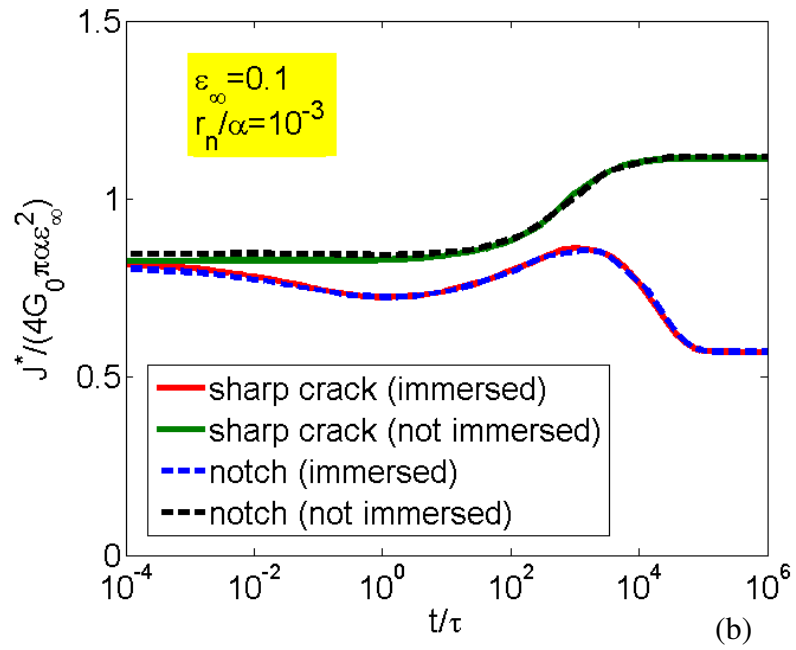
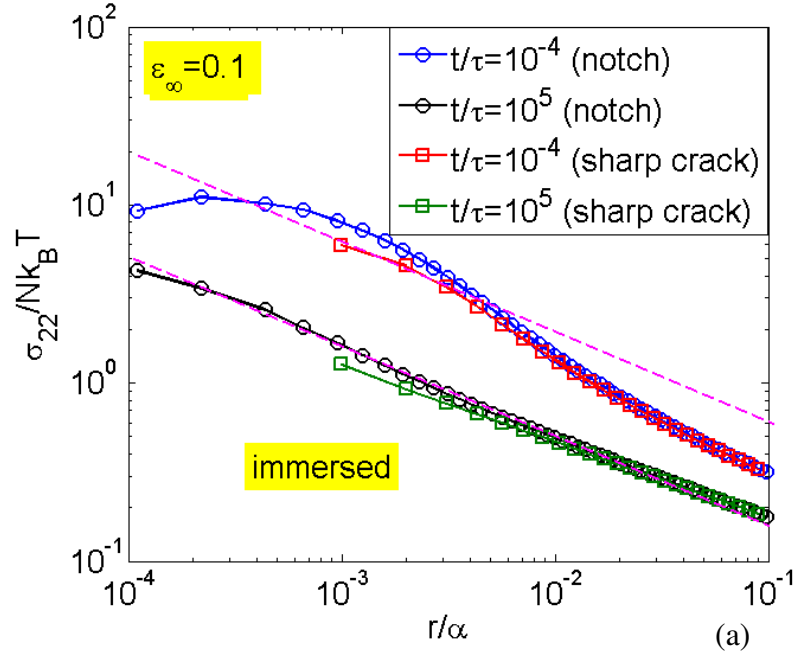


Figure 6.16: Comparison using a sharp crack and a notched model $r_n / \alpha = 10^{-3}$ for an immersed center crack model loaded in Mode I at $\varepsilon^\infty = 0.1$ for (a) Cauchy stress σ_{22} component for the instantaneous and equilibrium response and (b) the transient J-integral

6.2.2. Notched crack model

One way to accommodate very high deformations with respect to the initial state of the hydrogel in the finite element analysis, is to consider a notched crack geometry at the tip. The crack tip is rounded, with a radius r_n (Figure 6.4b). The mesh around the crack tip, can be designed, so that numerical stability is not an issue, even for significantly higher deformations. As mentioned previously, for the calculation of the energy release rate using the J-integral, the contribution of the contour integral on the notch cannot be ignored. Following Rice (1968b), the energy release rate, is calculated taking on volume V_1 and a surface integral S_2 (Figure 6.2b) in Eq. (6.25), but also subtracting the value of those integrals at the initial state (before loading is applied), where the free energy is not equal to zero, unless the initial state coincides with the dry state. Equivalently, invoking path-independence, the transient J-integral can be calculated by considering only the value of the contour integral on S_2 , which is traction-free, minus its initial value. These two procedures can be formulated as

$$J^* = \int_{S_2} \left(\hat{U}N_1 - s_{ij}N_j \frac{\partial x_i}{\partial X_1} \right) dS + \int_{V_1} \frac{\partial \mu}{\partial X_1} CdV - \left[\int_{S_2} \left(\hat{U}N_1 - s_{ij}N_j \frac{\partial x_i}{\partial X_1} \right) dS + \int_{V_1} \frac{\partial \mu}{\partial X_1} CdV \right]_{t=0} \quad (6.36)$$

and equivalently

$$J^* = \int_{-S_4} \hat{U}N_1 dS - \left[\int_{-S_4} \hat{U}N_1 dS \right]_{t=0} \quad (6.37)$$

The term regarding the initial state at both Eqs. (6.36-37) can be calculated analytically if the value of the free energy is known at the homogeneously swollen initial state and the blunted crack geometry follows the arc of a circle.

6.2.2.1. Moderate far-field deformations

First, a comparison with loading that creates moderately large far-field strain of $\varepsilon^\infty = 0.1$, is carried out between the sharp crack model of size $h/a = 10$ and a notched model with notch radius $r_n/a = 10^{-3}$ and size $h/a = 10$. Both materials have parameters $\chi = 0.2$ and $N\Omega = 10^{-3}$. In Figure 6.16a, the σ_{22} component of the Cauchy stress is plotted as a function of the radius from the crack tip at the instantaneous and equilibrium limits for an immersed hydrogel model. There is relatively good agreement at both states, considering the difference of the initial geometry of the crack. The evolution of the J-integral for both an immersed and a not-immersed hydrogel model is plotted in Figure 6.16b, comparing the results from the sharp crack and the notched crack models. There is a close agreement of the results, noting there is a slight difference at the initial response. This response could be attributed to the relative size of the radius, which was chosen at $r_n/a = 10^{-3}$ based on the discussion in McMeeking (1977). An even smaller notch radius could eliminate this difference, as is suggested by the results of Figure 6.20.

The crack opening displacement profile, for the immersed and the not-immersed model based on the same simulations, for sharp crack and notched crack models where $\varepsilon^\infty = 0.1$ is obtained, and presented in Figure 6.17. There is agreement for both cases at all times $t = 10^{-4}, 10^3, 10^5$ during the poroelastic relaxation, but a deviation from the elastic solution of Eq. (6.32) is also observed. In Figure 6.18, the chemical potential and the nominal concentration are also plotted ahead of the crack tip, up to the far-field boundary of the domain of the immersed hydrogel model. The concentration exhibits an interesting behavior, which was harder to capture for lower loading as the magnitude of the changes in concentration were very small. The concentration near the crack tip, following an initial increase up until $t > 10^3$, starts decreasing until the equilibrium state. This change of behavior is consistent with the time when the maximum value for the

transient J-integral is obtained (Figure 6.16), and also the maximum crack opening displacement is obtained for the immersed case.

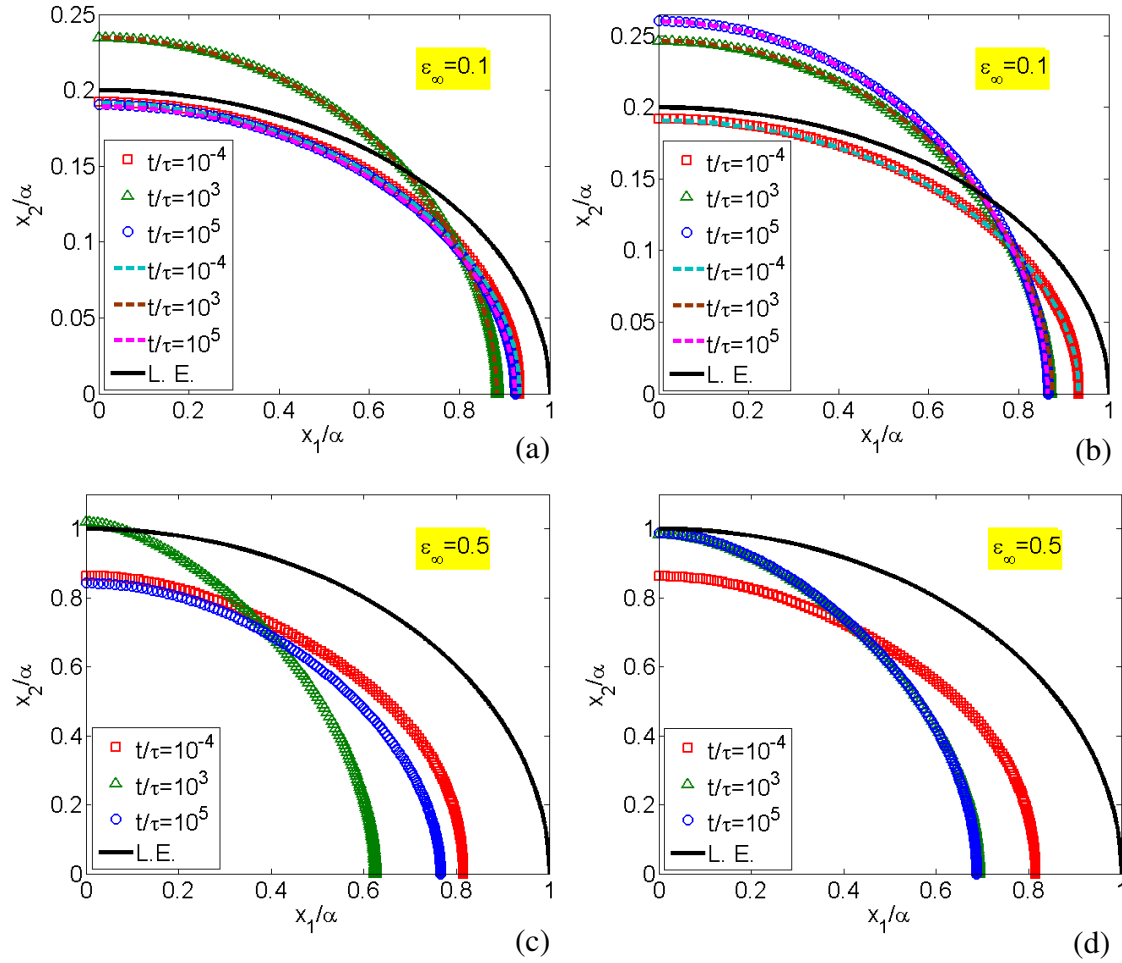


Figure 6.17: Evolution of the crack opening displacement profile with a notched center crack $r_n / \alpha = 10^{-3}$, for an (a) immersed and a (b) not-immersed hydrogel loaded in Mode I at $\varepsilon^\infty = 0.1$, and for an (c) immersed and a (d) not-immersed hydrogel loaded in Mode I at $\varepsilon^\infty = 0.5$.

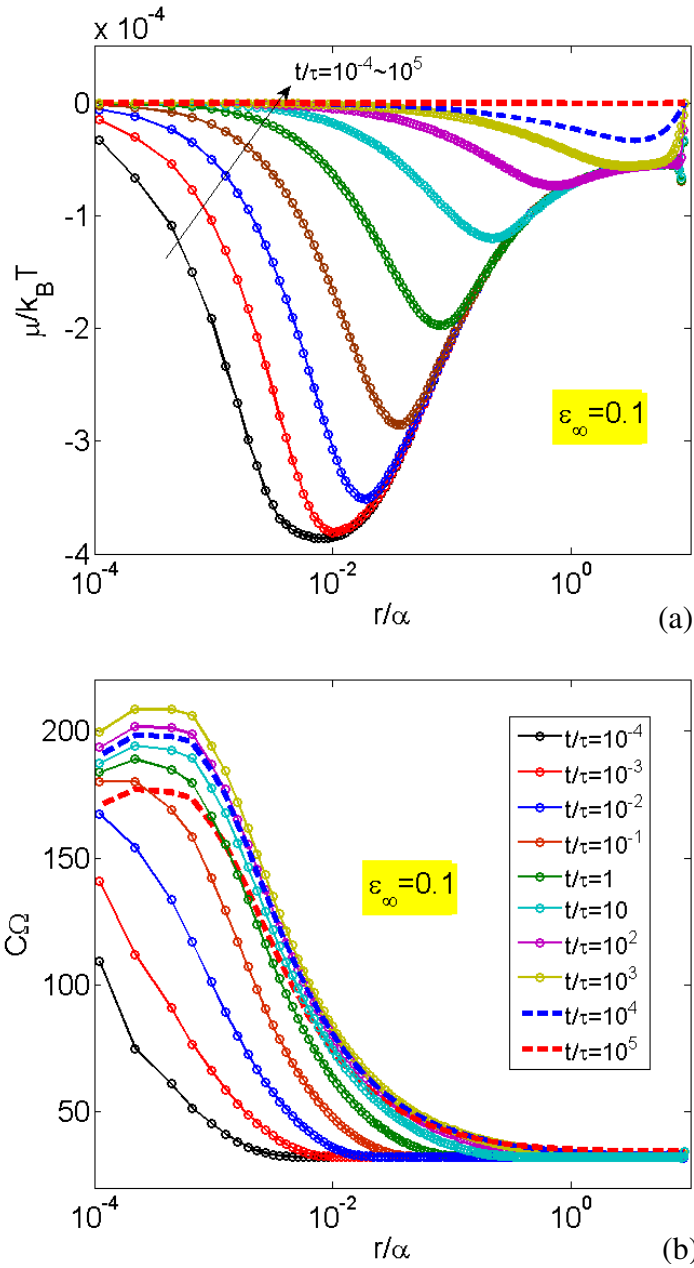


Figure 6.18: Evolution of (a) the chemical potential and (b) the concentration field, from the crack tip to the end of the specimen for an immersed hydrogel with a notch $r_n / \alpha = 10^{-3}$.

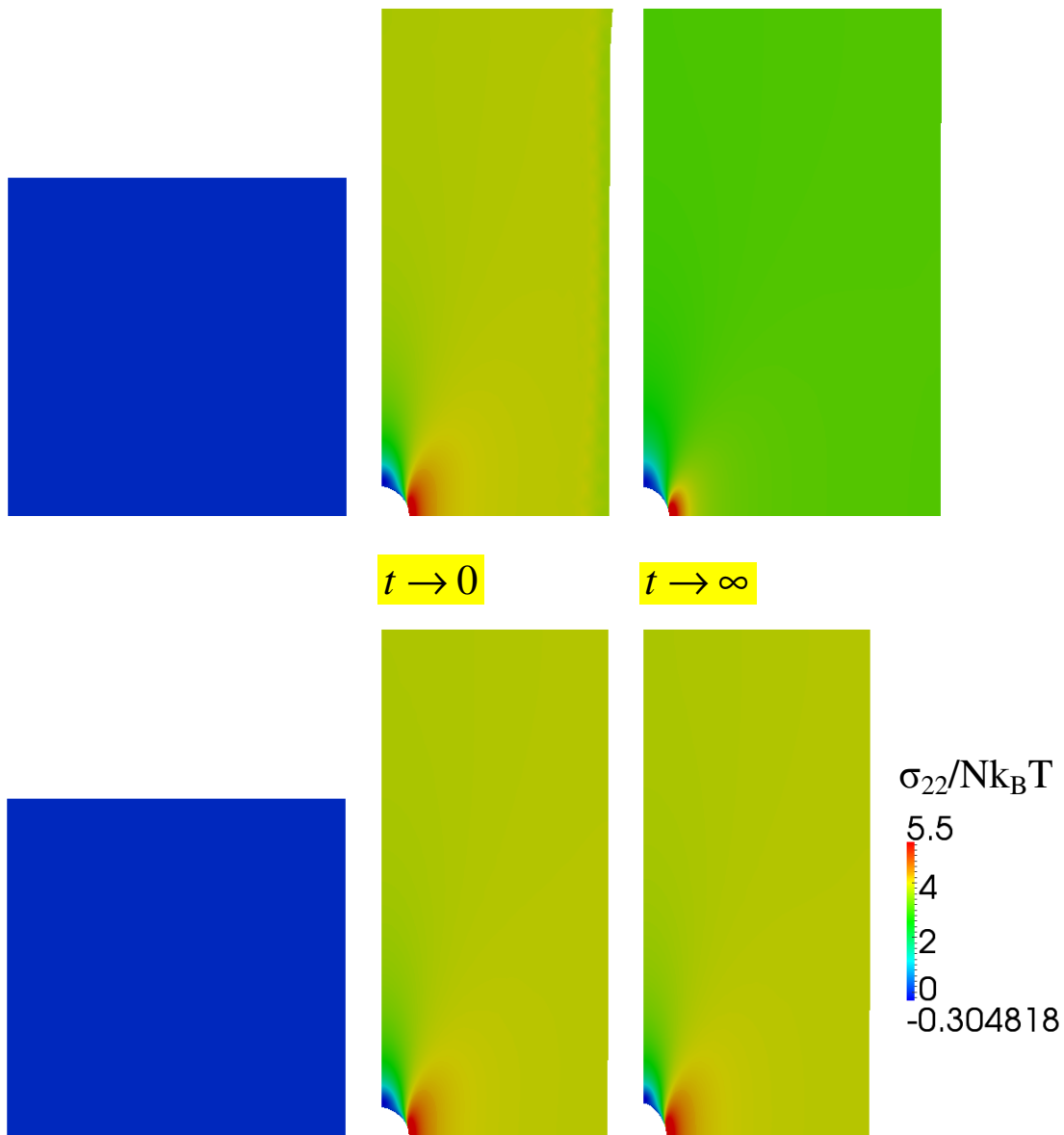


Figure 6.19: Immersed (top) and not immersed (bottom), center crack specimen with notch radius $r_n / \alpha = 10^{-3}$ loaded in Mode I at $\varepsilon^\infty = 0.5$, from left to right: before loading, after instantaneous loading and at equilibrium. Note that the notch is not even visible in the initial configuration.

6.2.2.2. Large far-field deformations

As a final example, and to demonstrate the potential of the notched mesh geometry, a significantly higher loading is considered and the far-field strain that is obtained reaches $\varepsilon^\infty = 0.5$ for both an immersed and a not-immersed hydrogel model. The notch radius is $r_n/a = 10^{-3}$ and the size of the domain $h/a = 10$. Material parameters are $\chi = 0.2$ and $N\Omega = 10^{-3}$. In figure 18, the crack opening profile is shown, where the opening-closing behavior is still maintained for the immersed model, and the same stands for the behavior of not-immersed model. Even larger deviation from the linear elastic results is observed. In Figure 6.19a contour plot of the σ_{22} component of the Cauchy stress is presented at the instantaneous and equilibrium limits, for both the immersed and the not immersed case, and also the un-deformed/initial state is shown. The volume change in the immersed case is significant compared to the initial volume of the hydrogel, and the relaxation of the stress concentration near the crack tip is also higher for the immersed case. The evolution of the transient J-integral is shown in Figure 6.20, where the loading path is also presented. The monotonic behavior of the value of the transient J-integral corresponding to the not-immersed case and the behavior for the immersed case are still consistent with the behavior for small far-field strains.

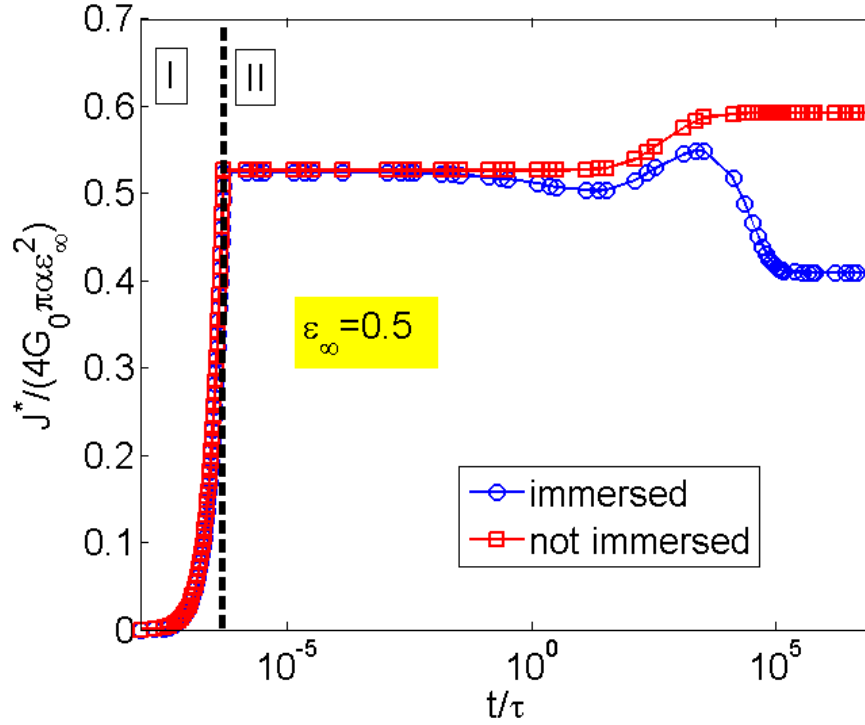


Figure 6.20: Evolution of the transient J-integral obtained from an immersed and a not immersed notched model, with notch radius $r_n / \alpha = 10^{-3}$ loaded in Mode I at $\epsilon^\infty = 0.5$. Stage I refers to loading, and stage II to the transient relaxation.

6.3. SUMMARY

In this chapter, a consistent nonequilibrium thermodynamic approach is presented, to obtain the energy release rate for quasi-static crack extension, in poroelastic relaxation of hydrogels. A transient modified form for the J-integral, that includes both a volume and a surface part, and equals the energy release rate is also presented. Path independence for the transient J-integral is proved. Unlike previous studies on models that exhibit energy dissipation e.g. poroelasticity for geomechanics and thermoelasticity,

this transient J-integral can provide the energy release rate at any state of the transient process. A specific material and kinetic law are assumed. A mixed finite element method is implemented. Numerical results are presented, for mode I displacement controlled loading for an immersed and not-immersed hydrogel model, using a sharp crack and a notched crack geometry, to accommodate various levels of loading. The behavior of the stress, chemical potential, concentration and deformation fields at the small far-field strain level are analyzed extensively, and compared to solutions from linear fracture mechanics using a linearization procedure for hydrogels previously presented by the authors. The transient J-integral is also calculated, and the possibility of delayed fracture is established, mainly for the not-immersed case. Capability of numerical calculations for higher levels of loading is also confirmed using the notched crack geometry, and compared to the results from the sharp crack geometry for moderate levels of loading. The derivation of the transient J-integral, suggest that not only could it be used to investigate more complicated problems in hydrogel fracture, like crack propagation, where the possibility of a stick-slip behavior is expected, but it could also be useful for the study of fracture in materials that exhibit other dissipative processes (solid state diffusion, poroelasticity). Of course, in order for the study of crack propagation to be complete, experimental studies have to compliment the theoretical formulation, to provide accurate fracture criteria. The novel point in the derivation of the transient J-integral is the fact that it separates the energy lost in dissipation from the energy to be lost in crack propagation.

Chapter 7

Conclusions

The present study deals with the effect of solvent diffusion in hydrogels and their transient response that includes large deformation. Constitutive theories including material and kinetic laws are adopted and a mixed nonlinear finite element method is developed for the study of the transient responses of hydrogels. Hydrogel swelling, indentation, and fracture are considered as numerical examples to be studied with the methods.

In Chapter 2, a comparison between a nonlinear theory for polymer gels and the classical theory of linear poroelasticity is presented. Considering incompressible constituents, it is shown that under the condition of small perturbations from an isotropically swollen state of the gel, the two theories are consistent. A linearization procedure provides the relationships between the material properties of the two theories. Both linear and nonlinear solutions are presented for swelling kinetics of substrate-constrained and freestanding hydrogel layers. It is shown that the applicability of the linear poroelasticity theory is valid only in the small deformation regime, and a new procedure is suggested to fit the experimental data with the nonlinear theory regarding the experimental characterization of hydrogels.

In Chapter 3, a nonlinear, transient finite element formulation is presented for initial boundary value problems associated with swelling and deformation of hydrogels. Two material models are considered, one where the constituents of the hydrogel are compressible and one where they are incompressible. The suggested mixed finite element method is implemented, with specific attention to the numerical stability issues associated

with the LBB condition arising from the nearly incompressible instantaneous response of the hydrogel.

In Chapter 4, numerical results are presented for constrained swelling of hydrogels, using the theory and the finite element method for hydrogels with compressible constituents. The results are compared to solutions from Chapter 2 regarding homogeneous swelling. The application of Taylor-Hood elements is shown to alleviate the numerical stability issues connected to the LBB condition. Instantaneous instability during swelling for single hydrogel layers, and wrinkling of hydrogel bilayers are discussed.

In Chapter 5, numerical results are presented for flat-punch indentation of hydrogel layers, again using the compressible theory and corresponding finite element formulation. The relaxation process following instantaneous loading is studied. The use of a penalty method is necessary to capture the instantaneous response accurately. The response at the instantaneous and equilibrium limits is compared to the response of linear elastic materials. It is found that the normalized indentation relaxation curve depends on the effective Poisson's ratio of the hydrogel, for the case of plane strain flat-punch indentation. Moreover, the effects of loading rate on indentation relaxation are discussed.

A consistent nonequilibrium thermodynamic approach for fracture of hydrogels is presented in Chapter 6, to obtain the transient energy release rate for crack propagation. By considering the effect of diffusive dissipation, a modified J-integral is derived and proved to be path independent. Numerical examples for displacement controlled mode I loading are studied using the incompressible theory and finite element method presented in Chapter 3. A sharp crack and a notched crack geometry are considered. The model is compared to linear elastic fracture mechanics in the small (far-field) deformation regime and also tested for large deformations. The transient J-integral increases monotonically

with time for the case of not-immersed swelling. To further build on this work a critical energy release rate criterion can be adopted, in parallel with experimental studies, and by using a crack growth rule, crack propagation can be studied along with interesting phenomena as delayed fracture and stick-slip crack propagation.

Appendices

APPENDIX A: LINEAR ELASTIC PROPERTIES OF HYDROGELS

To determine the linear elastic properties of a swollen gel based on the nonlinear theory, we assume that the gel is in chemical equilibrium and thus the chemical potential remains a constant everywhere in the gel during deformation. Take the initial state of the gel to be stress free and isotropically swollen with a swelling ratio λ_0 in all directions, relative to the dry state. The chemical potential in the gel is thus fixed by the swelling ratio as given in Eq. (3.1). Now consider three simple loading conditions imposed on the swollen gel: uniaxial stress, hydrostatic pressure, and simple shear.

Under a uniaxial stress, the only non-zero component of the nominal stress is

$$s_{11} = \lambda_2^2 \sigma \quad (\text{A.1})$$

where σ is the true stress in the 1-direction and λ_2 is the stretch in the lateral direction (relative to the dry state).

By the nonlinear constitutive relation in (2.7), we obtain that

$$s_{11} = Nk_B T (\lambda_1 + \alpha \lambda_2^2) \quad (\text{A.2})$$

$$s_{22} = s_{33} = Nk_B T (\lambda_2 + \alpha \lambda_1 \lambda_2) \quad (\text{A.3})$$

where

$$\alpha = -\frac{1}{\lambda_1 \lambda_2^2} + \frac{1}{N\Omega} \left(\ln \frac{\lambda_1 \lambda_2^2 - 1}{\lambda_1 \lambda_2^2} + \frac{1}{\lambda_1 \lambda_2^2} + \frac{\chi}{\lambda_1^2 \lambda_2^4} - \frac{\mu_0}{k_B T} \right) \quad (\text{A.4})$$

By setting $s_{22} = s_{33} = 0$, we obtain the lateral stretch (λ_2) as a function of the axial stretch (λ_1), namely

$$\ln \left(\frac{\lambda_1 \lambda_2^2 - 1}{\lambda_1 \lambda_2^2} \right) + \frac{N\Omega}{\lambda_1} + \frac{1 - N\Omega}{\lambda_1 \lambda_2^2} + \frac{\chi}{\lambda_1^2 \lambda_2^4} - \frac{\mu_0}{k_B T} = 0 \quad (\text{A.5})$$

For a small deformation from the initial state, we have

$$\lambda_1 = \lambda_0(1 + \varepsilon_1) \text{ and } \lambda_2 = \lambda_0(1 + \varepsilon_2) \quad (\text{A.6})$$

where ε_1 and ε_2 are the linear strain components in the axial and lateral directions, respectively. Assuming $\varepsilon_1, \varepsilon_2 \ll 1$, we linearize Eq. (A.5) and obtain

$$\left[\frac{1}{\lambda_0^3 - 1} - \frac{1 - N\Omega}{\lambda_0^3} - \frac{2\chi}{\lambda_0^6} \right] (2\varepsilon_2 - \varepsilon_1) - \left(\frac{N\Omega}{\lambda_0} \right) \varepsilon_1 = 0 \quad (\text{A.7})$$

Poisson's ratio of the swollen gel is then defined as

$$\nu = -\frac{\varepsilon_2}{\varepsilon_1} = \frac{1}{2} - \frac{N\Omega}{2} \left[\frac{1}{\lambda_0^2(\lambda_0^3 - 1)} + \frac{N\Omega}{\lambda_0^2} - \frac{2\chi}{\lambda_0^5} \right]^{-1} \quad (\text{A.8})$$

which is used in (2.20).

Combining (A.1) and (A.2), we obtain the axial stress as a function of the axial stretch:

$$\frac{\sigma}{Nk_B T} = \frac{\lambda_1}{\lambda_2^2} - \frac{1}{\lambda_1} \quad (\text{A.9})$$

Linearizing (A.9) leads to

$$\sigma = \frac{2Nk_B T}{\lambda_0} (\varepsilon_1 - \varepsilon_2) \quad (\text{A.10})$$

Thus, Young's modulus of the swollen gel is

$$E = \frac{\sigma}{\varepsilon_1} = \frac{2(1 + \nu)}{\lambda_0} Nk_B T \quad (\text{A.11})$$

Therefore, by considering the equilibrium deformation of the swollen gel under a uniaxial stress, we determine Young's modulus and Poisson's ratio as the linear elastic

properties under the condition of small deformation ($\varepsilon_1, \varepsilon_2 \ll 1$) based on the nonlinear theory.

Next consider the swollen hydrogel under a hydrostatic pressure p . In this case, the swelling ratio of the gel remains isotropic, i.e., $\lambda_1 = \lambda_2 = \lambda_3 = \lambda$. Correspondingly, the nominal stresses are

$$s_{11} = s_{22} = s_{33} = -\lambda^2 p \quad (\text{A.12})$$

Inserting (A.12) into (A.2), we obtain the swelling ratio as a function of the pressure:

$$\ln \frac{\lambda^3 - 1}{\lambda^3} + \frac{1}{\lambda^3} + \frac{\chi}{\lambda^6} + N\Omega \left(\frac{1}{\lambda} - \frac{1}{\lambda^3} \right) = \frac{\mu_0 - p\Omega}{k_B T} \quad (\text{A.13})$$

By (A.13), the swelling ratio (λ) decreases as the external pressure increases. In other words, applying external pressure directly onto the gel, not through the solvent, can squeeze out solvent molecules. On the other hand, applying pressure through the solvent would change the chemical potential in the gel and the external solvent simultaneously, which would not change the volume of the gel.

By linearizing (A.13), a bulk modulus of the swollen gel can be defined as

$$B = - \left(\frac{\lambda}{3} \frac{dp}{d\lambda} \right)_{p=0} = Nk_B T \left[\frac{1}{N\Omega} \frac{1}{\lambda_0^3 (\lambda_0^3 - 1)} - \frac{2\chi}{N\Omega} \frac{1}{\lambda_0^6} - \frac{1}{3\lambda_0} + \frac{1}{\lambda_0^3} \right] \quad (\text{A.14})$$

With Young's modulus in (A.11) and Poisson's ratio in (A.8), it can be confirmed that the bulk modulus, $B = E/[3(1-2\nu)]$, consistent with the linear elasticity theory.

For simple shear, we assume a deformation gradient

$$\mathbf{F} = \lambda_0 \begin{bmatrix} 1 & \gamma & 0 \\ 0 & 1 & 0 \\ 0 & 0 & 1 \end{bmatrix} \quad (\text{A.15})$$

where γ is the shear strain imposed onto the initial state of the gel. By the constitutive relation in (2.7), the only non-zero component of the nominal stress is

$$s_{21} = Nk_B T (\lambda_0 \gamma) \quad (\text{A.16})$$

The true shear stress is obtained as

$$\sigma_{21} = \frac{s_{21}}{\lambda_0^2} = \frac{Nk_B T}{\lambda_0} \gamma \quad (\text{A.17})$$

Thus the shear modulus of the swollen gel is

$$G = \frac{\sigma_{21}}{\gamma} = \frac{Nk_B T}{\lambda_0} \quad (\text{A.18})$$

which is used in Eq. (2.20). Again, it can be confirmed that the Young's modulus in (A.11), Poisson's ratio in (A.8), and the shear modulus in (A.18) satisfy the relationship for isotropic linear elasticity: $G = E/[2(1+\nu)]$.

It is notable that the nonlinear theory predicts a linear relationship between the shear strain and shear stress for the case of simple shear while the stress-strain behavior under uniaxial stress and hydrostatic pressure is nonlinear in general.

APPENDIX B: SOLUTION PROCEDURES FOR CONSTRAINED AND FREE SWELLING

B.1 Constrained swelling by the nonlinear theory

For constrained swelling of a thin layer, the stretch in the thickness direction is a function of time and position, $\lambda_2 = \lambda_2(X_2, t)$, whereas $\lambda_1 = \lambda_3 = \lambda_0$. By the nonlinear theory, the nominal stresses in the gel are obtained from Eq. (2.7):

$$s_{11} = s_{33} = Nk_B T \left(\lambda_0 - \frac{1}{\lambda_0} \right) - \Pi \lambda_2 \lambda_0 \quad (\text{B.1})$$

$$s_{22} = Nk_B T \left(\lambda_2 - \frac{1}{\lambda_2} \right) - \Pi \lambda_0^2 \quad (\text{B.2})$$

The mechanical equilibrium equation in (2.8) requires that

$$\frac{\partial s_{22}}{\partial X_2} = 0 \quad (\text{B.3})$$

With the traction-free boundary condition at the upper surface, i.e., $s_{22}(X_2 = H) = 0$, we have $s_{22}(X_2, t) = 0$ everywhere in the gel and hence by (B.2)

$$\Pi(X_2, t) = \frac{Nk_B T}{\lambda_0^2} \left(\lambda_2 - \frac{1}{\lambda_2} \right) \quad (\text{B.4})$$

Next, inserting (B.4) into (2.6), the chemical potential in the gel is obtained:

$$\mu(X_2, t) = k_B T \left[\ln \frac{\lambda_0^2 \lambda_2 - 1}{\lambda_0^2 \lambda_2} + \frac{1}{\lambda_0^2 \lambda_2} + \frac{\chi}{\lambda_0^4 \lambda_2^2} + \frac{N\Omega}{\lambda_0^2} \left(\lambda_2 - \frac{1}{\lambda_2} \right) \right] \quad (\text{B.5})$$

The nominal mobility as defined in (2.11) is specialized for this case as:

$$M_{11} = M_{33} = \frac{D}{\Omega k_B T} \left(\lambda_2 - \frac{1}{\lambda_0^2} \right) \quad (\text{B.6})$$

$$M_{22} = \frac{D}{\Omega k_B T} \left(\frac{\lambda_0^2}{\lambda_2} - \frac{1}{\lambda_2^2} \right) \quad (\text{B.7})$$

and $M_{12} = M_{23} = M_{31} = 0$. Thus, by (2.10), we have $J_1 = J_3 = 0$ and

$$J_2 = -M_{22} \frac{\partial \mu}{\partial X_2} = -\frac{D}{\Omega} \xi(\lambda_2) \frac{\partial \lambda_2}{\partial X_2} \quad (\text{B.8})$$

where

$$\xi(\lambda_2) = \frac{1}{\lambda_0^2 \lambda_2^4} - \frac{2\chi(\lambda_0^2 \lambda_2 - 1)}{\lambda_0^4 \lambda_2^5} + N\Omega \frac{(\lambda_0^2 \lambda_2 - 1)(\lambda_2^2 + 1)}{\lambda_0^2 \lambda_2^4} \quad (\text{B.9})$$

Finally, the diffusion equation (2.12) becomes

$$\lambda_0^2 \frac{\partial \lambda_2}{\partial t} = D \frac{\partial}{\partial X_2} \left(\xi \frac{\partial \lambda_2}{\partial X_2} \right) \quad (\text{B.10})$$

The nonlinear diffusion equation in (B.10) is solved numerically by a finite difference method. After normalizing the time and spatial coordinate as $\bar{t} = \frac{tD}{H^2}$ and $\bar{X} = \frac{X_2}{H}$, the diffusion equation takes a dimensionless form

$$\frac{\partial \lambda_2}{\partial \bar{t}} = \frac{\partial}{\partial \bar{X}} \left(\frac{\xi}{\lambda_0^2} \frac{\partial \lambda_2}{\partial \bar{X}} \right) \quad (\text{B.11})$$

By the finite difference method, we integrate (B.11) at each node with $\bar{X}_i = (i - 1)\Delta X$ for $i = 2$ to n and $\Delta X = 1/n$:

$$\lambda_2(\bar{X}_i, \bar{t} + \Delta t) = \lambda_2(\bar{X}_i, \bar{t}) - \frac{\Delta t}{\Delta X} \left[J\left(\bar{X}_i + \frac{\Delta X}{2}, \bar{t}\right) - J\left(\bar{X}_i - \frac{\Delta X}{2}, \bar{t}\right) \right] \quad (\text{B.12})$$

where

$$J\left(\bar{X}_i + \frac{\Delta X}{2}, \bar{t}\right) = -\xi\left(\bar{X}_i + \frac{\Delta X}{2}, \bar{t}\right) \frac{\lambda_2(\bar{X}_{i+1}, \bar{t}) - \lambda_2(\bar{X}_i, \bar{t})}{\lambda_0^2 \Delta X} \quad (\text{B.13})$$

and $\xi\left(\bar{X}_i + \frac{\Delta X}{2}, \bar{t}\right)$ is calculated using the swelling ratio at the midpoint by linear interpolation, i.e, $\lambda_2\left(\bar{X}_i + \frac{\Delta X}{2}, \bar{t}\right) = \frac{\lambda_2(\bar{X}_{i+1}, \bar{t}) + \lambda_2(\bar{X}_i, \bar{t})}{2}$.

The swelling ratio at the upper surface, $\lambda_2(\bar{X}_{n+1}, \bar{t}) = \lambda_\infty^c$, is fixed by the local equilibrium condition. At the lower surface ($X = 0$), the flux is zero and the swelling ratio is integrated as

$$\lambda_2(0, \bar{t} + \Delta t) = \lambda_2(0, \bar{t}) - \frac{2\Delta t}{\Delta X} J\left(\frac{\Delta X}{2}, \bar{t}\right) \quad (\text{B.14})$$

For the first step, $\lambda_2(\bar{X}_i, 0) = \lambda_0$, except at the upper surface. The numerical method is conditionally stable that requires a relatively small time step Δt . In our calculations for Fig. 2 and Fig. 3, we have used $\Delta X = 0.02$ and $\Delta t = 0.001$.

B.2 Free swelling by the nonlinear theory

For free swelling, solvent molecules enter the gel from both sides, and the gel swells in all directions. By symmetry, the layer remains flat, with $\lambda_2 = \lambda_2(X_2, t)$ and $\lambda_1 = \lambda_3 = \lambda_1(t)$. By the nonlinear theory the nominal stresses are

$$s_{11} = s_{33} = Nk_B T \left(\lambda_1 - \frac{1}{\lambda_1} \right) - \Pi \lambda_2 \lambda_1 \quad (\text{B.15})$$

$$s_{22} = Nk_B T \left(\lambda_2 - \frac{1}{\lambda_2} \right) - \Pi \lambda_1^2 \quad (\text{B.16})$$

The mechanical equilibrium equation, along with the boundary condition, requires that $s_{22}(X_2, t) = 0$ everywhere in the gel and thus

$$\Pi(X_2, t) = \frac{Nk_B T}{\lambda_1^2} \left(\lambda_2 - \frac{1}{\lambda_2} \right) \quad (\text{B.17})$$

By inserting (B.17) into (2.6), the chemical potential in the gel is obtained:

$$\mu(X_2, t) = k_B T \left[\ln \frac{\lambda_1^2 \lambda_2 - 1}{\lambda_1^2 \lambda_2} + \frac{1}{\lambda_1^2 \lambda_2} + \frac{\chi}{\lambda_1^4 \lambda_2^2} + \frac{N\Omega}{\lambda_1^2} \left(\lambda_2 - \frac{1}{\lambda_2} \right) \right] \quad (\text{B.18})$$

The nominal mobility for this case is

$$M_{22} = \frac{D}{\Omega k_B T} \left(\frac{\lambda_1^2}{\lambda_2} - \frac{1}{\lambda_2^2} \right), \quad (\text{B.19})$$

and the flux is

$$J_2 = -M_{22} \frac{\partial \mu}{\partial X_2} = -\frac{D}{\Omega} \bar{\xi}(\lambda_1, \lambda_2) \frac{\partial \lambda_2}{\partial X_2}, \quad (\text{B.20})$$

where

$$\bar{\xi}(\lambda_1, \lambda_2) = \frac{1}{\lambda_1^2 \lambda_2^4} - \frac{2\chi(\lambda_1^2 \lambda_2 - 1)}{\lambda_1^4 \lambda_2^5} + N\Omega \frac{(\lambda_1^2 \lambda_2 - 1)(\lambda_2^2 + 1)}{\lambda_1^2 \lambda_2^4}. \quad (\text{B.21})$$

The nonlinear diffusion equation (2.12) then becomes

$$\Omega \frac{\partial C}{\partial t} = \lambda_1^2 \frac{\partial \lambda_2}{\partial t} + 2\lambda_1 \lambda_2 \frac{d\lambda_1}{dt} = D \frac{\partial}{\partial X_2} \left(\bar{\xi} \frac{\partial \lambda_2}{\partial X_2} \right) \quad (\text{B.22})$$

Furthermore, with no constraint in the in-plane directions, the in-plane stress must be self-balanced, namely

$$\int_0^H s_{11} dX_2 = Nk_B T \left(\lambda_1 - \frac{1}{\lambda_1} \right) H - \lambda_1 \int_0^H \Pi \lambda_2 dX_2 = 0 \quad (\text{B.23})$$

Inserting (B.17) into (B.23), we obtain that

$$\lambda_1^2 = \frac{1}{H} \int_0^H \lambda_2^2 dX_2 \quad (\text{B.24})$$

The two nonlinear equations (B.22) and (B.24) are solved simultaneously using a finite difference method. After normalization ($\bar{t} = \frac{tD}{H^2}$ and $\bar{X} = \frac{X_2}{H}$), Eq. (B.22) becomes

$$\lambda_1^2 \frac{\partial \lambda_2}{\partial \bar{t}} + 2\lambda_1 \lambda_2 \frac{d\lambda_1}{d\bar{t}} = \frac{\partial}{\partial \bar{X}} \left[\bar{\xi}(\lambda_1, \lambda_2) \frac{\partial \lambda_2}{\partial \bar{X}} \right] \quad (\text{B.25})$$

We integrate (B.25) at each node with $\bar{X}_i = (i - 1)\Delta X$ for $i = 2$ to n and $\Delta X = 1/n$:

$$(\lambda_1)^2 \frac{(\Delta\lambda_2)_i}{\Delta t} + 2\lambda_1(\lambda_2)_i \frac{\Delta\lambda_1}{\Delta t} = \frac{J(X_i + \frac{\Delta X}{2}) - J(X_i - \frac{\Delta X}{2})}{\Delta X} \quad (\text{B.26})$$

where

$$J\left(X_i + \frac{\Delta X}{2}\right) = \bar{\xi}\left(\lambda_1, \frac{(\lambda_2)_i + (\lambda_2)_{i+1}}{2}\right) \frac{(\lambda_2)_{i+1} - (\lambda_2)_i}{\Delta X} \quad (\text{B.27})$$

The swelling ratio at the two end nodes ($i = 1$ and $n+1$) must satisfy the local equilibrium condition in (2.45), which may be written as $f(\lambda_1, \lambda_2) = 0$. Take the derivative of (2.45) with respect to λ_1 and λ_2 , we obtain

$$g_1(\lambda_1, \lambda_2)\Delta\lambda_1 + g_2(\lambda_1, \lambda_2)\Delta\lambda_2 = 0 \quad (\text{B.28})$$

where $g_1 = \partial f / \partial \lambda_1$ and $g_2 = \partial f / \partial \lambda_2$.

Discretization of (B.24) leads to

$$\lambda_1^2 = \Delta X \sum_{i=2}^n (\lambda_2)_i^2 + \frac{\Delta X}{2} [(\lambda_2)_1^2 + (\lambda_2)_{n+1}^2] \quad (\text{B.29})$$

The incremental form of (B.29) is

$$2\lambda_1\Delta\lambda_1 = 2\Delta X \sum_{i=2}^n (\lambda_2)_i (\Delta\lambda_2)_i + \Delta X [(\lambda_2)_1 (\Delta\lambda_2)_1 + (\lambda_2)_{n+1} (\Delta\lambda_2)_{n+1}] \quad (\text{B.30})$$

The discretized equations in (B.26), (B.28), and (B.30) form a complete linear system that can be written in a matrix form as

$$\mathbf{M}\mathbf{u} = \mathbf{P} \quad (\text{B.31})$$

where $\mathbf{u} = (\Delta\lambda_1, (\Delta\lambda_2)_i, i = 1 \dots n+1)$, \mathbf{M} is a $n+2$ by $n+2$ matrix, and \mathbf{P} is a vector of $n+2$ components. Thus, solving (B.31) we obtain the increments for the swelling ratios, with which we update the swelling ratio for the next time step.

For the first time step ($t = 0^+$), the swelling ratios are obtained by solving the nonlinear equation (2.45) along with the conditions that $(\lambda_2)_i = \lambda_0^3 / \lambda_1^2$ for $i = 2$ to n and

$(\lambda_2)_{1,n+1}^2 = n\lambda_1^2 - (n-1)\lambda_0^6/\lambda_1^4$. Again, the numerical method is conditionally stable. In our calculation for Fig. 4, we have used $\Delta X = 0.02$ and $\Delta t = 0.0025$.

B.3 Free swelling by the linear poroelasticity theory

A numerical method is used to solve Eqs. (2.46)-(2.48) by the linear poroelasticity theory for free swelling. For convenience, we normalize the chemical potential as $\mu/G\Omega$, the displacement as u/h_0 , and the time as tD^*/h_0^2 . The normalized space domain is $z = x_2/h_0 \in [0,1]$. The boundary conditions are: $\mu(0, t) = 0$, $\mu(1, t) = 0$, and $u(0, t) = 0$. The initial conditions are: $\mu(z, 0) = \mu_0$ and $u(z, 0) = 0$. With a spatial discretization, $z_i = (i-1)\Delta z$ for $i = 1$ to $n+1$ and $\Delta z = 1/n$, we denote the nodal displacement and the chemical potential as: $u_i(t) = u(z_i, t)$ and $\mu_i(t) = \mu(z_i, t)$. The out-of-plane strain is then obtained at the midpoint as

$$(\varepsilon_{22})_i = \frac{u_{i+1} - u_i}{\Delta z} \quad (\text{B.32})$$

By Eq. (4.18), the in-plane strain is obtained as

$$\varepsilon_{11} = \sum_{i=1}^n (\varepsilon_{22})_i \Delta z \quad (\text{B.33})$$

Next, Eq. (2.47) is discretized and written in a matrix form as

$$\left[\frac{2(1-\nu)}{1-2\nu} \mathbf{I} + \frac{4\nu\Delta z}{1-2\nu} \mathbf{U} \right] \{(\varepsilon_{22})_i\} = \mathbf{V} \{\mu_i - \mu_0\} \quad (\text{B.34})$$

where \mathbf{I} is the identity matrix (n by n), \mathbf{U} is the unit matrix (n by n), and \mathbf{V} is a n by $n+1$ matrix to obtain the chemical potential at the midpoints by linear interpolation as $\mu_{i+1/2} = (\mu_i + \mu_{i+1})/2$. Given the distribution of the chemical potential, the strain $\{(\varepsilon_{22})_i, i = 1 - n\}$ can be obtained from (B.34), and the in-plane strain ε_{11} can be obtained from (B33) at the same time step.

To integrate over time, Eq. (2.46) is discretized at each node (except for the two end nodes, where the chemical potential is fixed by the boundary condition) as

$$\dot{\mu}_i + 4\dot{\varepsilon}_{11} = \frac{\mu_{i+1} - 2\mu_i + \mu_{i-1}}{(\Delta z)^2} \quad (\text{B.35})$$

Moreover, taking time derivative of (B.33) and (B.34), we obtain that

$$\dot{\varepsilon}_{11} = \sum_{i=1}^n (\dot{\varepsilon}_{22})_i \Delta z \quad (\text{B.36})$$

$$\left[\frac{2(1-\nu)}{1-2\nu} \mathbf{I} + \frac{4\nu\Delta z}{1-2\nu} \mathbf{U} \right] \{(\dot{\varepsilon}_{22})_i\} = \mathbf{V}\{\dot{\mu}_i\} \quad (\text{B.37})$$

The three rate equations, (B.35)-(B.37), can be solved simultaneously to find $\dot{\mu}_i$ ($i = 2$ to n), $(\dot{\varepsilon}_{22})_i$ ($i = 1$ to n), and $\dot{\varepsilon}_{11}$.

Using the forward finite difference scheme in time we update the values at time $t + \Delta t$ as

$$\mu_i(t + \Delta t) = \mu_i(t) + \dot{\mu}_i \Delta t \quad (\text{B.38})$$

$$(\varepsilon_{22})_i(t + \Delta t) = (\varepsilon_{22})_i(t) + (\dot{\varepsilon}_{22})_i \Delta t \quad (\text{B.39})$$

$$\varepsilon_{11}(t + \Delta t) = \varepsilon_{11}(t) + \dot{\varepsilon}_{11} \Delta t \quad (\text{B.40})$$

The procedure repeats itself to evolve the fields of chemical potential and the strain. The method is conditionally stable and requires a relatively small time step Δt . For the simulation in Fig. 1.9, we have used $\Delta t = 0.0001$ and $\Delta z = 0.02$.

Alternatively, by using the backward time difference, the method is more stable and allows using much larger time steps for faster calculations. Briefly, the rate equations can be written in a matrix form

$$\mathbf{M}\dot{\mathbf{u}} = \mathbf{P}\mathbf{u} \quad (\text{B.41})$$

where \mathbf{u} represents a vector including all the variables, μ_i ($i = 2$ to n), $(\varepsilon_{22})_i$ ($i = 1$ to n), and ε_{11} . The two matrices \mathbf{M} and \mathbf{P} are independent of time. By backward difference, we obtain that

$$\mathbf{M}(\mathbf{u}(t + \Delta t) - \mathbf{u}(t)) = \Delta t \mathbf{P} \mathbf{u}(t + \Delta t) \quad (\text{B.42})$$

The vector can then be updated as

$$\mathbf{u}(t + \Delta t) = [\mathbf{M} - \Delta t \mathbf{P}]^{-1} \mathbf{M} \mathbf{u}(t) \quad (\text{B.43})$$

APPENDIX C: ANALYTICAL SOLUTIONS FOR CONSTRAINED SWELLING OF HYDROGELS

C.1 Initial state

The hydrogel in the initial state is assumed to be homogeneous, isotropically swollen from the dry state, with the principal stretch $\lambda_i = \lambda_0$ for $i = 1$ to 3. The initial state is stress-free, and thus by Eq. (3.2) we have

$$s_{11} = s_{22} = s_{33} = Nk_B T \left(\lambda_0 - \frac{1}{\lambda_0} \right) + K \lambda_0^2 (\lambda_0^3 - 1 - \Omega C_0) = 0 \quad (\text{C.1})$$

from which the nominal concentration at the initial state C_0 can be determined. The initial chemical potential is then obtained by Eq. (3.3) as

$$\mu_0 = k_B T \left(\ln \frac{\Omega C_0}{1 + \Omega C_0} + \frac{(1 + \Omega C_0) + \chi}{(1 + \Omega C_0)^2} \right) - \Omega K (\lambda_0^3 - 1 - \Omega C_0) \quad (\text{C.2})$$

For the incompressible limit with $K \rightarrow \infty$, the two equations (C.1) and (C.2) can be combined into one by eliminating K , namely

$$\frac{\mu_0}{k_B T} = \left(\ln \frac{\Omega C_0}{1 + \Omega C_0} + \frac{(1 + \Omega C_0) + \chi}{(1 + \Omega C_0)^2} \right) + \frac{N\Omega}{\lambda_0^2} \left(\lambda_0 - \frac{1}{\lambda_0} \right) \quad (\text{C.3})$$

which can be solved with the incompressibility constraint, $\lambda_0^3 = 1 + \Omega C_0$, leading to

$$\frac{\mu_0}{k_B T} = \ln \frac{\lambda_0^3 - 1}{\lambda_0^3} + \frac{1}{\lambda_0^3} + \frac{\chi}{\lambda_0^6} + N\Omega \left(\frac{1}{\lambda_0} - \frac{1}{\lambda_0^3} \right) \quad (\text{C.4})$$

Equation (C.4) was corresponds to (B.18).

C.2 Equilibrium state

In the equilibrium state, the chemical potential equals zero everywhere, and the principal stretches of the constrained hydrogel layer become $\lambda_2 = \lambda_\infty$ and $\lambda_1 = \lambda_3 = \lambda_0$, along with an equilibrium concentration C_∞ . By Eq. (3.3), we have

$$\mu = k_B T \left(\ln \frac{\Omega C_\infty}{1 + \Omega C_\infty} + \frac{(1 + \Omega C_\infty) + \chi}{(1 + \Omega C_\infty)^2} \right) - \Omega K (\lambda_\infty \lambda_0^2 - 1 - \Omega C_\infty) = 0 \quad (\text{C.5})$$

Moreover, since the surface of the hydrogel is traction free, the nominal stress in the thickness direction must be zero. By Eq. (3.2), we obtain that

$$s_{22} = N k_B T \left(\lambda_\infty - \frac{1}{\lambda_\infty} \right) + K \lambda_0^2 (\lambda_\infty \lambda_0^2 - 1 - \Omega C_\infty) = 0 \quad (\text{C.6})$$

Eqs. (C.5)-(C.6) can be solved simultaneously to obtain the equilibrium swelling ratio λ_∞ and the solvent concentration C_∞ , depending on the initial swelling ratio λ_0 and the material properties ($N\Omega$, χ and K).

For the limiting case with $K \rightarrow \infty$, Eqs. (C.5-C.6) can be combined into one by eliminating K and solved with the incompressibility constraint, $\lambda_\infty \lambda_0^2 = 1 + \Omega C_\infty$, leading to

$$\ln \frac{\lambda_\infty \lambda_0^2 - 1}{\lambda_\infty \lambda_0^2} + \frac{1}{\lambda_\infty \lambda_0^2} + \frac{\chi}{\lambda_\infty^2 \lambda_0^4} + \frac{N\Omega}{\lambda_0^2} \left(\lambda_\infty - \frac{1}{\lambda_\infty} \right) = 0 \quad (\text{C.7})$$

and corresponds to Eq.(B5).

C.3 Early stage of swelling: a self-similar solution

The transient process of constrained swelling can be described by a nonlinear diffusion equation. With the principal stretch $\lambda_2(X_2, t)$ and the solvent concentration $C(X_2, t)$, the chemical potential by Eq. (3.3) is

$$\mu = k_B T \left(\ln \frac{\Omega C}{1 + \Omega C} + \frac{(1 + \Omega C) + \chi}{(1 + \Omega C)^2} \right) - \Omega K (\lambda_2 \lambda_0^2 - 1 - \Omega C) \quad (\text{C.8})$$

The traction-free boundary condition on the surface requires that the nominal stress in the thickness direction be zero, namely

$$s_{22} = N k_B T \left(\lambda_2 - \frac{1}{\lambda_2} \right) + K \lambda_0^2 (\lambda_2 \lambda_0^2 - 1 - \Omega C) = 0 \quad (\text{C.9})$$

giving an expression for the nominal concentration as a function of the principal stretch

$$C = \frac{1}{\Omega} \left[\frac{N k_B T}{K \lambda_0^2} \left(\lambda_2 - \frac{1}{\lambda_2} \right) + \lambda_2 \lambda_0^2 - 1 \right] \quad (\text{C.10})$$

The flux in the thickness direction is obtained from Eqs. (2.12) as

$$J_2 = -M_{22} \frac{\partial \mu}{\partial X_2} = -\frac{DC}{k_B T \lambda_2^2} \frac{\partial \mu}{\partial X_2} \quad (\text{C.11})$$

Substituting (C.10) and (C.11) into Eq. (3.8) with $r = 0$ (assuming no source), we obtain that

$$\gamma(\lambda_2) \frac{\partial \lambda_2}{\partial t} = D \frac{\partial}{\partial X_2} \left[\xi(\lambda_2) \frac{\partial \lambda_2}{\partial X_2} \right] \quad (\text{C.12})$$

where

$$\gamma(\lambda_2) = \Omega \frac{\partial C}{\partial \lambda_2} = \lambda_0^2 + \frac{N k_B T}{K \lambda_0^2} \left(1 + \frac{1}{\lambda_2^2} \right) \quad (\text{C.13})$$

$$\begin{aligned} \xi(\lambda_2) &= \frac{\Omega C}{k_B T \lambda_2^2} \left(\frac{\partial \mu}{\partial C} \frac{\partial C}{\partial \lambda_2} + \frac{\partial \mu}{\partial \lambda_2} \right) = \\ &= \left(\frac{1}{(1 + \Omega C)^2} - \frac{2\chi\Omega C}{(1 + \Omega C)^3} \right) \left(\frac{N k_B T (1 + \lambda_2^2)}{K \lambda_0^2 \lambda_2^4} + \frac{\lambda_0^2}{\lambda_2^2} \right) + \frac{N \Omega^2 C (1 + \lambda_2^2)}{\lambda_0^2 \lambda_2^4} \end{aligned} \quad (\text{C.14})$$

At the early stage of swelling ($t \rightarrow 0$), the nonlinear diffusion equation (C.12) can be linearized as

$$\frac{\partial \lambda_2}{\partial t} = \frac{D\xi(\lambda_0)}{\gamma(\lambda_0)} \frac{\partial^2 \lambda_2}{\partial X_2^2} \quad (\text{C.15})$$

leading to a self-similar solution

$$\frac{\lambda_2 - \lambda_0}{\lambda_\infty - \lambda_0} = \text{erfc} \left(\frac{(H - X_2)}{2} \sqrt{\frac{\gamma(\lambda_0)}{D\xi(\lambda_0)t}} \right) \quad (\text{C.16})$$

The change of the thickness of the hydrogel layer is then obtained as

$$\Delta h(t) = \int_{-\infty}^H (\lambda_2 - \lambda_0) dX_2 = 2(\lambda_\infty - \lambda_0) \sqrt{\frac{\xi(\lambda_0)Dt}{\gamma(\lambda_0)\pi}} \quad (\text{C.17})$$

For the limiting case with $K \rightarrow \infty$ and using the incompressibility constraint, $\lambda_0^3 = 1 + \Omega C$, it can be shown that the self-similar solutions given by Eqs. (C.16) and (C.17) recover the equivalent self-similar solutions in Chapter 2, with $\gamma(\lambda_0) \rightarrow \lambda_0^2$ and $\xi(\lambda_0) \rightarrow \frac{1}{\lambda_0^6} - \frac{2\chi(\lambda_0^3 - 1)}{\lambda_0^9} + N\Omega \frac{(\lambda_0^3 - 1)(\lambda_0^2 + 1)}{\lambda_0^6}$. As noted in the previous study, a similar solution was obtained in linear poroelasticity (Yoon et al., 2010; Doi et al., 2009).

APPENDIX D: FLAT PUNCH INDENTATION OF AN ELASTIC HALF SPACE

Several textbooks have presented analytical solutions for plane-strain indentation of an elastic half space using a rigid flat punch (e.g., Johnson, 1985; Bower, 2010). Assuming no slip in the contact region of the surface, the normal and shear tractions on the contact surface ($|x| < a$) can be written as

$$\sigma + i\tau = -\frac{2(1-\nu)}{\sqrt{3-4\nu}} \frac{F}{\pi\sqrt{a^2-x^2}} \left(\frac{a+x}{a-x}\right)^{i\eta} \quad (\text{D.1})$$

where ν is Poisson's ratio, $\eta = [1/(2\pi)] \ln(3-4\nu)$ and F is the total normal force (per unit length). Note that the stress field has an oscillatory singularity at the edge of the flat punch ($|x| \rightarrow a$) unless $\nu = 0.5$.

To determine the indentation displacement, however, a point of datum has to be used. An analytical solution for the general case is possible but too lengthy to be included here. As a special case for $\nu = 0.5$, we have $\tau = 0$ and the solution coincides with that of frictionless contact with

$$\sigma = -\frac{F}{\pi\sqrt{a^2-x^2}} \quad (\text{D.2})$$

Following the complex variable method in Bower (2010), the displacement at a point located on the line of symmetry ($x = 0$) under the indenter can be obtained as

$$u_y(0, y) = -\frac{(1-\nu)F}{\pi G} \ln\left(y + \sqrt{y^2 + a^2}\right) + d \quad (\text{D.3})$$

where y is the distance from the surface and G is shear modulus of the material. Taking the point at $y = h$ as a datum with zero displacement, we obtain that

$$d = \frac{(1-\nu)F}{\pi G} \ln\left(h + \sqrt{h^2 + a^2}\right) \quad (\text{D.4})$$

The surface displacement under the flat punch indenter is then

$$\delta = u_y(0,0) = \frac{(1-\nu)F}{\pi G} \ln \left(\frac{h}{a} + \sqrt{1 + \left(\frac{h}{a}\right)^2} \right) \quad (\text{D.5})$$

As noted in Fig. 5.2, Eq. (D.5) considerably overestimates the indentation displacement for an elastic layer of thickness h . Apparently, the elastic layer has a much larger contact stiffness due to the presence of a rigid substrate, even for a very shallow indentation under the plane strain condition.

Bibliography

1. ABAQUS, (2013). ABAQUS 6.13 User Documentation, by Dassault Systèmes Simulia Corp., Providence, RI.
2. Abidian, M. R., & Martin, D. C. (2009). Multifunctional nanobiomaterials for neural interfaces. *Advanced Functional Materials*, 19(4), 573-585.
3. Al-Khelaiwi, F. T., Birchenko, V. M., Konopczynski, M. R., & Davies, D. (2010). Advanced Wells: A Comprehensive Approach to the Selection Between Passive and Active Inflow-Control Completions. *SPE Production & Operations*, 25(03), 305-326.
4. Babuška, I. (1971). Error-bounds for finite element method. *Numerische Mathematik*, 16(4), 322-333.
5. Baek, S., & Srinivasa, A. R. (2004). Diffusion of a fluid through an elastic solid undergoing large deformation. *International Journal of non-linear Mechanics*, 39(2), 201-218.
6. Barrière, B., & Leibler, L. (2003). Kinetics of solvent absorption and permeation through a highly swellable elastomeric network. *Journal of Polymer Science Part B: Polymer Physics*, 41(2), 166-182.
7. Baumberger, T., Caroli, C., & Martina, D. (2006). Solvent control of crack dynamics in a reversible hydrogel. *Nature Materials*, 5(7), 552-555.
8. Beebe, D. J., Moore, J. S., Bauer, J. M., Yu, Q., Liu, R. H., Devadoss, C., & Jo, B. H. (2000). Functional hydrogel structures for autonomous flow control inside microfluidic channels. *Nature*, 404(6778), 588-590.
9. Birgersson, E., Li, H., & Wu, S. (2008). Transient analysis of temperature-sensitive neutral hydrogels. *Journal of the Mechanics and Physics of Solids*, 56(2), 444-466.
10. Biot, M. A. (1941). General theory of three dimensional consolidation. *Journal of Applied Physics*, 12(2), 155-164.
11. Biot, M. A. (1955). Theory of elasticity and consolidation for a porous anisotropic solid. *Journal of Applied Physics*, 26(2), 182-185.
12. Bonn, D., Kellay, H., Prochnow, M., Ben-Djemaa, K., & Meunier, J. (1998). Delayed fracture of an inhomogeneous soft solid. *Science*, 280(5361), 265-267.
13. Bouklas, N., & Huang, R. (2012). Swelling kinetics of polymer gels: comparison of linear and nonlinear theories. *Soft Matter*, 8(31), 8194-8203.

14. Borja, R. I. (1986). Finite element formulation for transient pore pressure dissipation: A variational approach. *International Journal of Solids and Structures*, 22(11), 1201-1211.
15. Bower, A. F. (2010). *Applied Mechanics of Solids*. CRC Press, Boca Raton, FL.
16. Brezzi, F. (1974). On the existence, uniqueness and approximation of saddle-point problems arising from Lagrangian multipliers. *ESAIM: Mathematical Modelling and Numerical Analysis-Modélisation Mathématique et Analyse Numérique*, 8(R2), 129-151.
17. Broberg, K. B. (1999). *Cracks and fracture*. Academic Press
18. Caldorera-Moore, M., Kang, M. K., Moore, Z., Singh, V., Sreenivasan, S. V., Shi, L., & Roy, K. (2011). Swelling behavior of nanoscale, shape- and size-specific, hydrogel particles fabricated using imprint lithography. *Soft Matter*, 7(6), 2879-2887., 7, 2879.
19. Carroll, M. M. (1979). An effective stress law for anisotropic elastic deformation. *Journal of Geophysical Research: Solid Earth (1978–2012)*, 84(B13), 7510-7512.
20. Chan, E. P., Hu, Y., Johnson, P. M., Suo, Z., & Stafford, C. M. (2012). Spherical indentation testing of poroelastic relaxations in thin hydrogel layers. *Soft Matter*, 8(5), 1492-1498.
21. Chaudhury, M. K., & Whitesides, G. M. (1991). Direct measurement of interfacial interactions between semispherical lenses and flat sheets of poly (dimethylsiloxane) and their chemical derivatives. *Langmuir*, 7(5), 1013-1025.
22. Chen, Q., Zhu, L., Huang, L., Chen, H., Xu, K., Tan, Y., & Zheng, J. (2014). Fracture of the Physically Cross-Linked First Network in Hybrid Double Network Hydrogels. *Macromolecules*, 47(6), 2140-2148.
23. Cheng, A. D., Abousleiman, Y., & Roegiers, J. C. (1993). Review of some poroelastic effects in rock mechanics. *International journal of rock mechanics and mining sciences & geomechanics abstracts* , 30(7), 1119-1126
24. Cheng, A. D. (1997). Material coefficients of anisotropic poroelasticity. *International Journal of Rock Mechanics and Mining Sciences*, 34(2), 199-205.
25. Chester, S. A., & Anand, L. (2010). A coupled theory of fluid permeation and large deformations for elastomeric materials. *Journal of the Mechanics and Physics of Solids*, 58(11), 1879-1906.

26. Chien, N., & Herrmann, G. (1996). Conservation laws for thermo or poroelasticity. *Journal of applied mechanics*, 63(2), 331-336.
27. Coleman, B. D., & Noll, W. (1963). The thermodynamics of elastic materials with heat conduction and viscosity. *Archive for Rational Mechanics and Analysis*, 13(1), 167-178.
28. Cowin, S. C. (1999). Bone poroelasticity. *Journal of Biomechanics*, 32(3), 217-238.
29. Doi, M. (2009). Gel dynamics. *Journal of the Physical Society of Japan*, 78(5), 052001.
30. Dolbow, J., Fried, E., & Ji, H. (2004). Chemically induced swelling of hydrogels. *Journal of the Mechanics and Physics of Solids*, 52(1), 51-84.
31. Drury, J. L., & Mooney, D. J. (2003). Hydrogels for tissue engineering: scaffold design variables and applications. *Biomaterials*, 24(24), 4337-4351.
32. Duda, F. P., Souza, A. C., & Fried, E. (2010). A theory for species migration in a finitely strained solid with application to polymer network swelling. *Journal of the Mechanics and Physics of Solids*, 58(4), 515-529.
33. DuPont Jr, S. J., Cates, R. S., Stroot, P. G., & Toomey, R. (2010). Swelling-induced instabilities in microscale, surface-confined poly (N-isopropylacrylamide) hydrogels. *Soft Matter*, 6(16), 3876-3882.
34. Durning, C. J., & Morman Jr, K. N. (1993). Nonlinear swelling of polymer gels. *The Journal of Chemical Physics*, 98(5), 4275-4293., 98, 4275.
35. Flory, P. J., & Rehner Jr, J. (1943). Statistical mechanics of crosslinked polymer networks II. Swelling. *The Journal of Chemical Physics*, 11(11), 521-526.
36. P.J. Flory, *Principles of Polymer Chemistry*. Cornell University Press, Ithaca, NY, 1953.
37. Galaev, I. Y., & Mattiasson, B. (1999). 'Smart' polymers and what they could do in biotechnology and medicine. *Trends in biotechnology*, 17(8), 335-340.
38. Galli, M., & Oyen, M. L. (2009). Fast identification of poroelastic parameters from indentation tests. *Computer Modeling in Engineering and Sciences (CMES)*, 48(3), 241-268.

39. Gong, J. P., Katsuyama, Y., Kurokawa, T., & Osada, Y. (2003). Double-Network Hydrogels with Extremely High Mechanical Strength. *Advanced Materials*, 15(14), 1155-1158.
40. Gurtin, M. E. (1979). Path independent integral for thermoelasticity. *International Journal of Fracture*, 15(5), R169-R170.
41. Guvendiren, M., Burdick, J. A., & Yang, S. (2010). Kinetic study of swelling-induced surface pattern formation and ordering in hydrogel films with depth-wise crosslinking gradient. *Soft Matter*, 6(9), 2044-2049.
42. Haber, R. B. (1985). A consistent finite element technique for recovery of distributed reactions and surface tractions. *International Journal for Numerical Methods in Engineering*, 21(11), 2013-2025.
43. Harmon, M. E., Tang, M., & Frank, C. W. (2003). A microfluidic actuator based on thermoresponsive hydrogels. *Polymer*, 44(16), 4547-4556.
44. Hirotsu, S. (1991). Softening of bulk modulus and negative Poisson's ratio near the volume phase transition of polymer gels. *The Journal of Chemical Physics*, 94(5), 3949-3957.
45. Holtz, J. H., & Asher, S. A. (1997). Polymerized colloidal crystal hydrogel films as intelligent chemical sensing materials. *Nature*, 389(6653), 829-832.
46. Hong, W., Zhao, X., Zhou, J., & Suo, Z. (2008). A theory of coupled diffusion and large deformation in polymeric gels. *Journal of the Mechanics and Physics of Solids*, 56(5), 1779-1793.
47. Hong, W., Liu, Z., & Suo, Z. (2009a). Inhomogeneous swelling of a gel in equilibrium with a solvent and mechanical load. *International Journal of Solids and Structures*, 46(17), 3282-3289.
48. Hong, W., Zhao, X., & Suo, Z. (2009b). Formation of creases on the surfaces of elastomers and gels. *Applied Physics Letters*, 95(11), 111901.
49. Hu, Y., Zhao, X., Vlassak, J. J., & Suo, Z. (2010). Using indentation to characterize the poroelasticity of gels. *Applied Physics Letters*, 96(12), 121904.
50. Hu, Y., Chan, E. P., Vlassak, J. J., & Suo, Z. (2011). Poroelastic relaxation indentation of thin layers of gels. *Journal of Applied Physics* 110, 086103.
51. Hu, Y., You, J. O., Auguste, D. T., Suo, Z., & Vlassak, J. J. (2012). Indentation: a simple, nondestructive method for characterizing the

- mechanical and transport properties of pH-sensitive hydrogels. *Journal of Materials Research* 27, 152-160.
52. Huang, R. (2005) Kinetic wrinkling of an elastic film on a viscoelastic substrate. *Journal of the Mechanics and Physics of Solids*, 53, 63-89.
 53. Huang, R. & Im, S. H. (2006). Dynamics of wrinkle growth and coarsening in stressed thin films. *Physical Review E*, 74(2), 026214.
 54. Hughes, T. J. R. (1987). *The Finite Element Method: Linear Static and Dynamic Finite Element Analysis*. Prentice Hall, Englewood Cliffs, NJ.
 55. Hughes, T. J. R., Franca, L. P., & Balestra, M. (1986). A new finite element formulation for computational fluid dynamics: V. Circumventing the Babuška-Brezzi condition: A stable Petrov-Galerkin formulation of the Stokes problem accommodating equal-order interpolations. *Computer Methods in Applied Mechanics and Engineering*, 59(1), 85-99.
 56. Hui, C. Y., Jagota, A., Bennison, S. J., & Londono, J. D. (2003). Crack blunting and the strength of soft elastic solids. *Proceedings of the Royal Society of London.*, 459(2034), 1489-1516.
 57. Hui, C. Y., & Muralidharan, V. (2005). Gel mechanics: A comparison of the theories of Biot and Tanaka, Hocker, and Benedek. *The Journal of Chemical Physics*, 123(15), 154905.
 58. Hui, C. Y., Lin, Y. Y., Chuang, F. C., Shull, K. R., & Lin, W. C. (2006). A contact mechanics method for characterizing the elastic properties and permeability of gels. *Journal of Polymer Science Part B: Polymer Physics*, 44(2), 359-370.
 59. Hui, C. Y., Long, R., & Ning, J. (2013). Stress Relaxation Near the Tip of a Stationary Mode I Crack in a Poroelastic Solid. *Journal of Applied Mechanics*, 80(2), 021014.
 60. Jagur-Grodzinski, J. (2006). Polymers for tissue engineering, medical devices, and regenerative medicine. Concise general review of recent studies. *Polymers for Advanced Technologies*, 17(6), 395-418.
 61. Jeong, B., Bae, Y. H., Lee, D. S., & Kim, S. W. (1997). Biodegradable block copolymers as injectable drug-delivery systems. *Nature*, 388(6645), 860-862.
 62. Ji, H., Mourad, H., Fried, E., & Dolbow, J. (2006). Kinetics of thermally induced swelling of hydrogels. *International Journal of Solids and Structures*, 43(7), 1878-1907.
 63. Johnson, D. L. (1982). Elastodynamics of gels. *The Journal of Chemical Physics*, 77(3), 1531-1539.

64. Johnson, K. L., Kendall, K., & Roberts, A. D. (1971). Surface energy and the contact of elastic solids. *Proceedings of the royal society of London. A. mathematical and physical sciences*, 324(1558), 301-313.
65. Johnson, K. L. (1985). *Contact Mechanics*. Cambridge University Press, Cambridge, UK.
66. Kalcioğlu, Z. I., Mahmoodian, R., Hu, Y., Suo, Z., & Van Vliet, K. J. (2012). From macro-to microscale poroelastic characterization of polymeric hydrogels via indentation. *Soft Matter*, 8(12), 3393-3398.
67. Kang, M. K. & Huang, R. (2010a). A variational approach and finite element implementation for swelling of polymeric hydrogels under geometric constraints. *Journal of Applied Mechanics*, 77(6), 061004.
68. Kang, M. K. & Huang, R. (2010b). Swell-induced surface instability of confined hydrogel layers on substrates. *Journal of the Mechanics and Physics of Solids*, 58(10), 1582-1598.
69. Kang, M. K., & Huang, R. (2011). Swelling-induced instability of substrate-attached hydrogel lines. *International Journal of Applied Mechanics*, 3(02), 219-233.
70. Kishimoto, K., Aoki, S., & Sakata, M. (1980). On the path independent integral-J. *Engineering Fracture Mechanics*, 13(4), 841-850.
71. Kohles, S. S., & Roberts, J. B. (2002). Linear poroelastic cancellous bone anisotropy: trabecular solid elastic and fluid transport properties. *Journal of Biomechanical Engineering*, 124(5), 521-526..
72. Krishnan, V. R., Hui, C. Y., & Long, R. (2008). Finite strain crack tip fields in soft incompressible elastic solids. *Langmuir*, 24(24), 14245-14253.
73. Kwon, H. J., Rogalsky, A. D., & Kim, D. W. (2011). On the measurement of fracture toughness of soft biogel. *Polymer Engineering & Science*, 51(6), 1078-1086.
74. Lee, W., Lee, V., Polio, S., Keegan, P., Lee, J. H., Fischer, K., & Yoo, S. S. (2010). On demand three dimensional freeform fabrication of multi layered hydrogel scaffold with fluidic channels. *Biotechnology and bioengineering*, 105(6), 1178-1186.
75. Levental, I., Georges, P. C., & Janmey, P. A. (2007). Soft biological materials and their impact on cell function. *Soft Matter*, 3(3), 299-306.
76. Li, C., Hu, Z., & Li, Y. (1993). Poisson's ratio in polymer gels near the phase-transition point. *Physical Review E*, 48(1), 603.

77. Li, F. Z., Shih, C. F., & Needleman, A. (1985). A comparison of methods for calculating energy release rates. *Engineering Fracture Mechanics*, 21(2), 405-421.
78. Li, Y., & Tanaka, T. (1990). Kinetics of swelling and shrinking of gels. *The Journal of chemical physics*, 92(2), 1365-1371.
79. Liang, S., Hu, J., Wu, Z. L., Kurokawa, T., & Gong, J. P. (2012). Toughness Enhancement and Stick–Slip Tearing of Double-Network Hydrogels in Poly (ethylene glycol) Solution. *Macromolecules*, 45(11), 4758-4763.
80. Lucantonio, A., Nardinocchi, P., & Teresi, L. (2012). Transient analysis of swelling-induced large deformations in polymer gels. *Journal of the Mechanics and Physics of Solids*, 61(1), 205-218.
81. Luo, Y., & Shoichet, M. S. (2004). A photolabile hydrogel for guided three-dimensional cell growth and migration. *Nature Materials*, 3(4), 249-253.
82. McMeeking, R. M. (1977). Finite deformation analysis of crack-tip opening in elastic-plastic materials and implications for fracture. *Journal of the Mechanics and Physics of Solids*, 25(5), 357-381.
83. Morales, D., Palleau, E., Dickey, M. D., & Velev, O. D. (2014). Electro-actuated hydrogel walkers with dual responsive legs. *Soft Matter*, 10(9), 1337-1348.
84. Murad, M. A., & Loula, A. F. (1992). Improved accuracy in finite element analysis of Biot's consolidation problem. *Computer Methods in Applied Mechanics and Engineering*, 95(3), 359-382.
85. Murad, M. A., & Loula, A. F. (1994). On stability and convergence of finite element approximations of Biot's consolidation problem. *International Journal for Numerical Methods in Engineering*, 37(4), 645-667.
86. Nohara, S., Wada, H., Furukawa, N., Inoue, H., Morita, M., & Iwakura, C. (2003). Electrochemical characterization of new electric double layer capacitor with polymer hydrogel electrolyte. *Electrochimica acta*, 48(6), 749-753.
87. Nowak, A. P., Breedveld, V., Pakstis, L., Ozbas, B., Pine, D. J., Pochan, D., & Deming, T. J. (2002). Rapidly recovering hydrogel scaffolds from self-assembling diblock copolypeptide amphiphiles. *Nature*, 417(6887), 424-428

88. Pal, K., Banthia, A. K., & Majumdar, D. K. (2009). Polymeric hydrogels: characterization and biomedical applications. *Designed monomers and polymers*, 12(3), 197-220.
89. Palleau, E., Morales, D., Dickey, M. D., & Velev, O. D. (2013). Reversible patterning and actuation of hydrogels by electrically assisted ionoprinting. *Nature Communications*, 4.
90. Peppas, N. A., Hilt, J. Z., Khademhosseini, A., & Langer, R. (2006). Hydrogels in biology and medicine: from molecular principles to bionanotechnology. *Advanced Materials*, 18(11), 1345-1360.+
91. Peters, A., & Candau, S. J. (1988). Kinetics of swelling of spherical and cylindrical gels. *Macromolecules*, 21(7), 2278-2282.
92. Phillips, P. J. (2005). Finite element methods in linear poroelasticity: theoretical and computational results. PhD dissertation, University of Texas at Austin.
93. Phillips, P. J. & Wheeler, M. F. (2009). Overcoming the problem of locking in linear elasticity and poroelasticity: an heuristic approach. *Computational Geosciences*, 13(1), 5-12.
94. Prigogine, I. (1961). Introduction to thermodynamics of irreversible processes (pp. 1-257). New York: Interscience Publishers.
95. Qiu, Y., & Park, K. (2001). Environment-sensitive hydrogels for drug delivery. *Advanced drug delivery reviews*, 53(3), 321-339.
96. Rajagopal, K. R. (2003). Diffusion through polymeric solids undergoing large deformations. *Materials Science and Technology*, 19(9), 1175-1180.
97. Rice, J. R. (1968a). A path independent integral and the approximate analysis of strain concentration by notches and cracks. *Journal of Applied Mechanics*, 35(2), 379-386.
98. Rice, J. R. (1968b). Mathematical analysis in the mechanics of fracture. *Fracture: an advanced treatise*, 2, 191-311.
99. Rice, J. R., & Cleary, M. P. (1976). Some basic stress diffusion solutions for fluid saturated elastic porous media with compressible constituents. *Reviews of Geophysics*, 14(2), 227-241.
100. Ruina, A. (1978). Influence of coupled deformation-diffusion effects on the retardation of hydraulic fracture. In 19th US Symposium on Rock Mechanics (USRMS). American Rock Mechanics Association.
101. Scherer, G. W. (1989). Measuring of permeability I. Theory. *Journal of Non-Crystalline Solids*, 113, 107-118.

102. Scherer, G. W. (1992). Crack-tip stress in gels. *Journal of Non-Crystalline Solids*, 144, 210-216.
103. Sun, J. Y., Zhao, X., Illeperuma, W. R., Chaudhuri, O., Oh, K. H., Mooney, D. J., & Suo, Z. (2012). Highly stretchable and tough hydrogels. *Nature*, 489(7414), 133-136.
104. Sun, X. G., Liu, G., Xie, J., Han, Y., & Kerr, J. B. (2004). New gel polyelectrolytes for rechargeable lithium batteries. *Solid State Ionics*, 175(1), 713-716.
105. Suci, A. N., Iwatsubo, T., Matsuda, M., & Nishino, T. (2004). A study upon durability of the artificial knee joint with PVA hydrogel cartilage, *JSME International Journal Series C*, 47(1), 199-208.
106. Sussman, T. & Bathe, K. J. (1987). A finite element formulation for the nonlinear incompressible elastic and inelastic analysis. *Computers & Structures*, 26(1), 357-409.
107. Tanaka, T., Hocker, L., Benedek, G. (1973). Spectrum of light scattered from a viscoelastic gel. *Journal of Chemical Physics*, 59, 5151-5159.
108. Tanaka, T., & Fillmore, D. J. (1979). Kinetic models of gel extraction. *The Journal of Chemical Physics*, 70(3), 1214.
109. Tanaka, T., Sun, S. T., Hirokawa, Y., Katayama, S., Kucera, J., Hirose, Y., & Amiya, T. (1987). Mechanical instability of gels at the phase transition. *Nature* 325, 796-798.
110. Tanaka, Y., Abe, H., Kurokawa, T., Furukawa, H., & Gong, J. P. (2009). First Observation of Stick– Slip Instability in Tearing of Poly (vinyl alcohol) Gel Sheets. *Macromolecules*, 42(15), 5425-5426.
111. Taylor, C. & Hood, P. (1973). A numerical solution of the Navier-Stokes equations using the finite element technique. *Computers & Fluids* 1, 73-100.
112. Thompson, M., & Willis, J. R. (1991). A reformation of the equations of anisotropic poroelasticity. *Journal of Applied Mechanics*, 58(3), 612-616.
113. Tirumala, V. R., Divan, R., Ocola, L. E., & Mancini, D. C. (2005). Direct-write e-beam patterning of stimuli-responsive hydrogel nanostructures. *Journal of Vacuum Science & Technology B*, 23(6), 3124-3128.
114. Toh, W., Liu, Z., Ng, T. Y., & Hong, W. (2013). Inhomogeneous Large Deformation Kinetics of Polymeric Gels. *International Journal of Applied Mechanics* 5, 1350001.

115. Tokarev, I., & Minko, S. (2009). Stimuli-responsive hydrogel thin films. *Soft Matter*, 5(3), 511-524.
116. Trujillo, V., Kim, J., Hayward, R.C. (2008). Creasing instability of surface-attached hydrogels. *Soft Matter* 4, 564–569.
117. Ulijn, R. V., Bibi, N., Jayawarna, V., Thornton, P. D., Todd, S. J., Mart, R. J., & Gough, J. E. (2007). Bioresponsive hydrogels. *Materials Today*, 10(4), 40-48.+
118. Vermeer, P. A., & Verruijt, A. (1981). An accuracy condition for consolidation by finite elements. *International Journal for Numerical and Analytical Methods in Geomechanics* 5, 1-14.
119. Vlassak, J. J., & Nix, W. D. (1994). Measuring the elastic properties of anisotropic materials by means of indentation experiments. *Journal of the Mechanics and Physics of Solids*, 42(8), 1223-1245.
120. Wan, J. (2002). Stabilized finite element methods for coupled geomechanics and multiphase flow. PhD dissertation, Stanford University.
121. Wang, X. & Hong, W. (2012a). A visco-poroelastic theory for polymeric gels. *Proceedings of the Royal Society A: Mathematical, Physical and Engineering Science* 468, 3824-3841.
122. Wang, X., & Hong, W. (2012b). Delayed fracture in gels. *Soft Matter*, 8(31), 8171-8178.
123. Weiss, F., Cai, S., Hu, Y., Kang, M. K., Huang, R., & Suo, Z. (2013). Creases and wrinkles on the surface of a swollen gel. *Journal of Applied Physics*, 114(7), 073507.
124. White, J. A. & Borja, R. I. (2008). Stabilized low-order finite elements for coupled solid-deformation/fluid-diffusion and their application to fault zone transients. *Computer Methods in Applied Mechanics and Engineering*, 197(49), 4353-4366.
125. Willis, J. R. (1966). Hertzian contact of anisotropic bodies. *Journal of the Mechanics and Physics of Solids*, 14(3), 163-176.
126. Wilson, W. K., & Yu, I. W. (1979). The use of the J-integral in thermal stress crack problems. *International Journal of Fracture*, 15(4), 377-387.
127. Wu, Z., Bouklas, N., & Huang, R. (2013). Swell-induced surface instability of hydrogel layers with material properties varying in thickness direction. *International Journal of Solids and Structures* 50, 578-587.

128. Yoon, J., Cai, S., Suo, Z., & Hayward, R. C. (2010). Poroelastic swelling kinetics of thin hydrogel layers: comparison of theory and experiment. *Soft Matter*, 6(23), 6004-6012.
129. Zhang, J., Zhao, X., Suo, Z., & Jiang, H. (2009). A finite element method for transient analysis of concurrent large deformation and mass transport in gels. *Journal of Applied Physics*, 105(9), 093522.
130. Zhang, J., An, Y., Yazzie, K., Chawla, N., & Jiang, H. (2012). Finite element simulation of swelling-induced crack healing in gels. *Soft Matter*, 8(31), 8107-8112.
131. Zhao, X. (2014). Multi-scale multi-mechanism design of tough hydrogels: building dissipation into stretchy networks. *Soft Matter*, 10(5), 672-687.
132. Zienkiewicz, O. C., Chan, A. H. C., Pastor, M., Paul, D. K., & Shiomi, T. (1990). Static and dynamic behavior of soils: a rational approach to quantitative solutions. I. Fully saturated problems. *Proceedings of the Royal Society of London A. Mathematical and Physical Sciences* 429, 285-309.

Vita

Nikolaos Bouklas was born in Panorama, Thessaloniki. He studied at the American College of Thessaloniki, Greece through his high school years and graduated in June 2002. In September 2002, he enrolled in the Mechanical Engineering department of the Aristotle University in Thessaloniki, Greece. He received his Diploma in Engineering in the same department with a concentration in Machine Components and Design in June 2008. He started his Ph.D. study in the Aerospace Engineering & Engineering Mechanics department at The University of Texas at Austin in September 2009, working in Professor Rui Huang's and Professor Chad Landis' groups. During his graduate studies, he worked both as a teaching assistant and a research assistant in the department of Aerospace Engineering & Engineering Mechanics.

`nbouklas@utexas.edu`

This dissertation was typed by the author.